# On the Solid-State Dewetting of Au-Ni and Au-W Bilayer Polycrystalline Thin Films and the Formation of Alloy Micro- and Nanoparticles

DISSERTATION

zur Erlangung des akademischen Grades

**Doktoringenieur** (Dr.-Ing.)

der Fakultät für Elektrotechnik

und

Informationstechnik

an der Technischen Universität Ilmenau

vorgelegt von

Dipl.-Phys. Andreas Herz

geboren am 27. Juni 1986 in Mühlhausen/Thüringen.

urn:nbn:de:gbv:ilm1-2016000575

Gutachter: Univ.-Prof. Dr. rer. nat. habil. Dr. h. c. Peter Schaaf
Technische Universität Ilmenau

Univ.-Prof. Dr.-Ing. Jens Müller
Technische Universität Ilmenau

Prof. Eugen Rabkin
Technion – Israel Institute of Technology (IIT)

Tag der Einreichung: 1. Juli 2016

Tag der wissenschaftlichen Aussprache (öffentlicher Teil): 8. November 2016

„Die besten Dinge im Leben sind nicht die, die man für Geld bekommt.“ (Albert Einstein)

# Erklärung

Ich versichere, dass ich die vorliegende Arbeit ohne unzulässige Hilfe Dritter und ohne Benutzung anderer als der angegebenen Hilfsmittel angefertigt habe. Die aus anderen Quellen direkt oder indirekt übernommenen Daten und Konzepte sind unter Angabe der Quelle gekennzeichnet.

Bei der Auswahl und Auswertung folgenden Materials haben mir die nachstehend aufgeführten Personen in der jeweils beschriebenen Weise ~~entgeltlich~~/unentgeltlich[1] geholfen:

1. Martin Friák, IPM Brünn/CZ
2. Robert Müller, IPHT Jena
3. Marcel Himmerlich, TU Ilmenau

Weitere Personen waren an der inhaltlich-materiellen Erstellung der vorliegenden Arbeit nicht beteiligt. Insbesondere habe ich hierfür nicht die entgeltliche Hilfe von Vermittlungs- bzw. Beratungsdiensten (Promotionsberater oder anderer Personen) in Anspruch genommen. Niemand hat von mir unmittelbar oder mittelbar geldwerte Leistungen für Arbeiten erhalten, die im Zusammenhang mit dem Inhalt der vorgelegten Dissertation stehen.

Die Arbeit wurde bisher weder im In- noch im Ausland in gleicher oder ähnlicher Form einer Prüfungsbehörde vorgelegt.

Ich bin darauf hingewiesen worden, dass die Unrichtigkeit der vorstehenden Erklärung als Täuschungsversuch bewertet wird und gemäß § 7 Abs. 10 der Promotionsordnung den Abbruch des Promotionsverfahrens zur Folge hat.

Ilmenau, 1. Juli 2016
*(Ort, Datum)*

Andreas Hertz
*(Unterschrift)*

[1] Unzutreffendes bitte streichen.

# Danksagung

Zunächst möchte ich Herrn Univ.-Prof. Dr. rer. nat. habil. Dr. h. c. Peter Schaaf für die Möglichkeit und wissenschaftliche Betreuung meiner Promotion am *Institut für Werkstofftechnik* danken.

Die vorliegende Dissertation wurde im Rahmen des von der Deutschen Forschungsgemeinschaft im Einzelverfahren geförderten Projektes „*Funktionelle Nanopartikel-Anordnung durch Entnetzung von dünnen Schichten*“ (FuNParty, DFG Scha632/20-1) angefertigt. Herrn PD Dr.-Ing. habil. Dong Wang danke ich hierbei für seine stete Diskussions- und Hilfsbereitschaft. Dem Fachgebiet *Werkstoffe der Elektrotechnik* sei für die konstruktive Zusammenarbeit gedankt. Insbesondere den Damen Remdt und Roßberg sowie den Herren Grieseler, Hopfeld, Kups, Schawohl und Spieß danke ich für ihre Diskussions- und Hilfsbereitschaft zu materialanalytischen Aufgabe- und Fragestellungen. Bei den Mitarbeitern des *Instituts für Mikro- und Nanotechnologien IMN MacroNano®* der Technischen Universität Ilmenau bedanke ich mich für die Unterstützung bei prozesstechnischen Angelegenheiten, von der Wafer-Aufbereitung (die Damen Harnisch, Hartmann sowie Uziel) über die Beschichtung (die Herren Döll und Venier) und thermische Prozessführung (Frau Marquardt und Herr Stauden) bis zur Prozesskontrolle (die Herren Albrecht und Romanus). Frau M. Sc. Theresa Berthold und Herrn Dr. Marcel Himmerlich danke ich für ihre Zusammenarbeit bei XPS-Messungen und deren Auswertung. Weiterhin möchte ich mich bei allen Studenten, insbesondere bei Frau Franz sowie den Herren Hentschel und Theska, für ihre Mithilfe im Rahmen von Abschlussarbeiten oder Tätigkeiten als Hilfswissenschaftler bedanken. Herrn Dr. Robert Müller vom *Leibniz-Institut für Photonische Technologien IPHT* in Jena danke ich für seine Zusammenarbeit bei der magnetischen Charakterisierung von Gold-Nickel Partikeln. Besonderer Dank geht an Mgr. Martin Friák, Ph.D. vom *Institute of Physics of Materials* der *Czech Academy of Sciences* in Brünn/Tschechien. Die fruchtbare Zusammenarbeit zum Thema Phasenanordnung in Gold-Nickel Partikeln wird hoch geschätzt. Abschließend möchte ich mich bei meiner Freundin Diana, meinen Eltern Cornelia und Werner sowie meiner Schwester Claudia und Cousine Miriam bedanken, die mich während meiner Promotion liebevoll unterstützten und moralischen Beistand leisteten.

Ilmenau, im Juni 2016

# Table of contents

# Kurzfassung

In den vergangenen Jahren hat sich das Entnetzen dünner Schichten (*Dewetting*) wegen seiner Bedeutung in der Mikroelektronik zu einem breiten Forschungsfeld entwickelt. Ein Hauptgrund für das Versagen elektronischer Bauteile auf Dünnschichtbasis ist das Entnetzen beziehungsweise thermisch induzierte Agglomerieren der betreffenden Schichtmaterialien. Das Phänomen des Entnetzens kann umgekehrt gezielt angewendet werden um maßgeschneiderte Partikel im Submikrometerbereich zu erzeugen. Dieser Präparationsweg hat sich als einfacher und kosteneffizienter Ansatz im Bereich der Nanotechnologie etabliert. Kombiniert mit anderen Techniken wie der Lithographie können dann auf einfache Art und Weise präzise Nanopartikelanordnungen realisiert werden, welche vielversprechend für verschiedenste Anwendungen sind. Das Entnetzen im festen Zustand wird, weit unterhalb der Schmelztemperatur des betreffenden Schichtmaterials, durch die Bildung von Poren (also Lücken in der Schicht, sogenannte *Voids*) initiiert. Das anschließende *Void*-Wachstum hängt dann zum Beispiel davon ab, ob eine ein- oder polykristalline Mikrostruktur vorliegt. Begleitet von Kornwachstum und Texturänderungen stellt das Entnetzen eine vielschichtige Naturerscheinung dünner Schichten dar. Solche mikrostrukturellen Veränderungen spielen beim Entnetzen von Flüssigkeiten demgegenüber keine Rolle. Die Fülle an Einflussgrößen, welche das Entnetzen im festen Zustand bestimmen, macht es ungleich schwieriger eine in sich geschlossene „*Dewetting*-Theorie“ zu entwickeln. Das Verständnis der zugrunde liegenden Mechanismen war daher Gegenstand zahlreicher Arbeiten in jüngerer Vergangenheit. Nur wenig Aufmerksamkeit wurde dabei auf das Entnetzen dünner Schichten bestehend aus (metallischen) Doppel- beziehungsweise Multilagen oder auch Legierungen gerichtet. Die Motivation der vorliegenden Dissertation besteht darin, Effekte der Legierungsbildung auf das Entnetzen dünner Doppelschichten aufzuzeigen. Hierbei werden Au basierte Zweistoffsysteme herangezogen: **Au-Ni** und **Au-W**. Die Selbstanordnung solcher Schichten über das Entnetzen wird ferner benutzt um maßgeschneiderte, funktionelle Legierungspartikel zu generieren. Es wird gezeigt, dass Schichtreihenfolge, Einzelschichtdicke sowie Löslichkeit der beteiligten Komponenten die *Void*-Bildung und –Entwicklung maßgeblich beeinflussen. Feste Lösung und Übersättigung werden eine zentrale Rolle bei der Untersuchung der Phasenbildung in Au-Ni Partikeln spielen. Physikalische Gesetzmäßigkeiten auf der Nanoskala werden darüber hinaus zur Erklärung der beobachteten Erscheinungen herangezogen.

# Abstract

In recent years, thin film dewetting has become a broad field of research due to its importance in microelectronics. A primary reason for thin film devices to fail is the dewetting issue. However, this phenomenon can be employed to prepare tailored submicron particles as well. The dewetting route has been established in nanotechnology as a simple and cost-effective way. In combination with lithography techniques, precise arrangements of nanoparticles can be realized which are promising for a variety of applications. The dewetting in solid state occurs well below the melting point of the thin film material and is characterized by thermal initiation of crystal voids and their evolution in the remaining film. The latter depends, for example, on whether a single- or polycrystalline thin film microstructure is present. Accompanied by grain growth and thin film texture evolution, solid-state dewetting is a complex phenomenon (compared to liquid-state dewetting). The variety of parameters that have an impact on the dewetting makes it challenging to establish a self-contained "dewetting theory". Understanding the mechanisms behind solid-state dewetting was therefore subject to plenty of studies in the recent past. Only little work has been spent on the dewetting of bi-, multilayer or alloy thin films to reveal effects due to alloying. An increased thermal stability against dewetting might be achieved. The current thesis focuses on the solid-state dewetting of metallic bi-layer thin films consisting of *Au-based* binary alloys, in particular **Au-Ni** and **Au-W**. Self-assembly of metallic bi-layer thin films is further used to obtain tailored functional alloy particles. It will be shown that stacking sequence, individual layer thickness, and mutual solid solubility influences void formation and their evolution. Solid solution and supersaturation will play a key role to study phase formation in Au-Ni submicron particles. Physical principles at reduced scale will be applied to explain observations.

# 1 Introduction

The aim of this thesis is to attain new information about the dewetting of thin films in solid state. Main objective is the investigation of polycrystalline metallic bi-layer thin films as illustrated in Figure 1. Suitable metal pairs will be selected by thermodynamic criteria with respect to their solubility in solid state. Secondly, the dewetting phenomenon will be used as an approach to obtain functional alloy micro- and nanoparticles.

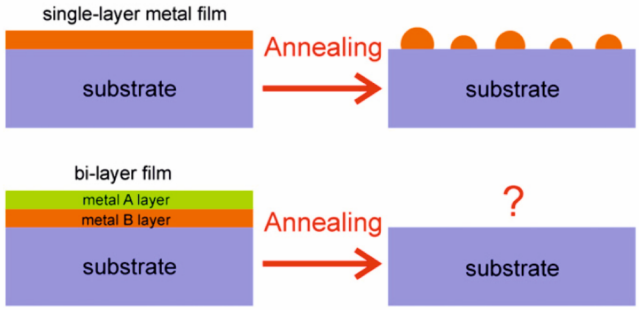


**Figure 1.** Scope of the current thesis. Concerning solid-state dewetting and subsequent particle formation, bi-layer thin films are expected to unveil even new effects due to alloying [1]. In particular, Au-Ni and Au-W films are studied.

Thin solid films deposited on inert substrates will undergo thermal agglomeration in order to minimize total energy. Due to their high surface-to-volume ratio, thin solid films are metastable and, upon thermal activation, the dewetting is driven mainly by surface (and interface) energy reduction – quite similar to a water droplet on a window. This phenomenon is an important factor in developing technological components based on thin films [2]. In recent years, understanding the mechanisms of solid-state dewetting has become a broad field of research. The dewetting is initiated by void nucleation or spinodal instabilities of the thin film. Grain boundary grooving in polycrystalline thin films may also initiate this process. Accompanied by redistribution of film material, the dewetting is determined by diffusion processes (surface, interface, and grain boundary) and ends up in the formation of isolated particles. A variety of influences exist to potentially control the dewetting and subsequent particle formation. Only little work has been spent on the effect of alloying in case of two or more component thin films. Contrary to single layer films, thermal diffusivities of the constituents as well as their solid solubility (self- and interdiffusion) may be crucial for morphology evolution. In this experimental work, Au-based binary alloys serve as model systems to show alloying effects on the solid-state dewetting. Moreover, thin films will be assessed in terms of their thermal stability. Thin film dewetting features a self-assembled

process which can be used as a simple and efficient way to form functional nanostructures potentially applicable in ecology such as catalysis, or information technology such as sensory/memory devices [3-5]. Also photonic nanocrystals are focused on [6]. In this context, *alloy* nanostructures may unveil even new properties due to the combination of size *and* composition [7].

Chapter 2 introduces mechanisms of void initiation in thin solid films. Morphology and microstructure evolution of both single crystal and polycrystalline thin films in the course of dewetting is compared, subsequent particle formation and associated features are discussed. As the starting point for the current thesis, recent studies on multicomponent thin film dewetting and alloy particle formation are briefly reviewed. Chapter 3 presents experimental methods and analytical tools applied in this work. Chapter 4 and 5 are dedicated to the dewetting of Au-W and Au-Ni bi-layer thin films. The role of individual layer thickness and stacking sequence at medium temperature is discussed. Features relating to oxidation are highlighted, alloying effects on the dewetting are pointed out. In chapter 6, Au-Ni bi-layer thin films are used to fabricate tailored alloy micro- and nanoparticles as illustrated in Figure 1. Underlying physical principles are applied and discussed. Moreover, substrate patterning using nanoimprint lithography is employed in order to create well-defined assemblies of alloy nanoparticles. The last chapter summarizes main findings of this work and presents/discusses perspectives associated with this thesis.

# 2 Fundamentals and review of state of the art

*This chapter introduces main aspects associated with the dewetting in solid state. For this purpose, essential recent studies are briefly reviewed. Fundamental mechanisms of void initiation are discussed. Morphology and microstructure evolution of single crystal as well as polycrystalline thin films in the course of dewetting are compared. It is shown that grain growth and void characteristics are necessarily connected with each other. Diffusion paths being active during dewetting involve the thin film surface, the film-substrate interface, and the grain boundaries. Their role in thin film dewetting as well as the influence of the annealing atmosphere are discussed. The concept of equilibrium crystal shape, metastable shape formation, and mean particle size are reviewed. As a last point, the dewetting of bi- or multicomponent thin films and alloy particle formation associated with thin film agglomeration are introduced, defining the starting point of the current thesis.*

## 2.1 Driving forces for thin film agglomeration

Thin solid films are characterized by a high surface-to-volume ratio, thus making them metastable or unstable against thermally induced film agglomeration. Surface/interface as well as strain may contribute to total energy.

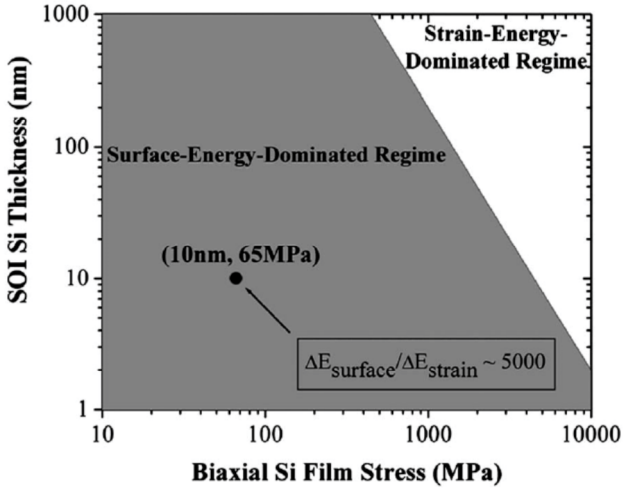


**Figure 2.** Si film thickness versus biaxial film stress. Two regimes dominated either by surface or strain energy can be identified for the silicon-on-insulator (SOI) dewetting system. Reprinted from Ref. [8].

However, depending on film thickness, thin film surface to strain energy ratio $\Delta E(surface)/\Delta E(strain)$ will change, making one contribution dominant in terms of total energy minimization as the driving force for the dewetting. Figure 2 exemplarily illustrates film

thickness as a function of biaxial film stress for a silicon-on-insulator dewetting system. It is shown that there are two energy regimes, one dominated by surface, the other one by strain energy. For a 10 nm thin Si film, $\Delta E(surface)/\Delta E(strain)$ is about 5000. This indicates that surface energy reduction will dominate the dewetting of ultrathin films.

## 2.2 Void formation in thin solid films

An important question is *how* thin *continuous* films transform into agglomerates via solid-state dewetting. The initial step for the dewetting to get started is spontaneous rupturing of the thin film. The following briefly reviews models which are established in literature. However, this summary raises no claim to completeness of all details.

A first approach, which may reasonably describe the morphology evolution of thin solid films, is the so-called ***spinodal dewetting***. Similarly to the liquid state, thin solid films are perturbed by wave fluctuations forming hills and depressions via surface diffusion. If the film is thin enough, these fluctuations the amplitude of which grows exponentially with thermal activation will cause the film to disintegrate into isolated features, *e.g.*, droplets or particles. A film having a total thickness $h$ becomes unstable against spontaneous dewetting when the GIBBS free energy per unit area complies with $\partial^2 G(h)/\partial h^2 < 0$. A characteristic wavelength $\lambda_C$ can then be connected to this condition via

$$\lambda > 2\pi\sqrt{-\gamma/G''(h)} := \lambda_C, \tag{1}$$

indicating the unstable, *i.e.*, growing modes for a given $h$ with $\gamma$ being the surface tension [9]. This situation is illustrated in Figure 3.


**Figure 3.** Illustrative model for spinodal dewetting. a) A continuous thin solid film in its as-deposited state. b) Thermally activated wave fluctuations form hills and depressions. c) Isolated film material exposes the former substrate. d) Eventually, single crystalline, faceted particles are formed. Reprinted from Ref. [10].

There is only little work spent on this dewetting mechanism in solid state. An obvious reason might be the fact that this approach does *not* take into account any *microstructural changes* of the solid film during dewetting, which is of paramount interest to potentially control this process. It solely considers spatial distribution of hole pattern at early stages to deduce the dominant dewetting mechanism. Figure 4 gives an idea of the procedure to analyze void pattern.

For this purpose, so-called MINKOWSKI functionals are used to be related to a suitable probability distribution. In order to analyze temporal changes in the spatial distribution of holes, deviations of these functionals from Poisson statistics are considered for different initial film thicknesses [11]: Generally speaking, if there is a remarkable deviation, a spatial correlation is existent, indicating that spinodal instabilities are dominant. Otherwise, a random distribution of holes represents stochastic processes such as void nucleation.

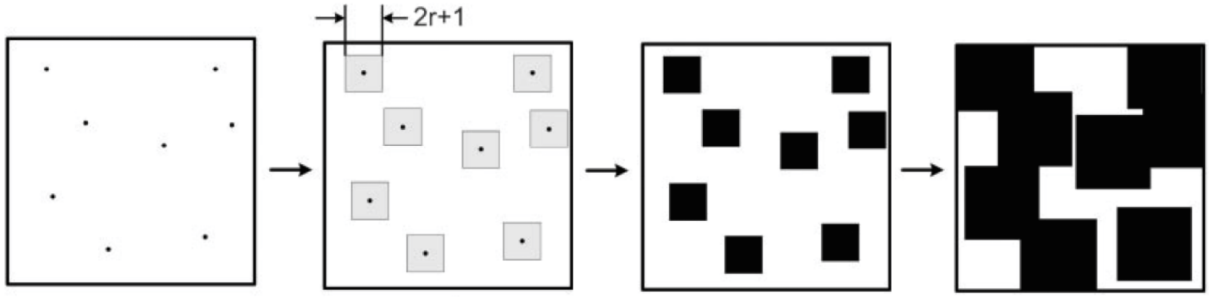


**Figure 4.** 2-d point pattern analysis for thin film dewetting. Positions of initiated voids are represented by point pattern in the binary image. Square grains which are centered on all points are then used to trace morphological changes by means of MINKOWSKI functionals. Reprinted from Ref. [11].

Homogeneous ***void nucleation*** may be another mechanism to break up a continuous thin film. In an analogous manner to a supercooled melt, voids have to reach a critical size in order to overcome the energy barrier to start growing.

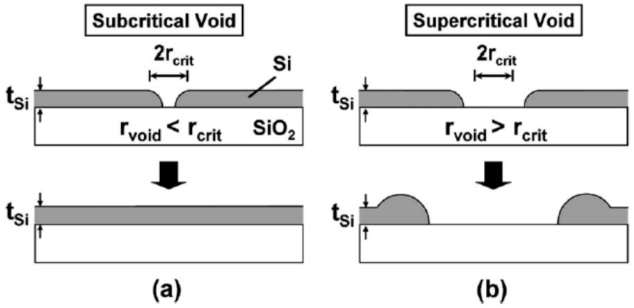


**Figure 5.** Homogeneous void nucleation. a) Subcritical and b) supercritical Si film voids are illustrated. Reprinted from Ref. [8].

Figure 5 shows that a subcritical void in a silicon film will not be able to further disclose the thin film, whereas a supercritical void ($> 2r_{\mathrm{crit}}$) can evolve. This energy barrier $\Delta G_{\mathrm{void}}$ was estimated for a silicon-on-insulator Si/$SiO_2$ film assuming that critical voids have a cylindrical shape. It was found that, even for a 1 nm Si film, an activation energy of about 60 eV is needed for homogeneous void nucleation. This considerably high value indicates that this mechanism will simply *not* contribute to film rupturing [8].

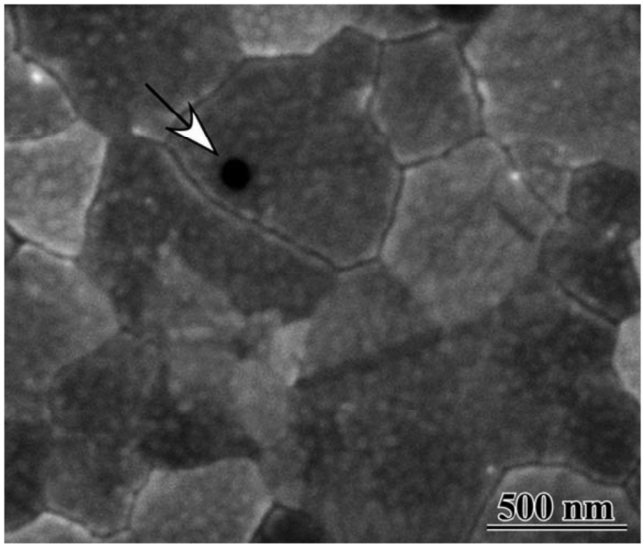


**Figure 6.** Critical Au film void after annealing at 700 °C for 10 min. The pinhole (appearing as a dark spot in SEM contrast, marked by an arrow) is located within a grain. Initial thickness of the Au thin film is 200 nm. Reprinted from Ref. [12].

Any defect being present in the film material may be the favorable site for the initiation of voids (heterogeneous nucleation), except for critical film voids such as pinholes (see Figure 6). Polycrystalline thin films provide plenty of defect area. Voids likely form at triple junctions subsequently evolving toward the free surface which is shown in Figure 7.

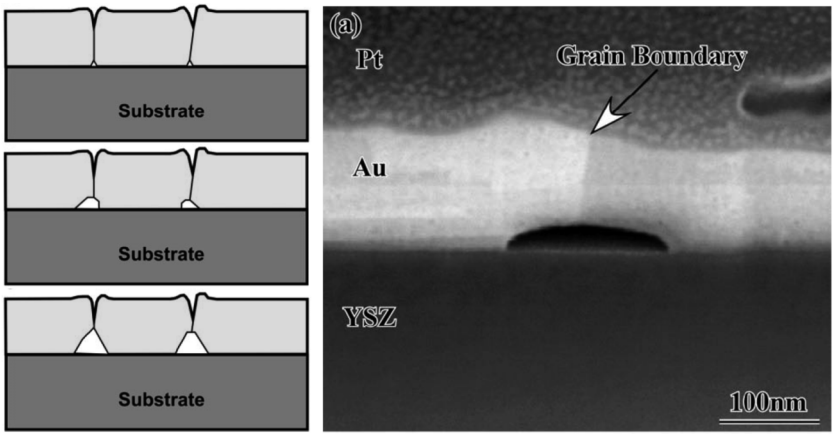


**Figure 7.** Heterogeneous void nucleation. Crystal voids likely form at triple junctions, as shown in a cross-sectional view for an Au film deposited on single crystal $Y_2O_3$-doped $ZrO_2$ (YSZ). Reprinted from Refs. [12, 13].

***Grooving*** can be considered as the top-down equivalent at which thermal grooves expose the substrate in the course of solid-state dewetting. There are two kinds of groove profiles proposed by *Mullins* in his pioneer work [14], a surface diffusion based contour as well as an evaporation-condensation based one. However, in practice, the latter will not play a major role during thin film retraction in solid-state. Surface diffusion (as one possible path to rearrange

film material) is related to the surface current $J$ of a number of atoms per unit area $\nu$ along the profile of a general surface which has a mean surface curvature $\kappa$,

$$\vec{J}_s = -\frac{D_s \gamma \Omega \nu}{k_B T} \nabla_s \kappa, \tag{2}$$

where $\Omega$ is the atomic volume. This model accounts for an *isotropic* case with the surface diffusion coefficient $D_s$, and the surface-free energy per unit area $\gamma$.[a] This means any change in the (local) surface curvature will initiate a motion of surface mobile atoms from positive to negative curvature in any direction alike. In practice, however, defects such as grain boundaries again will be the favorite site for this kinetic process, especially in polycrystalline thin films revealing columnar grains (Figure 8).

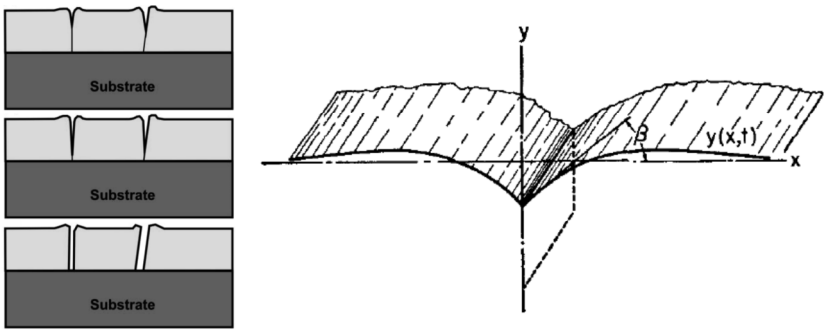


**Figure 8.** Thermal grooving. Such grooves likely evolve along grain boundaries in polycrystalline thin films. A profile *y(x,t)* due to surface diffusion is depicted to the right. Reprinted from Refs. [13, 14].

Regardless of which mechanism is the dominant one (*i.e.*, spinodal instabilities, void nucleation, or grooving) the ***incubation time*** for void initiation $t_i$ follows

$$t_i \propto \exp\left(\frac{E_i}{k_B T}\right) \tag{3}$$

by defining an activation energy $E_i$, which can be assumed to be a material parameter for a certain dewetting system. Hence, for fixed heat treatment cycles, this incubation time logarithmically decreases by increasing the temperature. However, the thicker the film the longer it takes to initiate film rupturing at a certain temperature [15], $h \propto \sqrt{t_i}$.

[a] Note that $s$ is curvilinear.

## 2.3 Evolution of single crystal thin films

Once a critical film void has formed by mechanisms introduced above, its ongoing evolution is a quite complex process. In case of ideal, *i.e.*, isotropic, single crystalline thin films, ***mass-shedding*** is supposed to be a sufficient model to describe a retracting film edge by capillary-driven surface diffusion. Based on Equation (2), evolutionary dynamics is then described through

$$\bar{u}_{\mathrm{n}} \propto \nabla_{\mathrm{s}}^{2}\kappa, \tag{4}$$

with $\bar{u}_{\mathrm{n}}$ being the surface mean normal velocity (Figure 9). Numerical modeling may then predict the evolution of the film edge, *e.g.*, as a function of the contact angle $\alpha$.

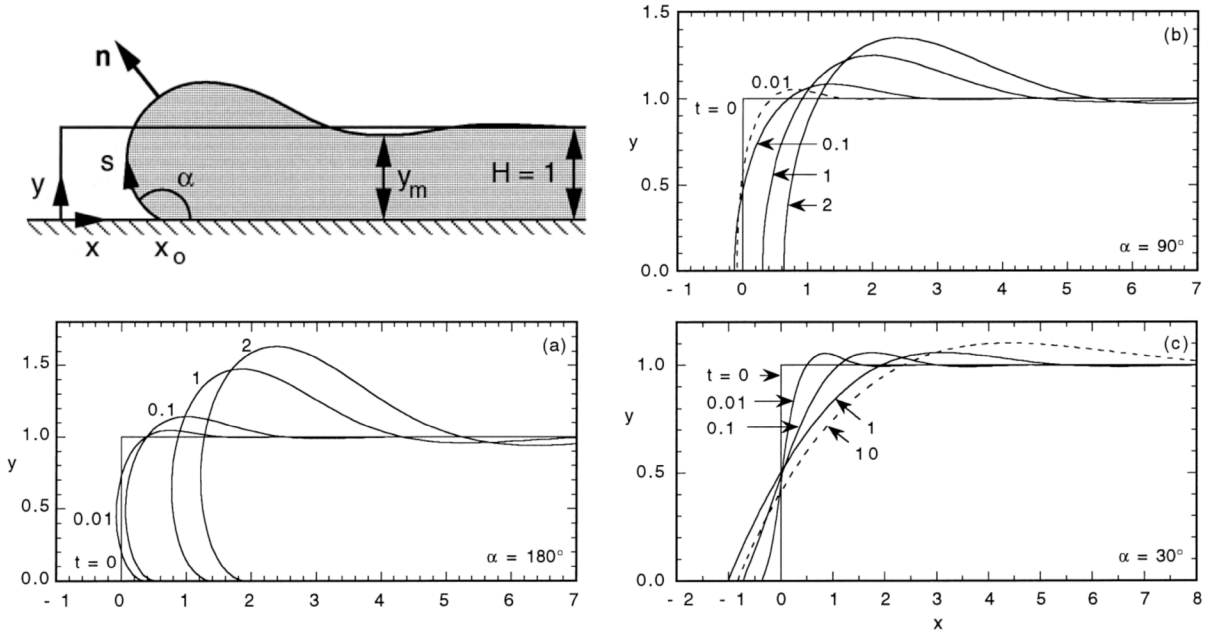


**Figure 9.** Mass-shedding. Numerical modeling of a retracting film step for the isotropic case. Evolutionary dynamics of the profile *y(x,t)* depends on the contact angle α of the film material. Reprinted from Ref. [16].

***Capillary instabilities*** are summarized by a family of similar morphological features, which result in complex pattern formation in continuous single crystalline thin films upon annealing. These can be specified as follows:

- *Rayleigh-like*

  High-aspect-ratio objects at the nanoscale are subject to generalized Rayleigh instabilities in such ways that these objects disintegrate into particle-like structures upon thermal activation. Linear stability analysis reveals that particle spacing scales with the line width *w* and thickness *t* as $(wt)^{1/2}$ [17]. A comprehensive experimental

examination of Rayleigh-Plateau instability of a Ni thin film strip can be found elsewhere [18]. In solid-state, size and spacing of the nanoparticles further depend on the crystallinity of the former wire [19].

- *Fingering*

  The rim (as a high-aspect-ratio object) of a retracting film may also undergo Rayleigh-like instabilities, forming fingers which in turn disintegrate into isolated droplets (see scheme in Figure 10).

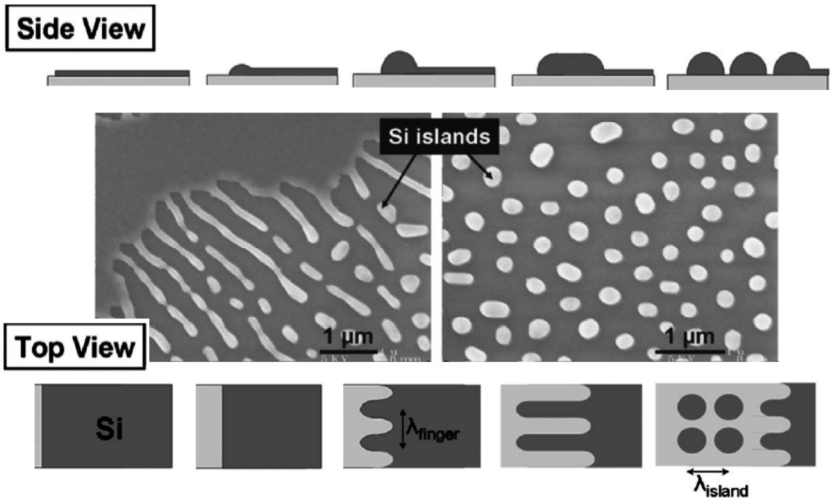


**Figure 10.** Fingering instabilities for a silicon-on-insulator (SOI, Si on $SiO_2$) dewetting system (Si film thickness < 30 nm), UHV annealed at 850 °C for 30 min. Schemes (side/top view) illustrate thin film evolution. Reprinted from Ref. [8].

- *Corner instabilities*

  Corner or edge instabilities result from an inhomogeneous diffusion field around the corner, similar to an electric field around a metal tip. A natural hole will therefore evolve along this diffusion field forming elongated void shapes (see scheme in Figure 11 as well as Figure 12a).

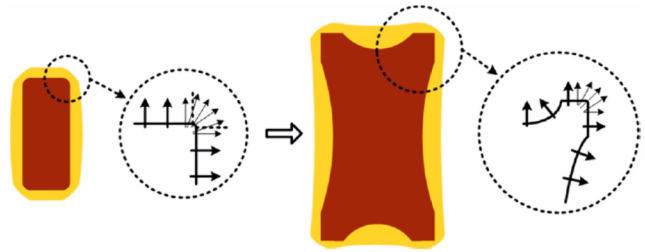

**Figure 11.** Corner or edge instabilities of a hole. An inhomogeneous diffusion field leads to different growth rates around the corner. Reprinted from Ref. [20].

- *Pinch-off*

  As a direct consequence of the mass-shedding mechanism, depressions which form right behind the elevated rim may result in a pinch-off. Axial shape symmetry can be observed which is shown in Figure 12 for a natural hole in a single crystalline Ni (110) thin film. Its temporal evolution upon annealing reveals surface-diffusion-induced morphological instabilities, which result in complex pattern formation once natural holes impinge each other.

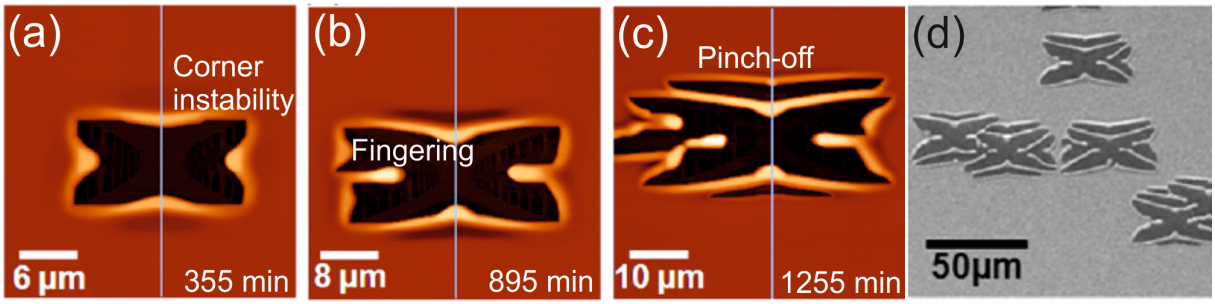


**Figure 12.** Complex pattern formation observed for a 120 nm thick single crystalline Ni (110) film due to surface-diffusion-induced morphological instabilities upon annealing at 900 °C. (a - c) Atomic-force microscopy (AFM) micrographs showing temporal evolution of a single hole. (d) SEM micrograph showing several hole pattern which are about to impinge each other. Reprinted from Ref. [20].

Moreover, ***anisotropic effects*** such as faceting likely appear in solid-state due to surface energy anisotropy. Figure 13 shows a retracting Ni film edge which reveals facets along its profile.

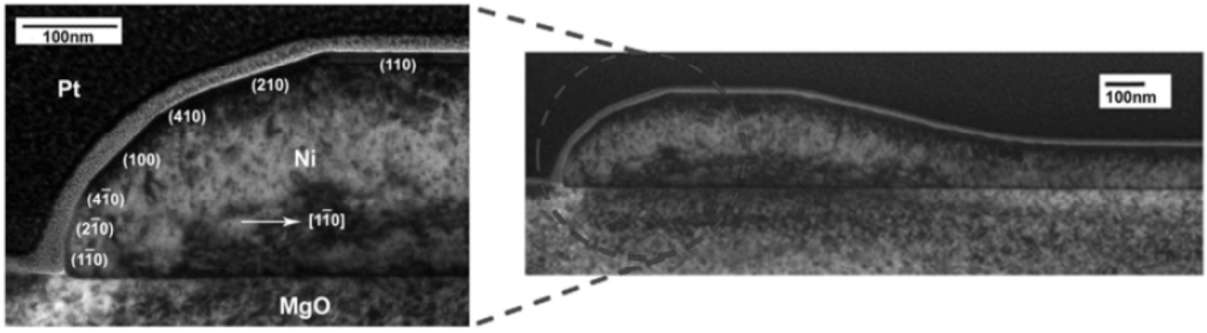


**Figure 13.** Edge faceting along a retracting Ni (110) film. TEM observation reveals that the rim consists of micro-faces belonging to different orientations. Reprinted from Ref. [21].

## 2.4 GIBBS free energy of a polycrystalline binary alloy and thin film dewetting

Subsequent derivation briefly introduces GIBBS free energy of a material containing an interface, following Ref. [22]. In condensed matter, GIBBS free energy expressed by its natural variables, *i.e.*, the temperature $T$, the pressure $p$, and the number of atoms $N$, is [23]

$$\mathrm{d}G = V\mathrm{d}p - S\mathrm{d}T + \sum_i \mu_i \mathrm{d}N_i, \tag{5}$$

with the volume $V = \partial G/\partial p$, the entropy $S = \partial G/\partial T$, as well as the chemical potential of the *i-th* atom

$$\mu_i = \frac{\partial G}{\partial N_i}\Big|_{T,p,N_j}. \tag{6}$$

For a binary alloy of *A* and *B* atoms at constant temperature and constant pressure GIBBS free energy is

$$\mathrm{d}G_\mathrm{m} = \mu_A \mathrm{d}N_A + \mu_B \mathrm{d}N_B. \tag{7}$$

When the material (m) contains an interface (i), as is the case with grain and/or phase boundaries in a polycrystalline microstructure, or simply a surface, the following equation holds

$$\mathrm{d}G_\mathrm{i} = \mu_A \mathrm{d}N_A + \mu_B \mathrm{d}N_B + \gamma \mathrm{d}a, \tag{8}$$

with the energy $\gamma$ and the total area *a* of the interface. For a closed system, any exchange of atoms between the host material and the interface is given by

$$\mathrm{d}N_{\mathrm{m},A} = -\mathrm{d}N_{\mathrm{i},A} \tag{9}$$

and

$$\mathrm{d}N_{\mathrm{m},B} = -\mathrm{d}N_{\mathrm{i},B}. \tag{10}$$

Then, the total change in GIBBS free energy is

$$\mathrm{d}G = (\mathrm{d}G_\mathrm{m} + \mathrm{d}G_\mathrm{i})_{N_A,N_B} = \gamma \mathrm{d}a. \tag{11}$$

This relation will be used to explain void evolution in polycrystalline, binary Au-Ni thin films, *cf.* chapter 5.2.

## 2.5 Void evolution in polycrystalline thin films

Due to the huge defect area being present in continuous polycrystalline thin films, void evolution will be different from its single crystalline counterpart. The following presents findings of recent studies dealing with this issue.

### *2.5.1 Grain growth and texture evolution*

During annealing, void formation and grain growth are shown to interact in such a way that *branched* void growth is usually observed for polycrystalline thin films.

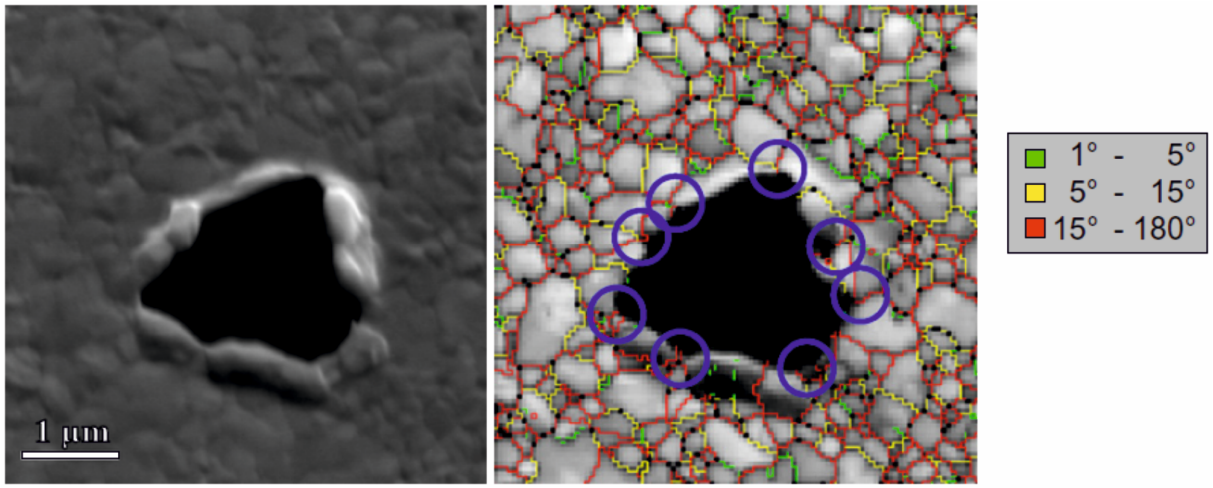


**Figure 14.** Crystal void in a 30 nm thick Au film which was annealed at 600 °C for 10 min. Substrate material was a p-type Si(100)/$SiO_2$/$SiN_x$ wafer which appears dark in SEM contrast. It is seen that the hole is surrounded by high-angle grain boundaries (marked by circles in the grain boundary map obtained by electron backscatter diffraction, EBSD). Reprinted from Ref. [24].

Such voids impinge and coalesce leaving isolated film material behind. There are several reasons for this fractal-like growth mode. For Au thin films, voids are found to extend into high-angle grain boundaries (Figure 14) and, for Pt thin films, abnormal grain growth around crystal voids is observed (Figure 15). From a kinetic point of view, grain boundaries are fast diffusion paths for vacancies and Au atoms which accounts for an accelerated void growth along these structures. Moreover, Pt film retraction slows down at grains having a low-index orientation relationship with the single crystalline substrate (which means a low interface energy). The interplay between both grain boundary diffusion and abnormal grain growth may facilitate void branching in polycrystalline thin films.

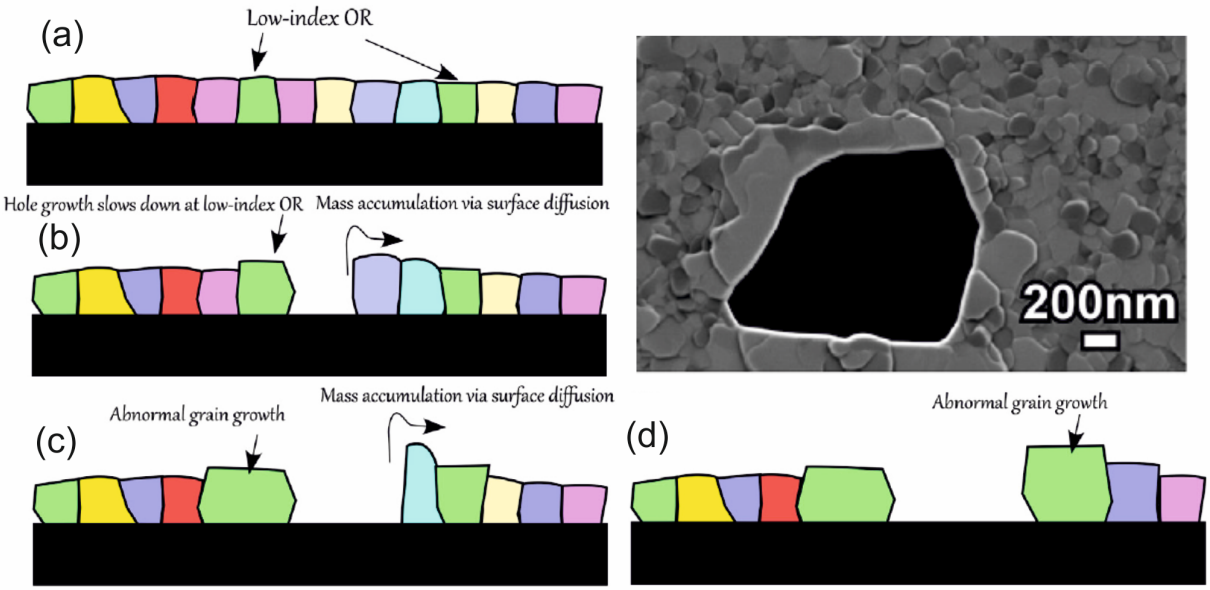


**Figure 15.** Abnormal growth of grains having low-index orientation relationship (OR) with the substrate. (a – d) Schematic representation of main steps of void evolution: Once a void has reached low-index OR grains, further void growth is inhibited due to an abnormal growth of that grain (compared to other grains in the remaining film). SEM micrograph showing terrace-like growth of grains at the edge of a Pt film void. Faceting is also apparent. The 50 nm thick Pt film deposited onto an a-plane oriented sapphire substrate was annealed at 800 °C for 2 h. Reprinted from Ref. [25].

Upon further void growth during ongoing dewetting, holes will eventually coalesce producing a network of interconnected film material. *Müller et al.* observed that void edges show crystallographic faces of the face-centered cubic Au, corresponding to a pronounced (111) texture being present in the thin film [24]. These rims also reveal uniform height which is characteristic of this dewetting stage. From Figure 16 it is apparent that elevated rims are those features that "survive" after holes have impinged each other.

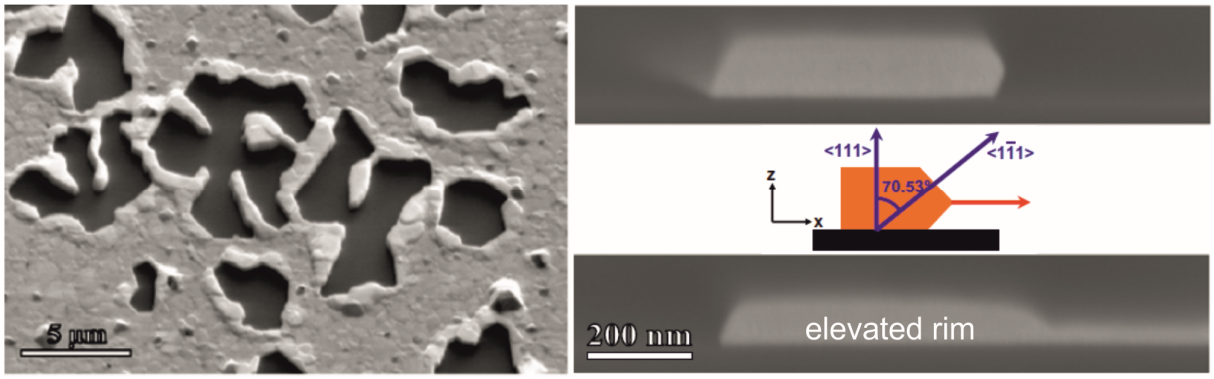


**Figure 16.** Void coalescence during dewetting in a 30 nm thick Au film upon annealing at 600 °C for 1 h. SEM image to the left displays film morphology. Small hillocks located in the remaining film can be observed. Faceted void rims of uniform height are highlighted by their cross-sectional profile to the right. The inset represents a void edge having crystallographic faces corresponding to (111) texture of the film. Reprinted from Ref. [24].

Another feature is the pronounced texture of the polycrystalline thin film. Upon dewetting it is found that texture evolution takes place [26]. In fact, the enhancement in texture contributes to surface energy minimization which is the main driving force for the dewetting. Commonly, this effect should not be a predominant condition for the dewetting itself because the thin film is highly textured before any annealing treatment. The relative alignment of grains in the course of dewetting can rather be associated with the characteristics of film voids. Statistical analyses show that it is those grains situated at the border of Au film voids that adjust their orientation (Figure 17). This indicates that void and grain growth strongly correlate. In summary, Figure 18 nicely depicts mechanisms associated with the dewetting of polycrystalline thin films. Initial coarsening occurs prior to the dewetting which is accompanied by texture evolution. Ongoing grain growth can be seen as a competing mechanism. Also grain rotation processes may be involved during texture sharpening. The transformation of a polycrystalline thin film microstructure into well-oriented particles/agglomerates defines the dewetting in solid state.

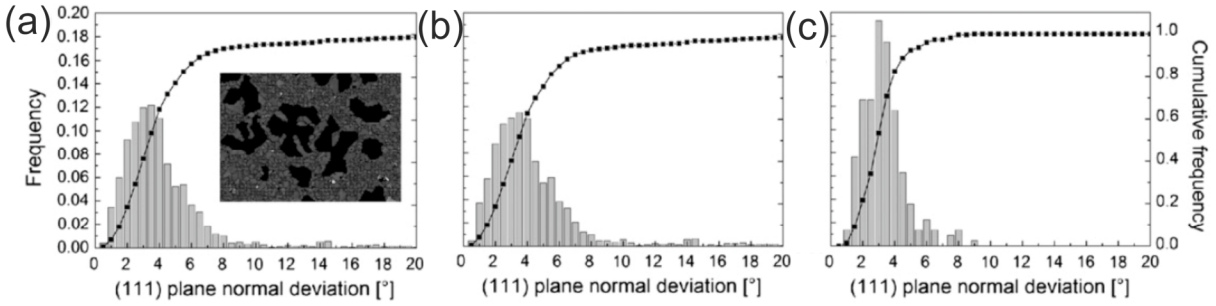


**Figure 17.** Grain orientation analyses during void coalescence in a 30 nm Au thin film annealed at 600 °C for 1 h. The angle of deviation between the (111) plane normal and sample normal direction is measured for (a) all the grains which are seen in the SEM image, (b) grains in the remaining film, and (c) grains around holes. Investigations were carried out by means of EBSD. Reprinted from Ref. [24].

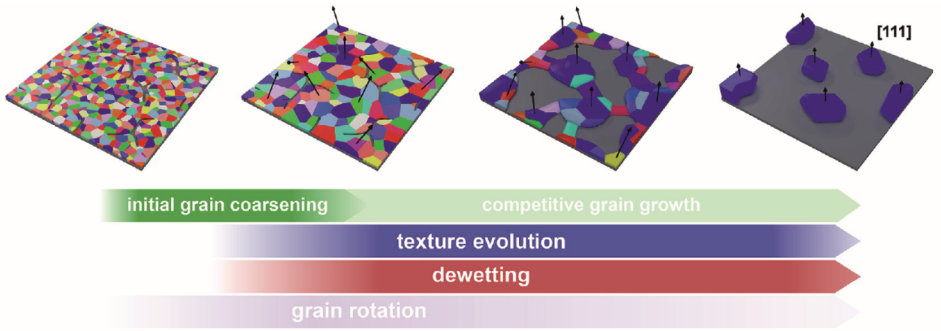


**Figure 18.** Illustration of processes associated with the dewetting of polycrystalline thin films. Color code displays out-of-plane orientation of grains. Arrows indicate [111] direction. Reprinted from Ref. [27].

### 2.5.2 *The role of grain boundary and film-substrate interface diffusion*

Diffusion paths being active during dewetting will determine morphology evolution of a thin film. While it is clear that surface diffusion is one possibility to reallocate film material, grain boundary and interface diffusion are also convenient kinetic paths. *Kovalenko et al.* studied Fe thin films with respect to this issue [28].

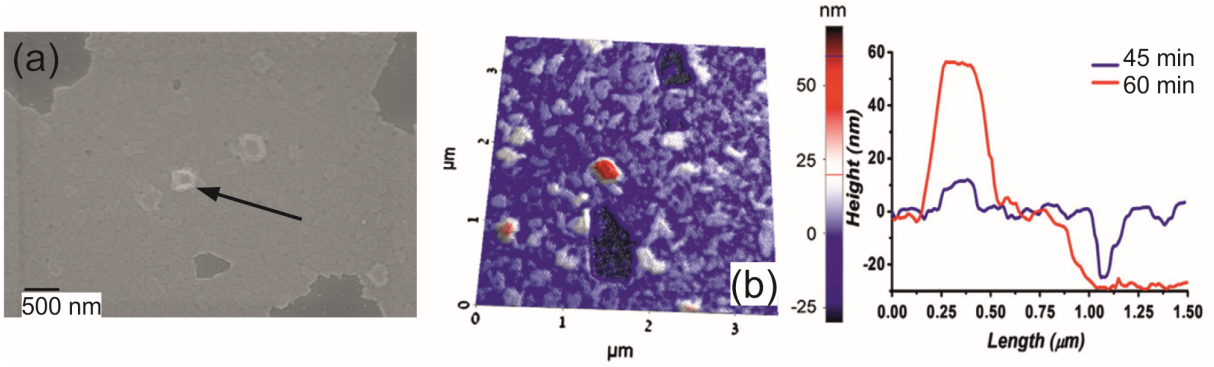


**Figure 19.** Hillock formation in α-Fe thin films annealed at 750 °C for 1 h. Film thickness was 25 nm deposited onto a basal plane, (0001)-oriented single crystalline sapphire substrate. (a) SEM image showing faceted hillocks off the position of crystal voids (as indicated by an arrow). It is also evident that elevated void rims are missing which would favor surface diffusion as the dominant mechanism. (b) AFM topographic imaging emphasizes that void growth as well as hillock formation correlate. Reprinted from Ref. [28].

Accumulation of Fe film material in the remaining film far away from holes suggests that surface diffusion is *not* the kinetic path being favored to form small hillocks, *i.e.*, elevated columnar grains. It is rather interface and grain boundary diffusion which are responsible for mass transport off the void, see Figure 19 and Figure 20. For a two-dimensional (real) polycrystalline thin film having a total thickness $h$, an effective diffusion coefficient can then be given as

$$D_{\text{eff}} = \frac{D_b h/w + D_i}{h/w + 1} \tag{12}$$

which is the weighted mean of grain boundary ($D_b$) and Fe-sapphire interface ($D_i$) diffusivities, assuming that mass flux goes along similar grains (having a width $w$) within the region limited by the average distance $U$ of the size of holes and hillocks (Figure 20b). In other words, Fe atoms will not circuit the hillock. Moreover, it is those hillocks that possibly act as nucleation sites for prospective particles at late stages of dewetting.

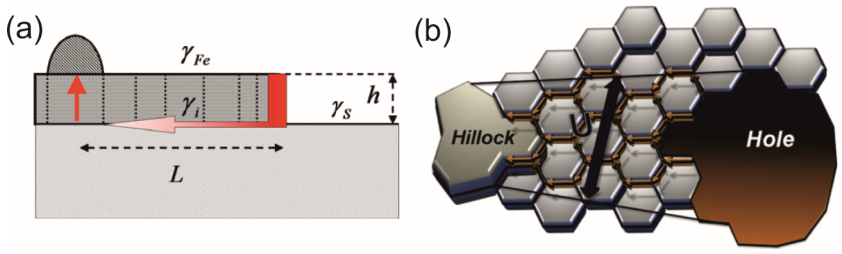


**Figure 20.** Modeling the formation of hillocks in polycrystalline α-Fe thin films for (a) 1-dimensional case, (b) 2-dimensional situation. It is assumed that diffusion along the film-substrate interface as well as along grain boundaries is dominant. In the 1-d scheme, $L$ is the distance between the edge of a void and the elevated grain; $\gamma_i$, $\gamma_{Fe}$, and $\gamma_S$ are corresponding interface as well as surface energies. Reprinted from Ref. [28].

At this point, another case showing the complex interplay of surface, interface, and grain boundary diffusion is addressed. During void initiation via grain boundary grooving (see Figure 8) it is assumed that surface diffusion (and/or evaporation-condensation) is the major mechanism behind the shape of a groove profile at early stages of dewetting. Actually, this one-sided display of what happens to thin films attached to a substrate neglects the fact that the film-substrate interface may act as a reservoir for mass accumulation as well (and not only the free surface). Such a mechanism would implicate thickening of the film which is indeed observed for a Ni thin film annealed at 700 °C. Ni atoms diffuse along the film-substrate interface increasing the original height level of the film (region 2 in Figure 21). In order to fulfill mass conservation, pile-up of film material at the edge of a groove is suppressed (region 1). However, overall grain growth as well as phase transformations within the thin film during annealing may also increase film thickness at early stages of the dewetting.

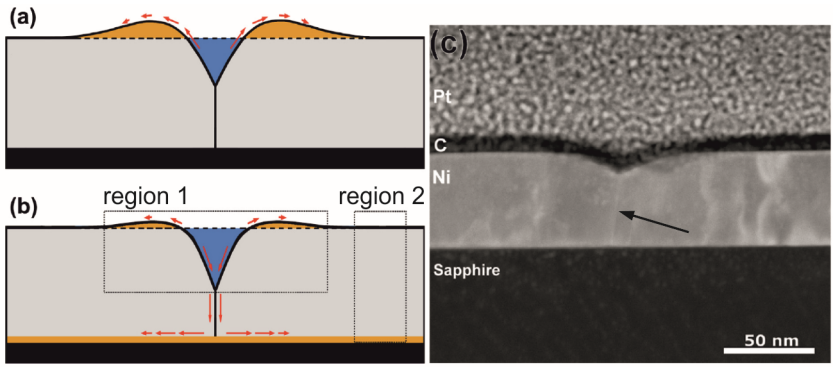


**Figure 21.** Grain boundary grooving revisited. It is plausible that surface diffusion is not the only mechanism which may contribute to void formation via thermal grooving. (a) Sketch of a classical profile solely based on surface-diffusion, (b) flattened groove profile due to mass accumulation at the film-substrate interface, (c) Cross-sectional view of an actual groove using TEM imaging. Initial thickness of the Ni film was 40 nm deposited onto a c-plane, (0001)-oriented single crystalline sapphire substrate. The grain boundary is indicated by an arrow. Reprinted from Ref. [29].

### 2.5.3 *Annealing atmosphere*

For the sake of completeness, the influence of the annealing atmosphere thin films are treated with is briefly introduced. At first glance, it is not obvious why the atmosphere should have any effect on the dewetting (apart from the ability to prevent the thin film from oxidation and/or contamination during annealing). Growth rates of film voids should be solely governed by the temperature. However, it can be expected that the *geometry* of dedicated film voids may depend on ambient conditions. For Au thin films, this shape effect becomes visible by the degree of surface energy anisotropy, resulting in more a less pronounced branched voids (Figure 22).

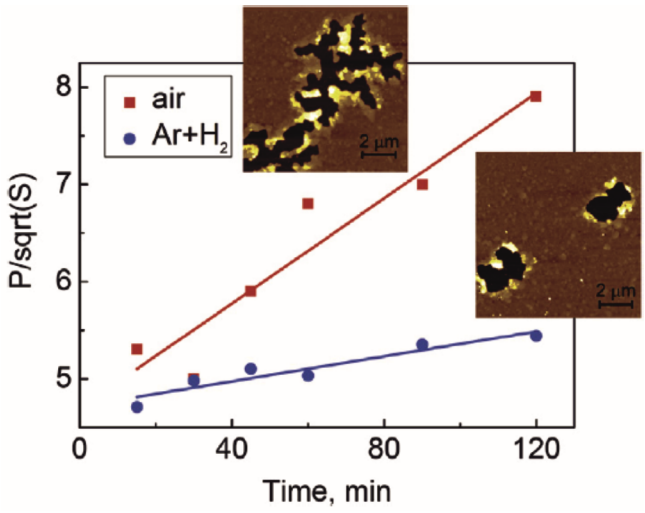


**Figure 22.** Shape effect due to different ambient conditions. A 25 nm thick Au film deposited onto c-plane oriented sapphire substrate was annealed at 400 °C in ambient air and forming gas (Ar-10%$H_2$), respectively. A dimensionless parameter $P/\sqrt{S}$ is introduced to trace shape evolution of film voids: $P$ is the perimeter, $S$ the projected area. This parameter amounts to $2\sqrt{\pi}$ (about 3.5) for circular holes and tends to infinity for elongated, very narrow holes. Insets: AFM topographic images showing voids which formed after 180 min in air or forming gas. Reprinted from Ref. [30].

A reasonable explanation for the difference in morphology evolution is that surface adsorbate states may change surface energy anisotropy. The higher the degree of anisotropy, the higher the fraction of atomically flat faces, thus making holes expand more isotropically.

To sum up, void growth mechanisms are shown to reveal individual characteristics which depends on many parameters. The most important one is, apart from the substrate and film material itself, the crystalline state the dewetting starts from. Grain boundaries (together with the film-substrate interface) are emphasized to play a major role in dewetting kinetics. Also, abnormal grain growth is shown to affect void evolution in polycrystalline metal thin films. Secondary factors such as ambient conditions can be used to alter void characteristics.

## 2.6 Final stages of solid-state dewetting – particle formation

This section is dedicated to the question how particles formed via solid-state dewetting will equilibrate. Dewetting of polycrystalline thin films is accompanied by grain growth. Finally, single or bi-crystal particles having various shapes will form. Upon equilibration, parameters such as the film and substrate material (*i.e.*, surface and interfacial energy) play a major role. Another influencing parameter is the annealing treatment performed which may even lead to unprecedented shapes.

### *2.6.1 Equilibrium crystal shape (ECS)*

From a thermodynamic point of view, the equilibrium crystal (or WULFF) shape will be the favorable habitus according to the GIBBS condition

$$\sum_{i=1}^{N} \gamma_i a_i = \text{Min.} \tag{13}$$

At equilibrium, this variational problem is solved by the WULFF theorem which is depicted in Figure 23 for a 2-dimensional case. Due to surface energy anisotropy being present in solid-state, each direction in space has a particular surface energy $\gamma_i = \partial G / \partial a_i$ which is represented by the radial distance from the origin in a polar plot. The specific surface area $a_i$ being occupied for a certain direction in space derives from the $\gamma$ plot in such a way that minimum surface energy is favored. Isotropic surface energy would result in a sphere as the only habitus. In solid-state, however, orientation dependence of surface energy may form even complex polyhedral shapes.

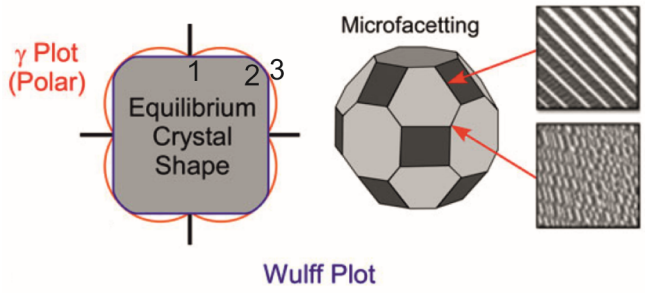


**Figure 23.** 2-d WULFF construction and 3-d habitus of a face-centered cubic (fcc) crystal. The WULFF plot or ECS results from the $\gamma$ plot. The inner planes (belonging to a set of smallest $\gamma$) generate the equilibrium shape which may reveal faces (1, atomically flat) and curved surfaces (2, rough). Any singularity (3, discontinuous connection in the WULFF plot) means that respective orientations become unstable and decompose into micro-faces as shown by AFM micrographs to the right. Reprinted from Ref. [13].

Another question is what happens in the presence of a rigid substrate on which particles/crystals are attached. The WINTERBOTTOM analysis deals with this issue depicted in Figure 24. Here, the so-called $\gamma$-interfacial vector with magnitude $\gamma_{CS} - \gamma_{SV}$ which is the energy difference of the crystal/substrate and the substrate/vapor interfaces has to be considered. This vector then determines the energetically favorable position of the underlying substrate. A more rigorous examination can be found elsewhere [13].

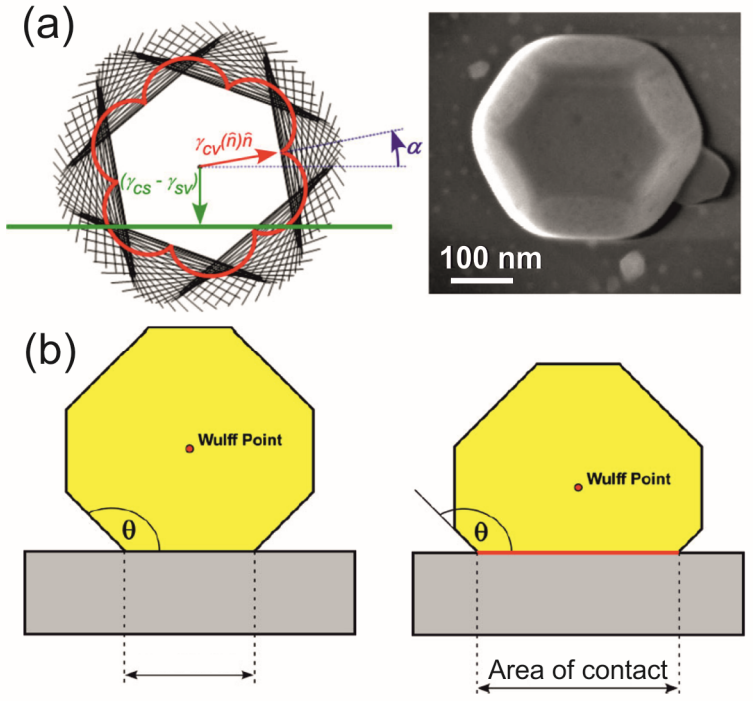


**Figure 24.** Equilibrium shape and the role of a substrate. (a) 2-d WINTERBOTTOM construction to achieve ECS in the presence of a flat rigid substrate. SEM micrograph showing an actual crystal habitus of an Au nanoparticle equilibrated at 950 °C after 120 h. The shape corresponds to a truncated octahedron with one of the (111) faces on top. (b) Actual area of contact is further influenced by effects such as segregation (which is represented by a red line at the particle-substrate interface), thus altering the magnitude $\gamma_{CS} - \gamma_{SV}$ of the $\gamma$-interfacial vector. This is why measuring contact angles is not sufficient in solid-state. Reprinted from Refs. [10, 13].

### *2.6.2 Metastable shape formation*

In practice, however, it is less likely that the above mentioned methods accurately predict an actual crystal habitus since many factors such as segregation, supersaturation, or supercooling will affect growth rates along particular orientations. Therefore, size and shape stability of particles formed through thin film dewetting is a field of interest to reveal concomitant features.

Once single crystal faceted particles have formed, their further equilibration is assumed to be hindered due to difficulties in forming surface steps on atomically flat, singular faces. This is why even metastable shapes can be observed which clearly differ from corresponding ECS (see Figure 25).

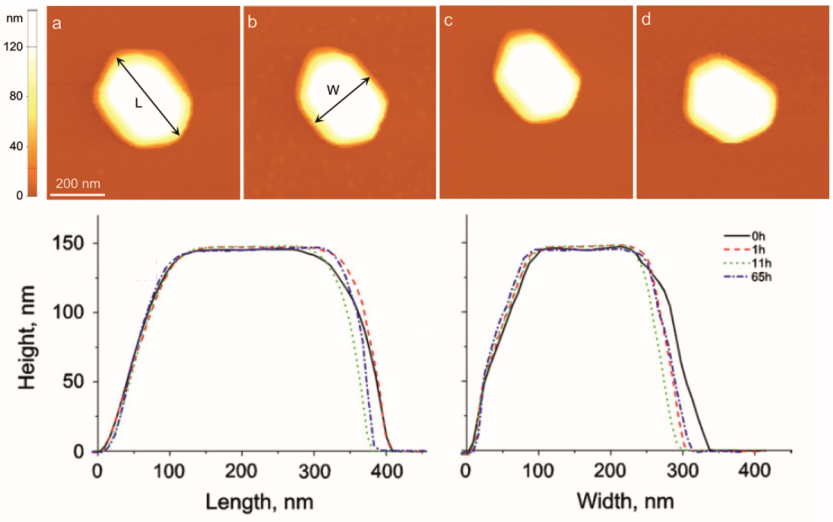


**Figure 25.** Elongated single crystal Au nanoparticle formed via solid-state dewetting of an Au thin film on sapphire. AFM micrographs show its size and shape evolution upon post-annealing at 950 °C in air for different durations, (a) initial particle after dewetting, (b) after 1 h, (c) 11 h, and (d) 65 h. Height profiles taken along the length (L) and width (W) of the particle confirm its metastable shape. Reprinted from Ref. [31].

Different behavior is found for bi-crystal nanoparticles. Here, grains seem to rotate and self-align in such a way that particles no longer show kinking (resulting from the grain boundary inside the particle, Figure 26). A kinetic model was developed by *Malyi et al.* to describe this "rotation" mechanism [31]. The grain boundary (GB) is assumed to move out of the particle due to its high mobility near the melting point of Au (1064 °C), leaving non-singular, *i.e.*, atomically rough side surfaces of the former grain. Surface-curvature-driven surface diffusion then transforms the single crystal into its final (metastable) shape solely containing singular (faceted) sides.

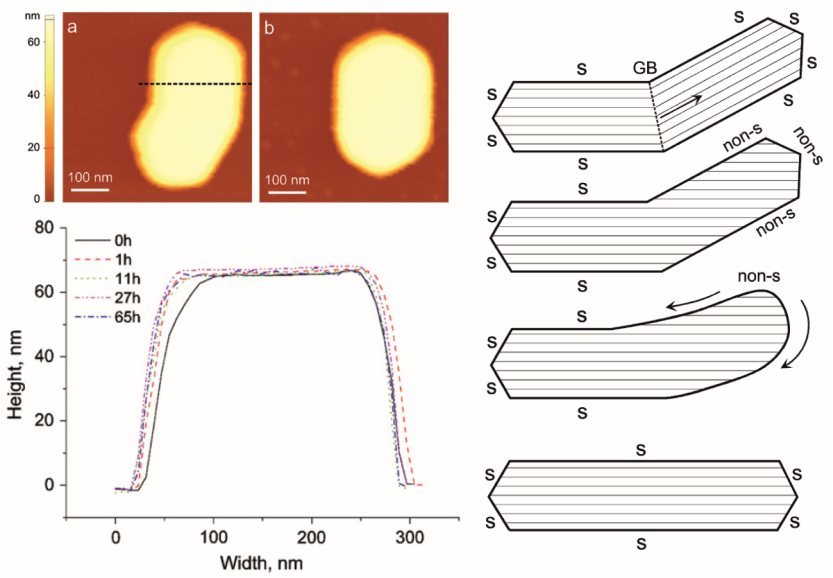


**Figure 26.** Grain rotation in a bi-crystal Au nanoparticle upon annealing at 950 °C in air. (a – b) AFM micrographs exemplarily show the self-alignment already after annealing for 1 h. Height profiles are taken along the upper grain (dashed line) at different durations. The scheme to the right illustrates how grains may align in order to eventually form a single crystal particle. Singular (s) as well as non-singular (non-s) surfaces will play a role in the transformation process. Reprinted from Ref. [31].

In another study, however, it is impressively shown that defects which are introduced by plastic deformation may drive nanoparticles into a more pronounced equilibrium shape upon thermal activation, see Figure 27. The reason is that defects such as dislocations provide plenty of nucleation sites for the transformation process. To sum up, statements made in this section underline the fact that particle formation in the course of dewetting is, in solid-state, a quite complex issue even for the same material.

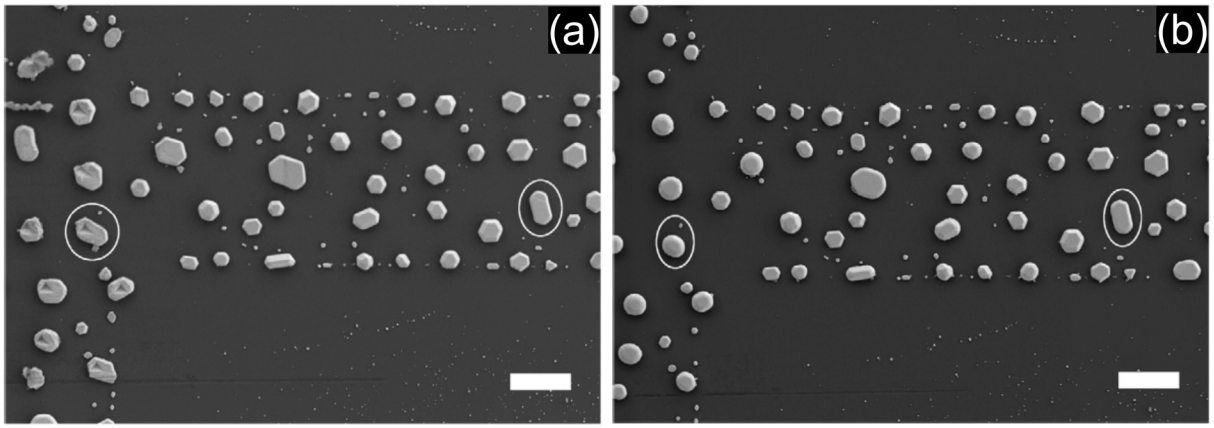


**Figure 27.** Defect-induced equilibration of Au nanoparticles on sapphire: (a) initial state after dewetting of the Au thin film, some of the particles (located on the left part of SEM micrographs) were subject to indentation, (b) post-annealing at 900 °C for 1 h in ambient air. It is seen that mechanically stimulated particles transform from elongated into equiaxed crystals whereas other particles uphold their metastable shape. Scale bars are 2 µm. Reprinted from Ref. [32].

### *2.6.3 Size distribution and mean particle size*

From a global point of view, all the particles formed via dewetting are to be considered as a statistical unit having a mean size.

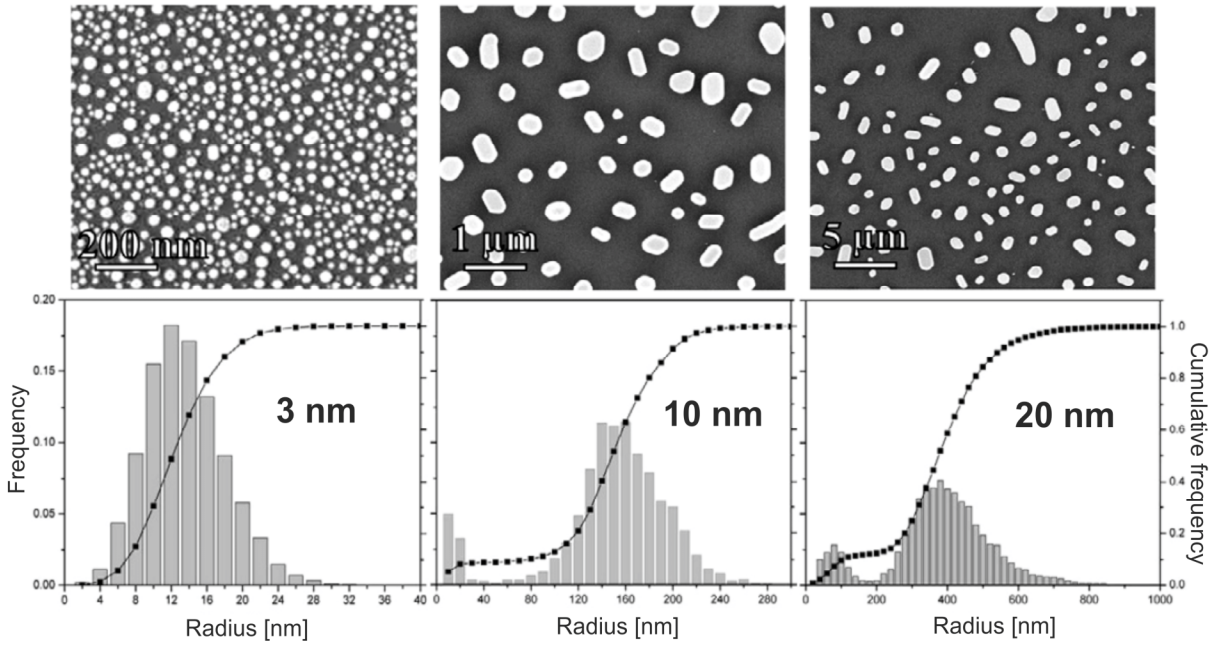


**Figure 28.** Particle size distributions of Au micro- and nanoparticles formed via solid-state dewetting of thin films in air at 950 °C for 10 min. An increasing initial film thickness, as labeled in bar charts, increases mean particle size after dewetting (assuming spherical shape). Reprinted from Ref. [10].

Figure 28 shows that initial film thickness is the most important parameter to tune particle dimension: Obviously, the thicker the film, the bigger the particles. However, it is found that thicker films may also form bimodal size distributions with one mean being a measure of a substrate defect spacing (Figure 29). In other words, surface roughness or any irregularities of the substrate being used may result in a kind of fingerprint which will become visible in the bar chart if the former film is thick enough.

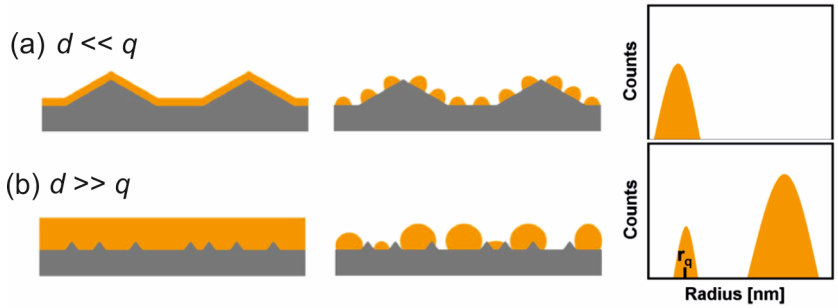


**Figure 29.** Schematic. (a) If film thickness $d$ is too thin, the dewetting will not be affected by any irregularities (the substrate defect spacing $q$) of the film-substrate interface, thus showing a monomodal size distribution of particles formed. (b) If the film is thick enough, a bimodal distribution will be present with one mean being a measure of $q$. Reprinted from Ref. [10].

Upon further annealing, additional effects come into play. Ripening and evaporation during long-term annealing are the most significant ones since the interplay between size-increasing (coarsening) and size-decreasing (evaporation) effects will determine whether mean particle size shrinks or increases. The former one may become important for particles lying very close together. If the evolution of the particle size remains constant, a certain balance between both processes can be assumed. For Au thin films, investigations show that such effects indeed alter particle characteristics which is depicted in Figure 30. At this point, the question whether an average size is predictable for particles formed via solid-state dewetting or not is hardly answered. In fact, even for the same film material, substrate quality and annealing conditions do have an impact on particle size distributions. This might be one reason why there is no general analytical relation between film thickness and mean particle size in solid-state.

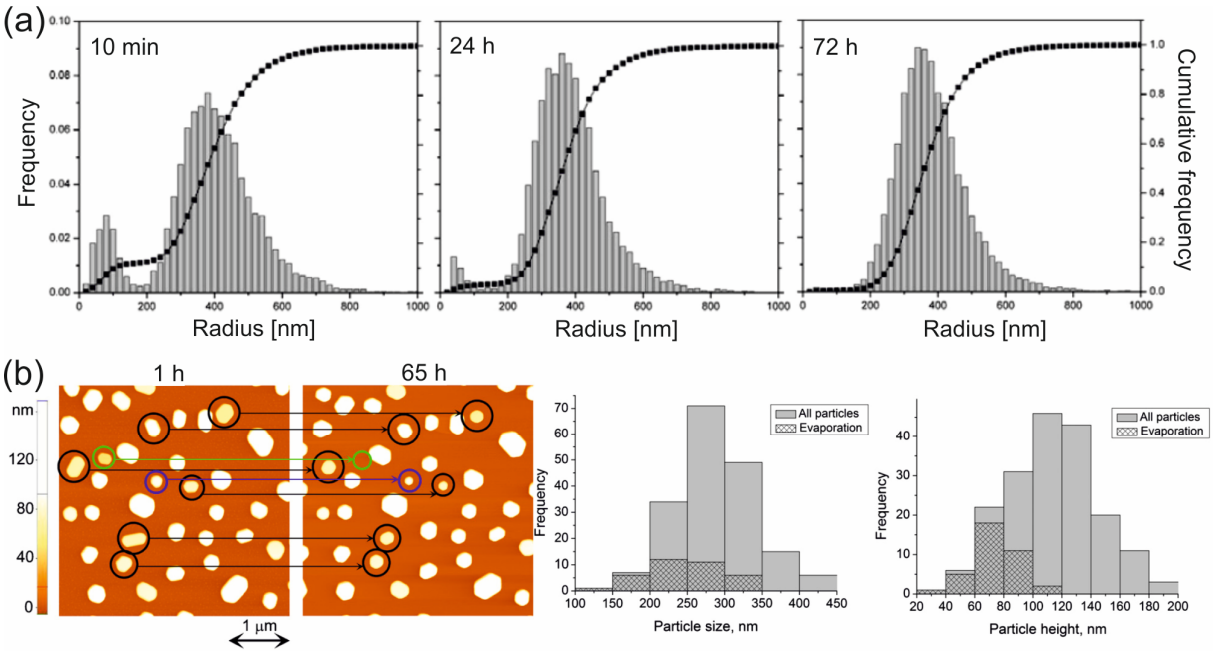


**Figure 30.** Au particle size evolution upon isothermal annealing at 950 °C. (a) Initial film thickness was 20 nm. Size distribution narrows with increasing duration and turns into a monomodal, log-normal one after 72 h. (b) Shrinking and even vanishing (see the smaller particle marked by green color in AFM topographic images) Au particles due to evaporation effects. Initial film thickness was 14 nm. Reprinted from Refs. [10, 33].

## 2.7 Solid-state dewetting of multicomponent thin films

Previous sections show that dewetting (and dedicated particle formation) of one-component thin films is a comprehensive field of research, however, in order to exploit the effect of alloying, bi- or multicomponent thin films could be an advanced approach to study the dewetting in solid-state, see Figure 31. Thermodynamics of alloys will play a key role for the thermal stability of thin solid films. Segregation, different dewetting kinetics of the set of compounds being under consideration, or even chemical aspects such as surface reactions may provide an additional set of parameters for the dewetting.

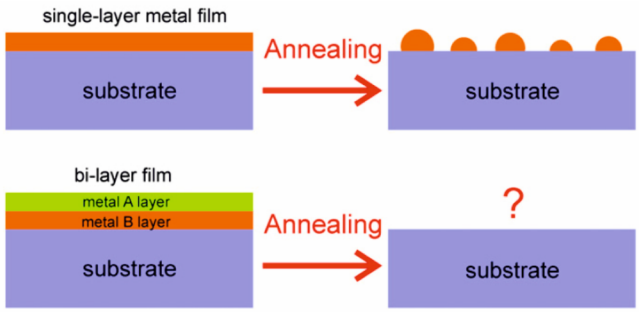


**Figure 31.** Schematic of what may happen to multicomponent thin solid films upon dewetting [1].

### *2.7.1 Metallic bi-layer and alloy thin films*

Several binary systems has been the subject of dewetting experiments. For instance, it is found that morphology and dewetting rate of the miscible Co-Pd system lie in between that of individual components [34]. Ag-Ni thin films changed their void growth mode from longish gaps (pure Ni) to fractal-like void pattern by adding the immiscible Ag [35]. Investigations on Fe-Pd thin films are also available [36]. This section is dedicated to studies that reflect on the thermal stability of thin solid films.

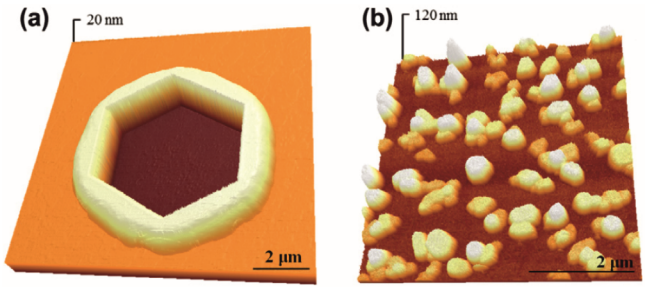


**Figure 32.** Enhanced thermal stability of an alloy thin film. (a) AFM micrograph of a film void in the unperturbed Au-Fe thin film, (b) fully disintegrated Au film, both deposited onto c-plane, (0001)-oriented single crystalline sapphire and annealed at 650 °C for 7 h. Reprinted from Ref. [37].

*Amram et al.* report on Au/Fe bi-layer thin films which are found to be quasi-single crystalline upon deposition via e-beam evaporation, *i.e.*, grain size is orders of magnitude larger than film thickness [37]. The intriguing finding why the bi-layer is not polycrystalline can be related to the Fe which is known to adopt an fcc structure in ultrathin films. Compared to $Au/Al_2O_3$, Fe may act as a kind of seed layer which decreases the misfit between the film and the substrate material and which increases the adhesion energy [38]. Moreover, nucleation conditions of the Au top layer will be changed facilitating heteroepitaxial growth during deposition.

At 650 °C, the **Au-Fe** alloy forms homogeneous solid solutions. It is plausible that the *thin film* completely homogenizes before the initiation of dewetting. In other words, the incubation time for void initiation $t_i$ exceeds the dissolution time of the bi-layer, $t_{diss} << t_i$. Hence it follows that void formation is expected to be much more difficult compared to a polycrystalline Au film having similar thickness: The lack of defects may hinder void nucleation and/or thermal grooving in the single crystalline, homogeneously distributed Au-Fe alloy film. Figure 32 visualizes the considerable thermal stability of the Au-Fe film.

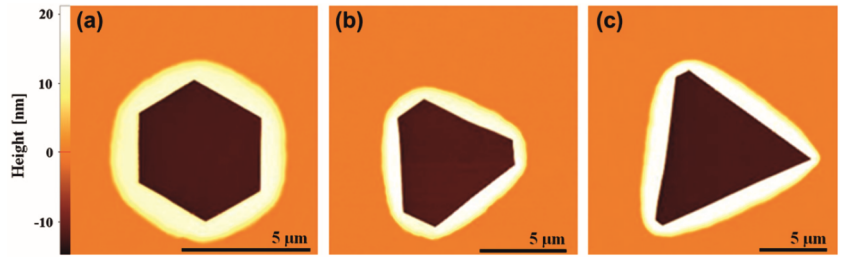


**Figure 33.** Anisotropic void growth in Au/Fe bi-layer thin films on sapphire upon annealing at 650 °C for (a) 7 h, (b) 15 h, and (c) 24 h. Initial thickness of individual layers was 3 nm (Fe, ground layer) and 9 nm (Au, top layer) which corresponds to Au-32 at.% Fe. From AFM topographic images it is seen that void shape transforms from a hexagon into a triangle due to diffusion anisotropy along respective faces, $D_{111} > D_{100}$. Reprinted from Ref. [37].

Upon annealing, symmetrically shaped voids showing strong edge faceting evolve from hexagonal into triangular shape (Figure 33). The presence of alternating {100} and {111} faces can be associated with the ECS of Au. For energetic reasons it is thus expectable that Au atoms relocate toward the free surface of the alloy film. To sum up, this study emphasizes the role of a thin (Fe) interlayer in the dewetting characteristics of Au thin films. Another study is presented by *Müller et al.* that reflects on the effect of alloying small amounts of Pt to Au [15]. At equilibrium, this binary system also forms solid solutions. Upon annealing at elevated temperature the influence on the dewetting can be demonstrated. Figure 34 shows that solid-state dewetting is delayed for **Au-Pt** alloy films. Void formation is clearly suppressed even after

several hours at 500 °C. From a kinetic point of view, this is due to the fact that alloying Pt to Au lowers the diffusivity of the Au-Pt alloy formed and, therefore, the dewetting of the alloy film is kinetically hindered at this temperature [39].

Both studies reviewed here show that the dewetting of multicomponent thin films reveals even new features due to alloying. Thinking of the large number of **Au-**based alloys, it is not astonishing that a huge "playing field" is entered. In this thesis, parameters such as stacking sequence and individual layer thickness (which determines the alloy composition) will be assessed. Phase formation will also be pointed out to critically affect the dewetting in Au-Ni thin films.

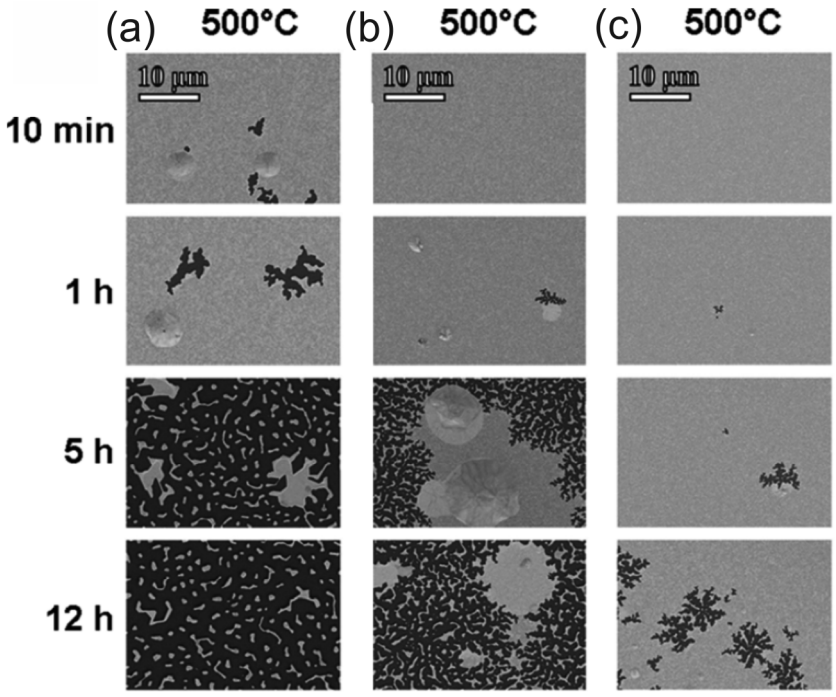


**Figure 34.** SEM morphology maps of Au and Au-Pt alloy thin films deposited onto a p-type $Si(100)/SiO_2/SiN_x$ wafer: (a) 19.6 nm pure Au, (b) 21.1 nm Au-3.7 wt.% Pt, (c) 19.7 nm Au-8.6 wt.% Pt. It is clearly seen that the dewetting will delay if Pt content rises. Reprinted from Ref. [15].

### *2.7.2 Phase formation in micro- and nanoparticles*

Recently, more and more scientists have recognized the great potential of bi- or multicomponent thin film dewetting in order to exploit both size *and* composition for the synthesis of functional micro- and nanoparticles. Moreover, the dewetting method combines high throughput with the ease of handling which makes this technique useful even on an industrial scale. Time-consuming chemical treatments are usually not needed. Thus, self-assembly of thin solid films provides a cost-effective and simple way to design tailored *alloy* nanostructures [40-44]. This section introduces fundamental experimental studies on the

formation of bi-metallic micro- and nanoparticles via dewetting exploiting physical principles at reduced scale. The interesting question of how phases will arrange in ***alloy*** mirco- and nanoparticles is pointed out.

- *Au-Co nanoparticles (NPs)*

  The Co-Au binary system is characterized by its large miscibility gap in solid state. However, mutual solubility increases above ~422 °C since Co changes its crystal structure from hexagonal close packing (hcp) to the fcc type (see Figure 35). This is why the particles formed by thin film dewetting should contain Au-rich and Co-rich phases. Starting from a 25 nm thick Au-Co bi-layer annealing-induced dewetting forms dumbbell-shaped, bi-metallic NPs.

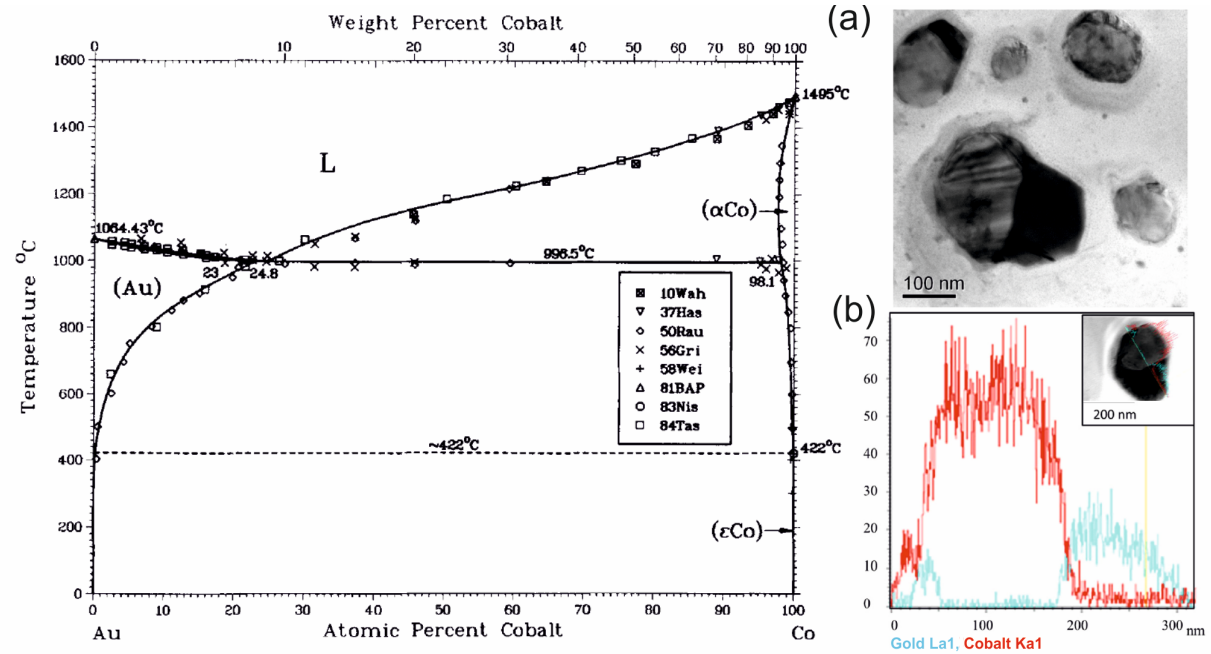


**Figure 35.** Assessed phase diagram for Au-Co, including experimental data. Mutual solubility increases above the allotropic transformation temperature of Co. To the right: (a) TEM micrograph of Au-Co bi-metallic NPs showing faceted Au-rich and Co-rich phases. Due to its strong scattering power, Au-rich regions appear darker in contrast. Individual layer thickness of Au (10 nm) and Co (15 nm) corresponds to an overall composition of about 69.8 at.% Co. The bi-layer film was annealed at 800 °C for 2 h in order to obtain alloy NPs. (b) Limited solubility of Au in Co (~1%) and Co in Au (~9%), respectively, is retained to room temperature (confirmed by EDS). Reprinted from Refs. [34, 45].

- *Au-Ni NPs*

  Similar behavior is found for Au-Ni particles formed via dewetting of bi-layer thin films. Due to the large lattice mismatch of about 15% [46], the Au-Ni binary system reveals a miscibility gap which covers the entire concentration range at room temperature (see Figure 36). These characteristics make this binary alloy very

interesting because one can adjust any stoichiometry (*e.g.*, by changing the thickness ratio of the corresponding bi-layer film) at high temperature. The cooling rate then determines how much of the solid solution is able to decompose, *i.e.*, fast cooling or quenching will enable a supersaturated state whereas slow cooling will separate particles into Au(-rich) and Ni(-rich) regions. Therefore, cooling also impacts the shape of the alloy particles.

The study presented at this point reflects on the influence of annealing temperature and total film thickness. Alloy composition (39 at.% Au) was not changed. Slow cooling was applied in order to trace the decomposition into Au and Ni at room temperature. Annealing above the miscibility gap (and subsequent slow cooling) lead to spherical alloy particles revealing faceted Au-rich and Ni-rich regions. At 650 °C, corresponding phases already form during annealing because this temperature crosses the miscibility gap. Then, at room temperature, also dumbbell-shaped, bi-metallic NPs are formed which reveal even symmetric arrangements of Au-rich and Ni-rich phases in individual particles.

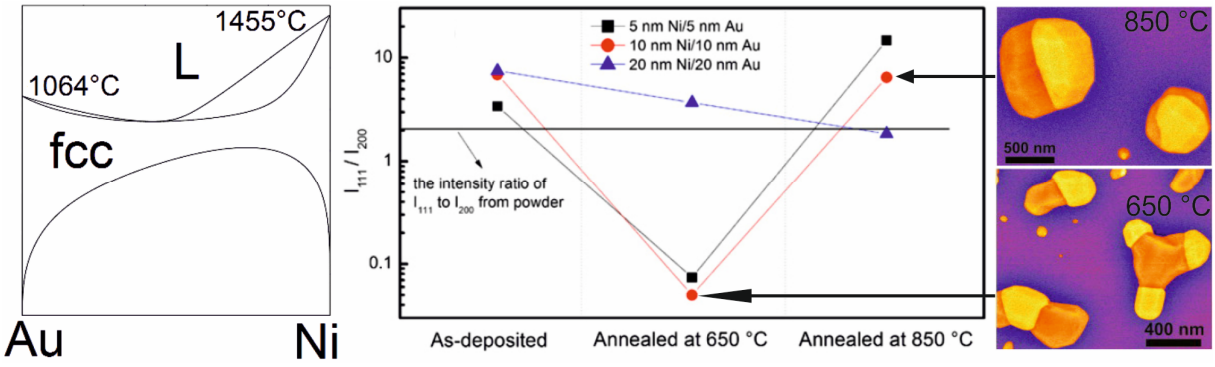


**Figure 36.** Sketch of the equilibrium Au-Ni phase diagram showing the miscibility gap and the high-temperature fcc solid solution regime. Melting temperatures of Au and Ni are indicated to facilitate reading. To the right: Intensity ratio $I_{111}/I_{200}$ of the Au-rich phase obtained from XRD measurements. Depending on the annealing temperature, pseudo-color SEM images show that, upon annealing for 1 h, different particle shapes are formed. The change in texture can be related to surface as well as strain energy minimization in the course of forming bi-metallic NPs [1].

A plausible explanation for these observations can be associated with the large lattice mismatch which causes the particles to be elastically strained. At 850 °C, formation of homogeneous solid solutions enables a more spherical, equiaxed crystal shape due to surface energy minimization. Then, during cooling, phase arrangement is *confined* by the pre-defined shape. This is why texture of the particles is similar to that of the as-deposited bi-layer film. At 650 °C, however, Au-rich and

Ni-rich phases has to form during the dewetting process. Resulting particle shapes are expected to be governed rather by strain energy reduction which then relates to a change in texture (see Figure 36). This effect becomes less important with increasing bi-layer film thickness. If there is a critical value for film thickness is hard to say due to the great number of factors associated with the dewetting.

- *Ag-Au NPs*

  This binary system forms solid solutions in sold-state for all the compositions, *i.e.*, is completely miscible (thus, there is no need to depict the respective equilibrium phase diagram). Starting from a bi-layer thin film, Ag-Au alloy NPs can be easily obtained via the dewetting route (see Figure 37). Here it is found that the shape of the particles differs from classical ECS of fcc crystals which is probably due to the formation of solid solutions: A homogeneous distribution of Ag and Au atoms may promote spherical particles. Subsequent *dealloying* of the Ag then results in the formation of nanoporous Au NPs, using a nitric acid (65 wt.% $HNO_3$ solution at 21 °C) to remove the Ag. The specific surface area can be estimated by an analytical expression

$$A_S = \frac{(1/s^2)0.5\pi d_P^2}{\rho t} \tag{14}$$

  which connects initial bi-layer film thickness $t$ and density of Au $\rho_{Au}$ with NP characteristics (mean particle size $<d_P>$ and their characteristic spacing $s$). The latter can be obtained from autocorrelation-based image analysis [47]. The combination of the dewetting method with subsequent dealloying introduces a simple and cost-effective way to fabricate catalytically highly active Au NPs having a specific surface area $A_s$ which is $10^4$ (!) times larger than their *bulk* nanoporous counterpart.

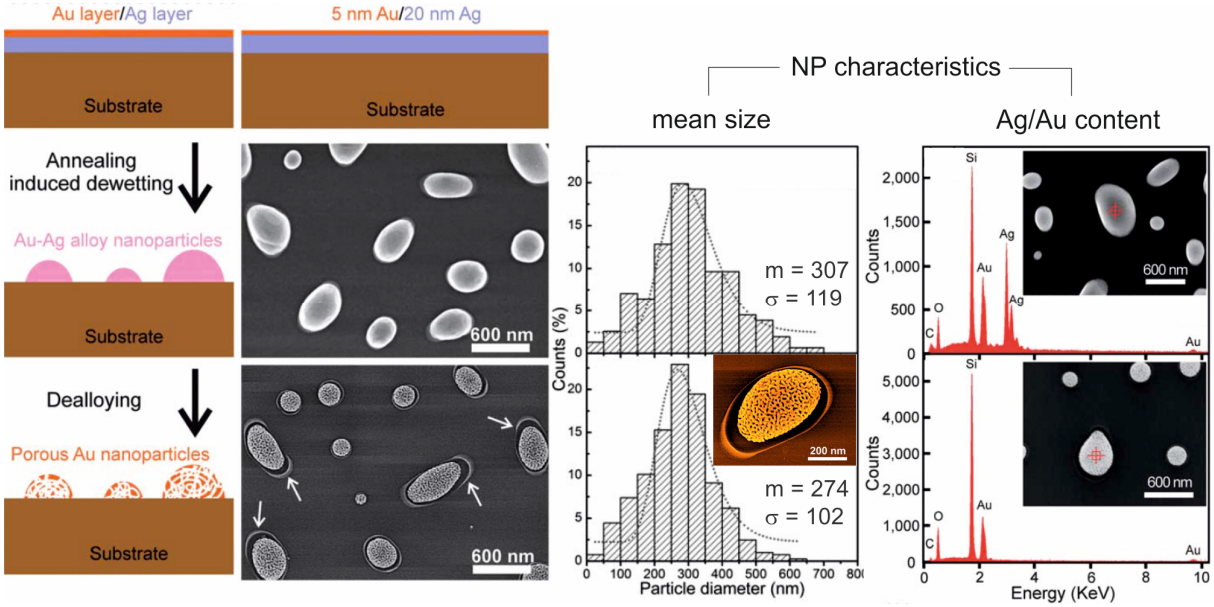


**Figure 37.** Dewetting and dealloying. Individual layer thickness of Au and Ag determines the overall composition (thickness ratio). In the present case, the 5 nm Au/20 nm Ag bi-layer thin film corresponds to ~20 at.% Au. Ag-Au alloy NPs are formed via dewetting at 900 °C in Ar for 15 min. Subsequent dealloying of the Ag results in the formation of nanoporous Au NPs. After wet chemical treatment, contours of former alloy particles (as indicated by arrows) are clearly seen in SEM images. NP characteristics before/after dealloying are also shown. It can be seen that particle size distribution is slightly changed due to the mass deficit upon dealloying. Mean ($m$) and standard deviation ($\sigma$) of a log-normal fit are given. EDS point analysis of selected particles approves that Ag is not detectable anymore [47].

- *Au-Fe micro- and nanoparticles*

  This Au-based binary alloy is quite similar to other combinations with *3d*-transition metals (see Au-Co and Au-Ni). There is a large miscibility gap at medium temperatures and a broad solid solution ridge for Au-rich alloys. However, the allotropic transformation of Fe ($\alpha \leftrightarrow \gamma \leftrightarrow \delta$) influences phase formation for Fe-rich alloys. For example, there is an eutectoid transformation at 868 °C for $(\gamma Fe) \leftrightarrow (\alpha Fe) + (Au)$. A reliable approach to study phase transformations in micro- and nanoparticles is conducting bi-layer thin film dewetting in the solid-solution regime. This means micro- or nanoparticles consisting of Au-Fe solid solutions are formed. Subsequent annealing at lower temperature then induces particles to separate into Au-rich and $\alpha$-Fe phases according to the equilibrium phase diagram (Figure 38). However, as mentioned in previous sections, size and shape stability of *single crystalline* NPs is associated with the difficulty in forming steps on atomically flat faces. The area density of surface mobile atoms is decreased. This is why

precipitation of a second phase on such facets might be challenging. In turn it is plausible that facet edges act as favorable nucleation sites which may result in a certain symmetry of phase arrangement. This is clearly visible in Figure 38 and quite contrary to respective bulk materials.

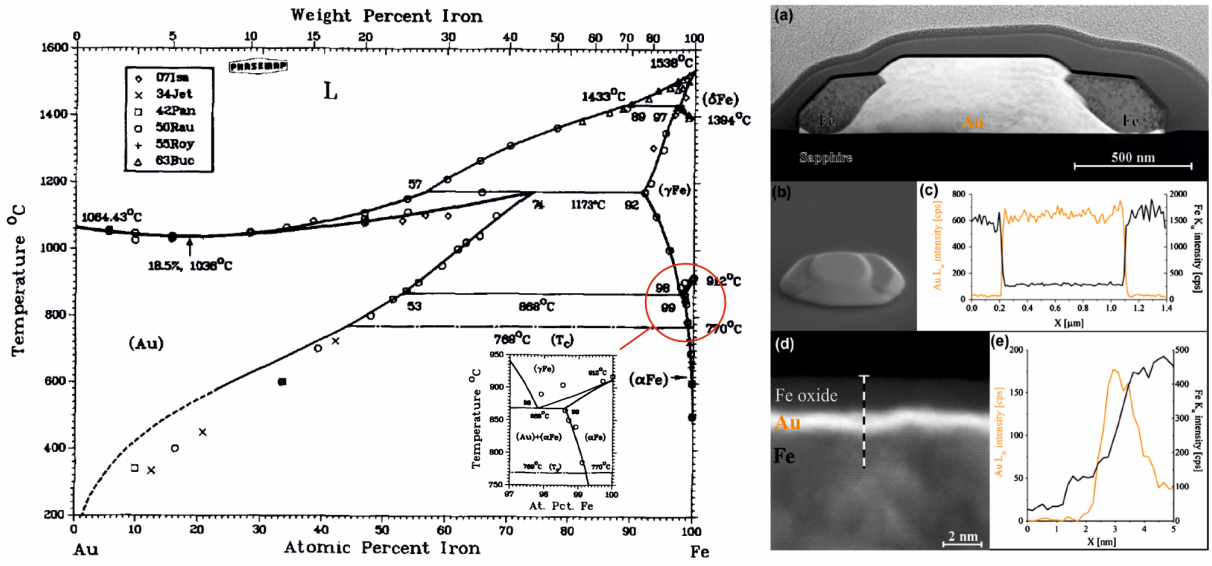


**Figure 38.** Assessed phase diagram for Au-Fe, including selected experimental data. The insert magnifies the $\gamma$-Fe ↔ $\alpha$-Fe transition. To the right: Phase transformation in Au-Fe microparticles obtained by dewetting of an Au/Fe bi-layer at 900 °C for 24 h. The thin film was deposited onto a sapphire substrate. Subsequent annealing at 600 °C for another 24 h induces phase separation. Initial composition (thickness ratio of the 11 nm Au/9 nm Fe bi-layer) corresponds to 54.1 at.% Fe. (a) Cross-sectional view using Z-contrast imaging (high-angle annular dark-field (HAADF) STEM mode). Fe precipitates are clearly seen to be neither completely inside nor outside the host particle. (b) SEM side view of the former particle. (c) EDS analysis across the particle in (a). (d) and (e) High-resolution micrograph of the topmost region of a Fe precipitate. It is seen that the Fe precipitate is covered by an Au-rich segregation layer (which is approved by EDS). The thin Fe oxide layer was verified using electron energy loss spectroscopy, EELS. Reprinted from Refs. [45, 48].

Another intriguing observation is a thin Au(-rich) *segregation layer* covering facets of the Fe precipitates. The thin segregation layer will alter surface as well as interface energies of the encapsulated Fe precipitates, which is seen to be a key factor for the transformations of phases in such particles [48, 49]. In a recent study, this issue was rethought. It is deduced that coherency strain reduction in such particles is a major driving force for solute segregation. This elastic energy contribution further scales with the volume of the particles and their specific geometry [50]. Impressively, even core(Fe)-shell(Au) NPs could be successfully fabricated via the dewetting route (Figure 39). Here, the overall Au content was decreased by adjusting the thickness ratio of the bi-layer film to ~80 at.% Fe. Total film thickness determines mean particle size. Annealing was conducted at 1100 °C.

At equilibrium, fcc Au(-rich) and $\gamma$-Fe are the stable phases. However, the high-temperature gamma phase iron (austenite) was not observed during *in-situ* X-ray diffraction in the course of bi-layer dewetting [51]. A more rigorous examination that reflects on the $\alpha \leftrightarrow \gamma$ transformation in Fe and Fe-Au micro- and nanoparticles can be found elsewhere [52].

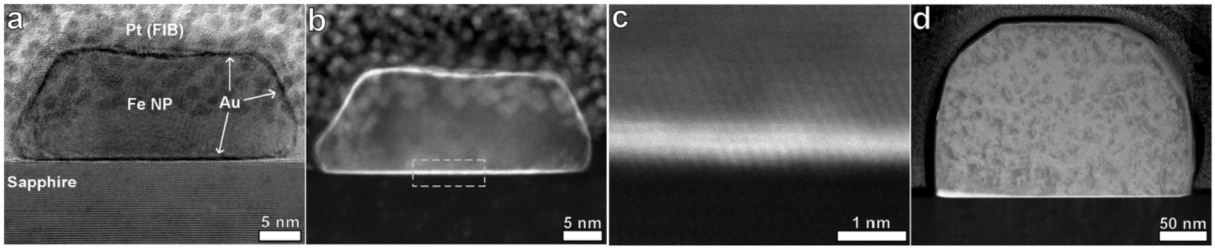


**Figure 39.** Employing surface/interfacial segregation to fabricate *core*(Fe)-*shell*(Au) NPs. (a) Cross-sectional view of a NP obtained via dewetting of a thin (1 nm Au/ 3 nm Fe) bi-layer using high-resolution TEM imaging. The bi-layer thin film was annealed at 1100 °C for 1 h under forming gas flow. (b) and (c) The same view using HAADF-STEM mode which highlights the thin Au segregation layer (~1 nm). (d) STEM micrograph of a larger particle also showing a thin segregation layer to all faces and the interface. Reprinted from Ref. [51].

## 2.8 Templated dewetting

A key factor that influences the dewetting of thin solid films is the substrate – the material type, its crystallinity, and especially the topography. The latter can be used to define precise arrangements of monodisperse NPs via solid-state dewetting (Figure 40). Compared to a *flat* substrate, the dewetting on pre-patterned substrates is more or less confined by the underlying geometric relief. The aim is to control (minimize) size and spacing of the NPs which makes the dewetting method even more reliable for real applications.

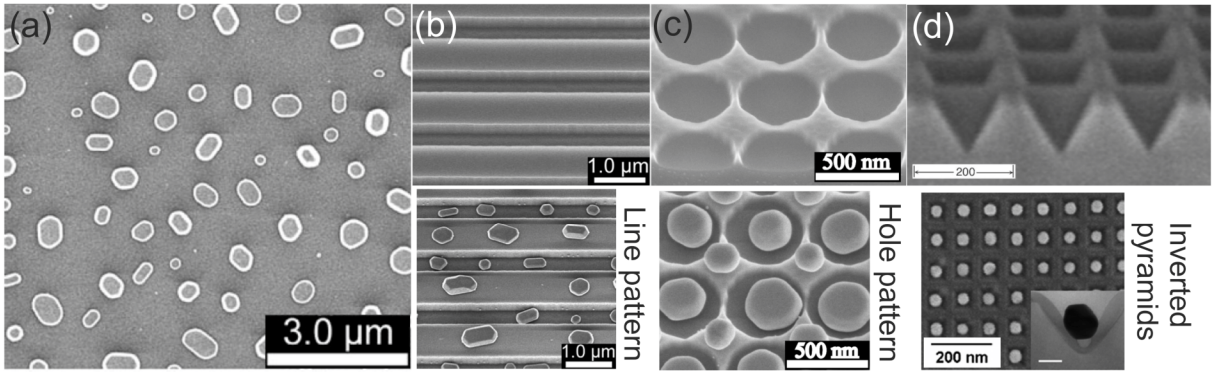


**Figure 40.** Solid-state dewetting on pre-patterned substrates (templated dewetting). SEM images show Au NPs that have arranged via self-assembly on different substrate geometries of $SiO_2$/Si. (a) flat, (b) line pattern [53], (c) circular hole arrays with square symmetry [54], and (d) inverted pyramidal pit arrays. Reprinted from Refs. [55, 56]. The scale bar of the upper image is 200 nm. Please note that periodicity is different from the array containing the particles. Insert: Cross-sectional TEM image of an individual Au particle which is located in one pit.

A variety of lithography techniques are applicable for surface patterning. Also laser-assisted lithography-free techniques are found in literature [57]. At this point, the substrate-conformal imprint lithography (SCIL) is briefly introduced: Established by *Philips Research* and *Suss MicroTec* [58], this nanoimprint technique combines high accuracy with high throughput. The advantage is the flexible stamp which consists of a *rigid* glass carrier and a *soft* polymeric composite (the viscoelastic polydimethylsiloxane, PDMS). This combination ensures the best resolution, large-area (up to 6 inch) patterning, and reliable reproduction at the same time, making it efficient for industrial-scale applications. In this work, the SCIL technique will be used to generate inverted pyramidal pit arrays. Experimental details will be provided in the methodological part of this work.

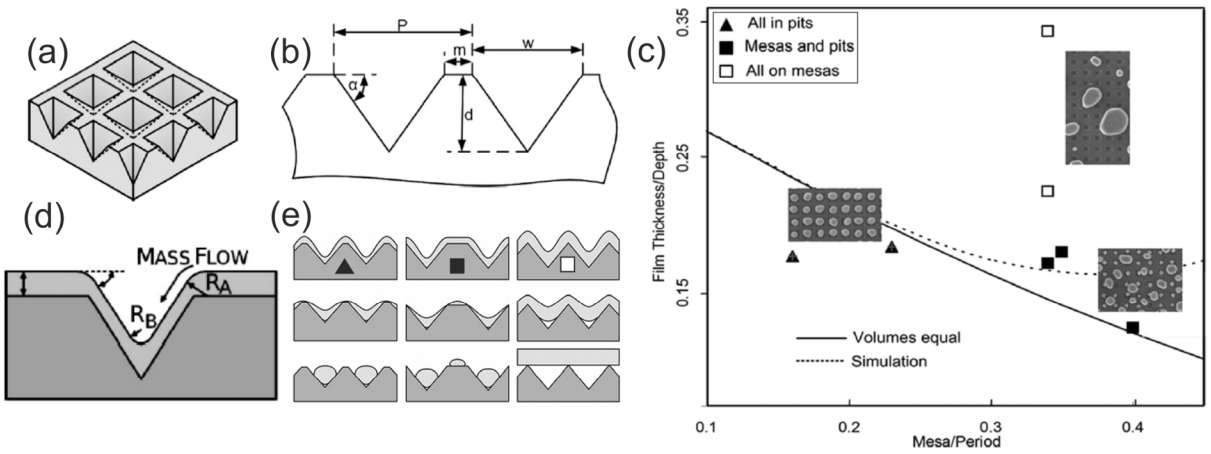


**Figure 41.** Requirements for the dewetting on inverted $SiO_2$/Si pyramidal pit arrays. (a) 3D model, (b) Geometric parameters that define the topography of the substrate: the angle α, which is 54.7° between the (100) surface normal and (111) side walls, the depth *d*, the period *P*, the mesa width *m*, and, optionally, the pit width *w*. (c) Topographic phase map that connects film thickness/*d* with mesa-width-to-period ratio, $R_{mP}$. Three scenarios are shown which are indicated by open/solid symbols. (d) Mass flow is induced by local surface curvature gradient. (e) The same three scenarios illustrated. Reprinted from Refs. [55, 56].

There are a number of studies that reflect on the dewetting of metal thin films deposited onto inverted pyramidal pit arrays [54-56, 59, 60]. Such arrays are determined by their mesa-width-to-period ratio, $R_{mP}$, which is introduced in Figure 41. It is seen that film thickness, depth, and $R_{mP}$ have to be compatible in order to obtain regular arrays of metal NPs each located in one pit. According to Equation (2), three different scenarios can be established: (i) all film material has agglomerated in the pits, (ii) both mesas and pits are covered by particles, and (iii) the film flattens prior to the dewetting (meaning that the film is too thick to be influenced by the substrate geometry). The solid line in Figure 41c simply means that the volume of the film is equal to the one of the pits. This equal-volume condition separates the topographic map into regions where either solely pits contain agglomerated film material or some material remains on the mesas. In its entirety (thick films deposited on smallish holes and vice versa), it is plausible that *templated dewetting* does not work properly as the film does not "sense" the underlying geometry. Please also refer to Figure 29a.

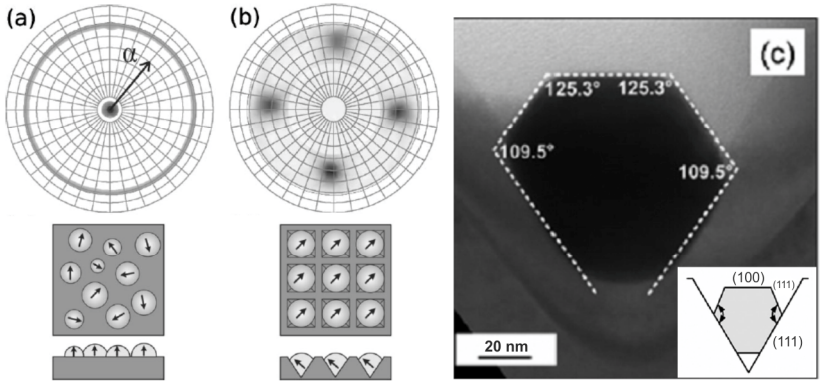


**Figure 42.** Microstructural features of Au NPs generated through thin film dewetting on (a) flat substrate and (b) inverted pyramids. X-ray pole figures show that crystallographic orientation is changed which is illustrated underneath. (c) Cross-sectional TEM view of an individual particle showing faces that have aligned to the (111) side walls. Reprinted from Refs. [55, 56].

Figure 42 compares Au NPs formed via dewetting on flat substrates with the dewetting on inverted pyramids in the case of "all in pits". It is seen that (111) crystallographic texture and the random in-plane orientation of the former film remain for particles upon dewetting on the flat substrate (according to the high intensity ring around 70° in the Au (111) pole figure). For particles formed on the pre-patterned substrate four poles at $\alpha \approx 53°$ can be observed, indicating that crystallographic texture has changed. This angle agrees well with the one between the (111) and (100) planes of the Au fcc crystals (54.7°). Cross-sectional profile of a confined particle reveals that crystallographic faces of the NPs have to align with the walls of the inverted pyramids. Texture therefore changes from (111) to (100). The fourfold symmetry of the pole figure further indicates non-random in-plane orientations. Thermal dewetting on flat substrates clearly differs from that on the same but pre-patterned one. Precise arrays of NPs can be obtained through templated dewetting of metallic thin films.

Only little work has been spent on requirements for alloy or bi-layer thin films deposited on pre-patterned substrates such as inverted pyramidal pit arrays. Two experimental studies that reflect on this issue are introduced: Well-defined arrays of Ag-Au solid solution NPs are formed via dewetting of a bi-layer thin film. Subsequent dealloying removes the Ag, resulting in ordered arrays of porous Au NPs. Please also refer to Figure 37 for details. Average ligament size can be tuned by the Ag content being removed from alloy particles: The more Ag is dissolved in the homogeneous solid solution Ag-Au NPs, the thicker the ligaments are (Figure 43). The Ag content can then be adjusted by the thickness ratio of corresponding bi-layers, which is well-defined after deposition. This study impressively shows how templated dewetting

of bi-layer thin films can be employed to obtain large-area arrangements of tailored nanoparticles.

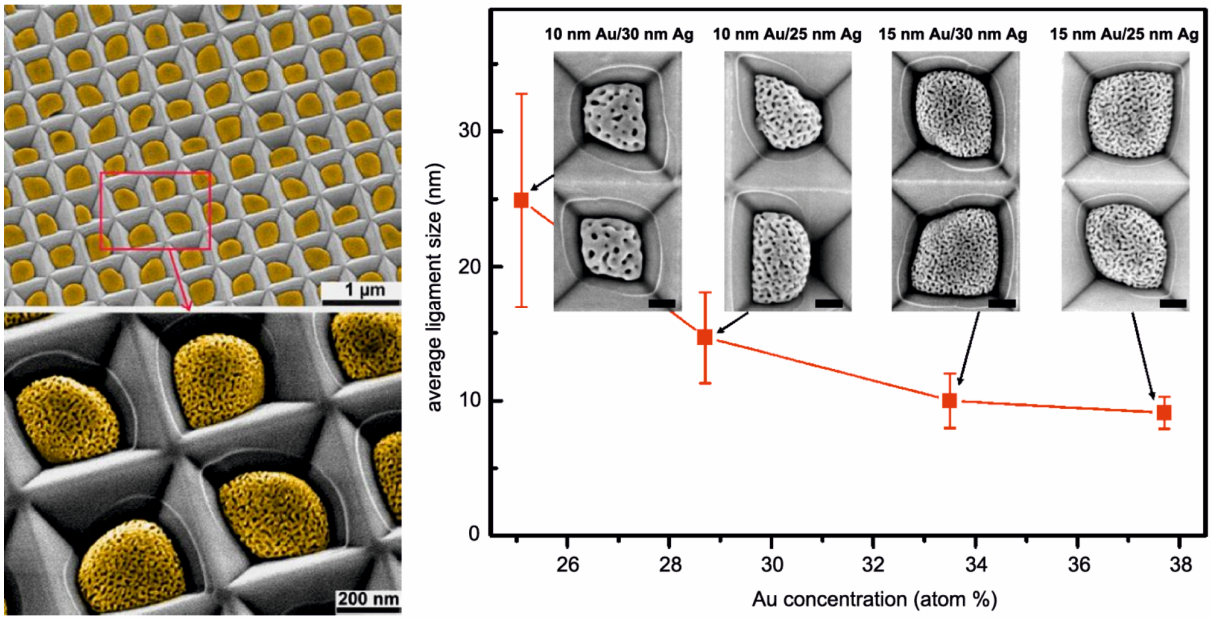


**Figure 43.** Ordered arrays of porous Au nanoparticles obtained by dewetting of Ag-Au bi-layer thin films deposited on inverted pyramidal pits and subsequent dealloying. Contours of former Ag-Au NPs are clearly seen in the SEM images. Average ligament size of porous Au NPs depends on the composition of the former Ag-Au alloy particles [61].

Another study that reflects on magnetic recording applications uses Co-Pt bi-layer thin films to create Co-Pt alloy nanoparticle arrays. Initial bi-layer film thickness was 12 nm. The alloy composition was fixed by adjusting the thickness ratio of individual metal layers (*e.g.*, 4.5 nm Co/7.5 nm Pt for the Co-52at.% Pt NPs). Figure 44 shows two kinds of nanoparticle arrays, corresponding to different alloy compositions. Annealing procedure was the same in either case. The alloy having 36at.% Pt corresponds to the disordered fcc phase in the equilibrium phase diagram. Thus, NPs formed are magnetically soft. In contrast, other particles show stronger coercivity and remanence for both in-plane and out-of-plane directions which can be ascribed to the $L1_0$ phase of the Co-52at.% Pt NPs. The face-centered tetragonal (fct) lattice structure enables the so-called *magnetic easy-axis* (c-axis) to align alongside the surface normal. This is why the out-of-plane coercivity is increased. However, it was found that [001] texture was not as pronounced as compared with Au NPs. The reason could be that the Co-Pt NPs (fct structure) cannot fit into the pits as properly as the fcc Au NPs (please also refer to Figure 42). On the other hand, high-resolution TEM unveils that the high-temperature fcc phase is retained by the surface region of Co-Pt NPs (which could be a direct consequence of the fitting procedure).

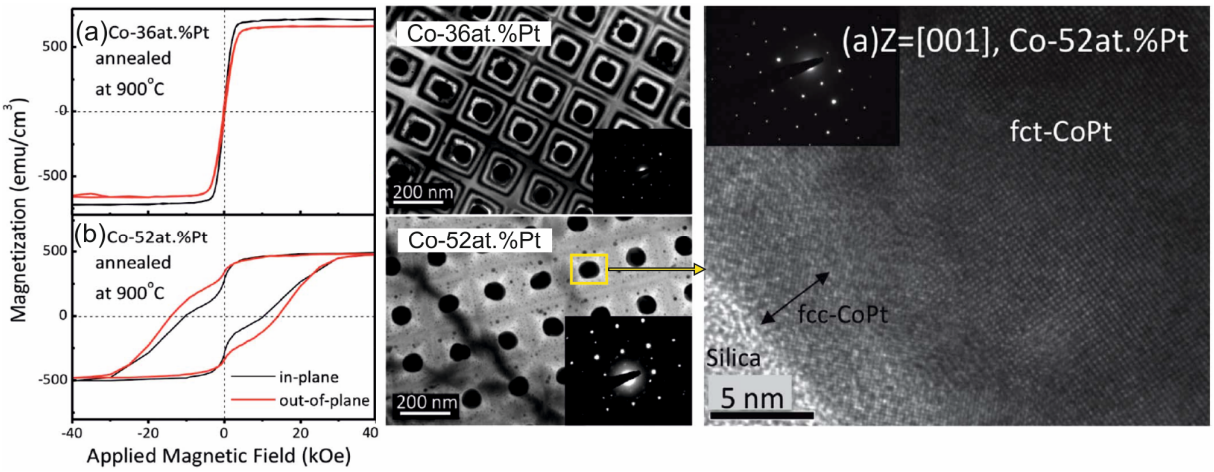


**Figure 44.** Ordered arrays of monodisperse Co-Pt nanoparticles obtained by dewetting of Co-Pt bi-layer thin films at 900 °C for 2 h. Magnetic hysteresis curves were determined using superconducting quantum interference device (SQUID) magnetometry. The effect of alloying is clearly visible in (a) and (b). Plane-view TEM images of corresponding arrays including diffraction pattern are also shown. High-resolution TEM reveals that the surface region of Co-52at.% Pt NPs retains the disordered fcc phase. Reprinted from Ref. [62].

To sum up, this review gives the reader a comprehensive insight into the complex dewetting science. Other approaches also intended to design functional nanostructures using the dewetting method such as pulsed-laser induced dewetting, *PLiD* [57, 63], thin film patterning prior to the dewetting [64, 65], or special patterning techniques [66, 67] would go beyond the scope of this thesis.

# 3 Experiments and methods

*This chapter briefly introduces experimental procedures and techniques applied in the current thesis. Substrate preparation, thin film deposition, thermal processing, and materials characterization are described, i.e., the whole process chain can be followed. Parameters for thin film deposition and thermal treatment are given.*

## 3.1 Substrate preparation

### *3.1.1 Basic cleaning and oxide barrier layer*

(100) oriented, p-type silicon wafers (6–10 Ω cm, *SIEGERT WAFER GmbH* Aachen, Germany) were used as received. These wafers were single-side polished. Prior to deposition of the thin films, it is necessary to create a *diffusion barrier* on the (polished) surface to prevent interdiffusion of Si and layer material and the formation of a low-melting-point liquid eutectic phase (as is the case with **Au-Si**). For this purpose, Si wafers were first treated with Piranha solution (a mixture of sulfuric acid, $H_2SO_4$ + hydrogen peroxide, $H_2O_2$) to remove metal-organic residues from the substrate. After cleaning in deionized water, subsequent treatment with hydrofluoric acid HF removes native oxide. Since oxidation is fastest in its early stages, initial oxide being present before thermal oxidation would be hindering. The as-cleaned wafers were then put in a wet-$H_2O$ ambient to thermally grow a several nm thick silicon dioxide ($SiO_2$) barrier layer.

### *3.1.2 Nanostructuring*

The substrate-conformal imprint lithography (SCIL) technique was used to pre-define the Si surface, which is depicted in Figure 45. The following steps are carried out to obtain well-defined nanoscale inverted pyramids:

(i) The lithography step. Here, the nanoimprint method SCIL is applied (*Suss MicroTec*).

(ii) After UV-curing, the resist (which is the so-called AMONIL®, a special low-viscosity imprint resist) retains the nanoimprint, see Figure 45a.

(iii) Residual resist in the space between has to be removed via inductively-coupled plasma dry etching process (ICP-RIE, *Sentech 500*) in order to expose the underlying $SiO_2$.

(iv) Etch rates of the resist and the exposed $SiO_2$ are different (~ 1 : 2), allowing structure transfer down to the Si substrate via reactive ion etching (RIE, *Oxford Plasmalab 100*), see Figure 45b.

(v) Si selective chemical etching using highly basic aqueous potassium hydroxide KOH finally defines square-based inverted pyramids with {111} side walls via $Si + 4OH^- \rightarrow Si(OH)_4 + 4e^-$ [68]. The Si (100) surface is selectively etched through different etch rates along (100) and (111) crystal planes. This *etch rate selectivity* is influenced by many factors such as defects, impurities, or doping concentration of the Si. During wet-chemical treatment, residual $SiO_2$ acts as a mask, defining the mesa-width-to-period ratio: The longer the etching is carried out, the deeper and sharper is the 2D *saw-tooth* profile, see Figure 45c.

(vi) The last step again includes the growth of thermal oxide on the pre-patterned Si substrate to create the diffusion barrier prior to thin film deposition. After removing $SiO_2$ mask via hydrofluoric acid, a new oxide layer is grown either via inductively-coupled plasma chemical vapor deposition (ICP-CVD, *Oxford Plasmalab 100*) or by means of rapid thermal annealing (RTA, *Jipelec*) in an oxygen ambient, see Figure 45d.

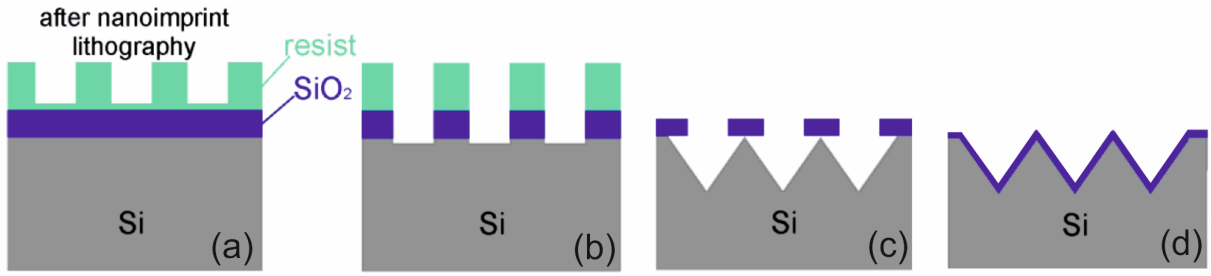


**Figure 45.** 2D schematic of the Si substrate patterning via nanoimprint lithography and selective etching. (a) Initial state after imprint, (b) RIE "down to substrate", (c) KOH selective etching, and (d) thermal oxide barrier layer [61].

### *3.1.3 Cutting and final cleaning*

In order to ensure adequate handling for further processing, as-prepared 4" wafers (flat or pre-patterned) were cut into small square pieces having a side length of 5 or 10 mm. Final cleaning includes treatment with acetone to remove organic residues, using isopropanol to dissolve the acetone, and, finally, cleaning with deionized water (DI).

## 3.2 Thin film deposition and thermal processing

### *3.2.1 Electron beam evaporation*

This method belongs to the physical vapor deposition (PVD) family and is integrated in the PVD cluster system (CS400ES, *von Ardenne*) located in the cleanroom of the Center for Micro- and Nanotechnologies at TU Ilmenau, IMN MacroNano®. Electron beam (or simplified e-beam) evaporation is characterized by high deposition rates at a base pressure of $2\times10^{-7}$ mbar. **Au**, **Ni**, and **W** thin films were deposited onto $SiO_2$/Si substrates with an accuracy of thickness of about ±5%. Assuming that continuous films are formed upon deposition, a polycrystalline microstructure having columnar grains will evolve at room temperature, *i.e.*, without pre-heating the substrate during condensation of target material. This is especially true for comparatively low-melting metals such as Au or Ni according to the zone model established by *Movchan* and *Demchishin* (see Figure 46). The ratio between substrate temperature ($T_S \approx 300$ K) and the melting point of the target ($T_{m,Au} \approx 1337$ K) is $T_S/T_m \approx 0.22$ which is close to the predicted value of about 0.26 for the transition from zone 1 to zone 2.

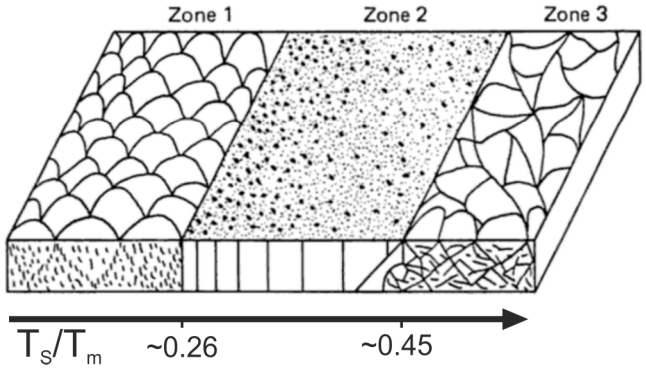


**Figure 46.** Microstructural changes in thin films upon vapor deposition after Movchan and Demchishin. Transition temperatures $T_S/T_m$ are valid for metal thin films. Schematic drawing reprinted from Ref. [69].

### *3.2.2 Rapid thermal annealing*

All the samples in this work were treated by means of a rapid thermal annealing processor (RTA or RTP, *Annealsys*, formerly *Jipelec*). This technique allows one to conduct short heat cycles with defined heating rates which is suitable for the annealing of bi-layer (alloy) thin films. Figure 47 shows a typical annealing history applied to the samples.

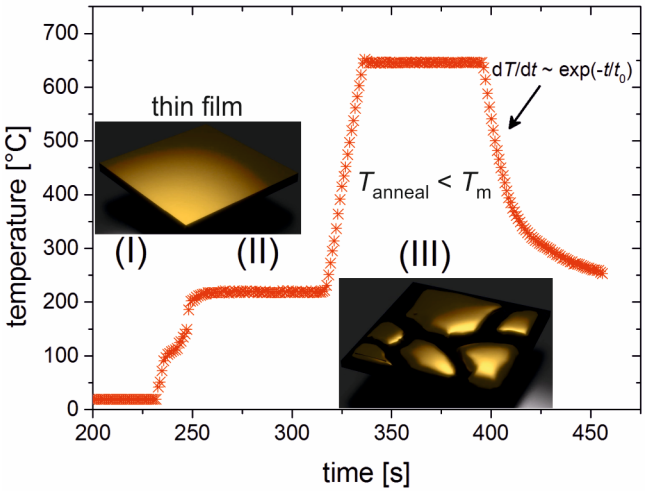


**Figure 47.** Typical temperature profile during rapid thermal processing. Three different regimes can be defined: (I) Pumping/venting ($N_2$ purge), (II) pre-heating at 200 °C, (III) annealing at a given temperature ($T_{anneal}$) followed by cooling in furnace. Please note that time axis does not start at zero here because temperature is only little changed during pumping/venting. Insertions: Computer-animated illustrations showing the onset of the dewetting below the melting point $T_m$ of the film material.

Power-heat coupling with the sample is realized through thermal radiation (and convection). Temperature first reaches a plateau at 200 °C in order to warm-up the halogen lamp array and to introduce desired process gases. Grain growth may also initiate during pre-heating. Halogen lamps are cooled by compressed-air and protected by a quartz window. The window itself is cooled by recirculating cooling water. Then, the effective temperature profile initiating the dewetting runs on. Fastest cooling is achieved by simply switching off the furnace, following an exponential decay. Different process gases such as inert gases (*6N purity* Ar, $N_2$), or reactive gases ($O_2$, $CH_4$) can be used for special applications. Their inlet is controlled by mass flow controller. Also hydrogen is available to create a reducing atmosphere at ambient pressure. **Ar-3.3% $H_2$** forming gas flow was used for all the samples. Gas inlet pipes may contain residual impurities of former processes. It is therefore recommended that one or two idle runs are conducted before actual annealing experiments (*i.e.*, without having the sample inside) to purge the whole system once or twice. Temperature profile is measured by a pyrometer which is usually placed in the middle underneath the susceptor as shown in Figure 48. The sample to be

annealed is then placed onto the susceptor (also called *carrier wafer*) slightly away from the position of the pyrometer.

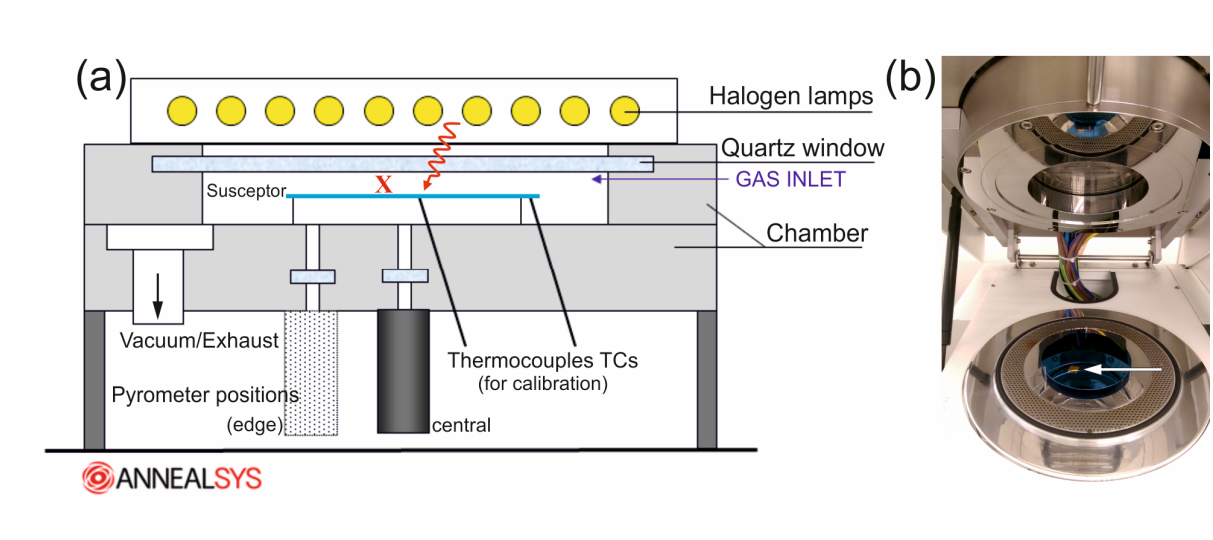


**Figure 48.** RTP. (a) Chamber design by courtesy of Albin Diranzo, Annealsys Company: adequate sample position on the susceptor is marked by a red cross, (b) real view into the opened chamber with $Si_3N_4$/Si susceptor and as-prepared sample lying on it. The position of the sample is marked by an arrow.

Two different susceptor materials are available. $Si_3N_4$ coated Si wafers and graphite absorbers. At medium temperatures, silicon nitride is a reasonable alternative to the much more expensive (but with best absorbing properties) graphite susceptor. The latter is solely used for high-temperature applications well above 1000 °C. Prior to processing, the RTP unit has to be calibrated according to the susceptor material used. In order to summarize experimental parameters for this thesis, the following table list all information about metallic thin films and their thermal treatment conducted.

Table 1. Experimental parameters used in the framework of this thesis.

| Chapter | Thin films investigated | Individual layer thickness | Temperature range | Duration |
|---|---|---|---|---|
| **4** | **Au** | $h_{Au}$ = {1, 2.5, 3, 5, 10} nm | 180 – 950 °C | $t_1$ = 30 sec<br>$t_2$ = 1 min |
| | **W** | $h_W$ = 3 nm | 550 – 950 °C | 1 min |
| | **Au-W** (bi-layer) | $h_{Au}$ = {3, 10} nm,<br>$h_W$ = 3 nm (fixed) | 550 – 950 °C | $t$ = {1, 5} min<br>(1, 6 cumulative) |
| **5** | **Au-Ni** (bi-layer) | $h_{Au, Ni}$ = {5, 10, 15} nm :<br>$h_{tot}$ = 20 nm (fixed) | 500 – 900 °C | 1 min |
| **6** | **Au-Ni** (particles) | $h_{Au, Ni}$ = 10 nm | $T_1$ = 950 °C<br>$T_2$ = 650 °C | $t$ = {1, 5, 10} min<br>(1, 6, 16 cumulative) |

## 3.3 Central analytics tools for materials characterization

### *3.3.1 Electron microscopy and elemental analysis*

In order to trace morphological features during dewetting, scanning electron microscopy (FEG-SEM, *Hitachi S-4800*) is an essential tool. Primary electrons are generated via cold field emission. SEM imaging was performed at **low kV** (usually 2 kV) in order to reduce negative effects due to charging. At such low accelerating voltages, the dimension of the interaction volume *beam–specimen* rapidly decreases. High-resolution imaging (SE I + II) becomes possible at a relatively good signal-to-noise (S/N) ratio and dedicated backscattered imaging approaches the resolution of the SEs. Trajectories of these electrons which are line of sight with the upper detector are shown in Figure 49: Secondary electrons (SEs) and low-angle (L.A.) as well as high-angle (H.A.) backscattered electrons (BSEs, carrying compositional information) are trapped by the detector placed in the vicinity of the objective lens.

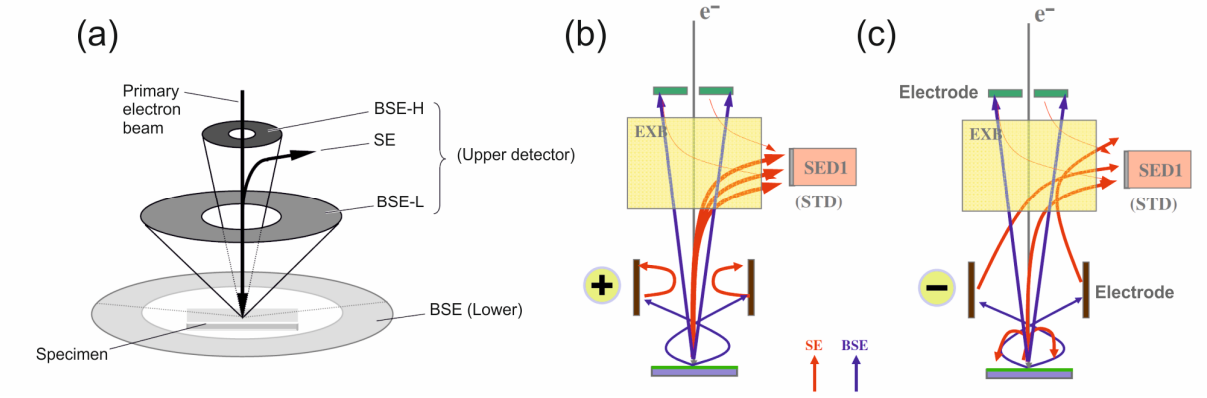


**Figure 49.** SEM imaging. (a) Depending on the solid angle, signals generated from specimen can be detected by an upper ("through the lens") or lower (out-lens) detector, which are usually Everhart-Thornley type ones. Schematic drawing reprinted from Ref. [70] with kind permission of Hitachi High-Technologies Corporation. Upper detector (SED1): (b) SE mode and (c) L.A. BSE mode for low kV BSE detection by means of conversion electrodes (+)/(–) and *ExB* energy filtering. The S/N ratio of the H.A. BSE signal is rather weak as indicated by thin red arrows. Schematic drawings by courtesy of Dipl.-Phys. Dr.-Ing. Roland Schmidt, Hitachi High-Technologies Corporation.

The lower detector signal usually consists of SEs and very low-angle BSEs. Working distance (WD) needs to be adjusted once the detector is changed. In order to be less confined by an accurate specimen height for the use of either the upper or the lower detector, both signals can be mixed. Thus, a suitable signal for probing multicomponent thin film samples was **SE (M, L.A.70)**, *i.e.*, a BSE-rich signal coming from both detectors (with the upper detector signal being the dominant one at shorter WDs). Before imaging, the SEM has to be aligned by the operator in such a way that the primary electron beam is positioned along with the optic axis, the objective aperture is centered, and astigmatism is corrected/minimized.

Additionally, the SEM is equipped with a silicon drift detector (UltraDry SDD with 10 mm² crystal active area, *Thermo Fisher Scientific*) for chemical analysis by means of energy-dispersive X-ray spectroscopy (EDS NORAN™ 7 X-ray Microanalysis System, *Thermo Scientific*). Accelerating voltage for EDS was increased to 7 kV in order to excite **Au M** (Au M$\alpha$, 2.120 keV) and **Ni L** (Ni L$\alpha$, 0.851 keV) series. This voltage can be seen as a compromise between adequate excitation and reduced measurement artifacts at the same time such as drift issues due to charging. In order to further decrease image drift, regions of interest were exposed to the electron beam for a while. The measurement can be started once a thermoelectric equilibrium between sample and electron beam is reached. Elemental analysis was performed mainly in *line scan mode* along thin film structures such as branched voids or even submicron-sized particles. In order to increase statistical significance, line scans were repeated at least three times at a dwell time of 1 s. During EDS, WD is increased to 15 mm to ensure photons being line of sight with the detector, which has to be moved inside the chamber close to the sample. 25 µA objective aperture together with high probe current are used to obtain adequate count rates at a dead time below 30%.

Selected samples were also analyzed by transmission electron microscopy (TEM, *FEI Tecnai 20 S-Twin*) performed at 200 kV. High-resolution imaging as well as selected area electron diffraction (SAED) were carried out in order to clarify microstructural issues. Chemical analysis was performed in scanning transmission mode (STEM-EDS).

### *3.3.2 X-ray diffraction (XRD)*

This powerful analytical tool was used for structural clarification. During thin film dewetting, grain growth, texture evolution, and (in case of multicomponent thin films) phase formation take place. All these structural properties are traceable by means of X-ray diffraction. A *Siemens D-5000* (now *Bruker AXS* Advanced X-ray Solutions) diffractometer was used in ***θ–θ* geometry**, *i.e.*, a fixed sample with moving source and detector at angular velocity $\omega$ (Figure 50a). The sample itself can be rotated in order to either raise the overall peak intensity during measurement or minimize substrate contribution by means of a $\varphi$ scan (here: the Si (400) peak of the underlying Si substrate).

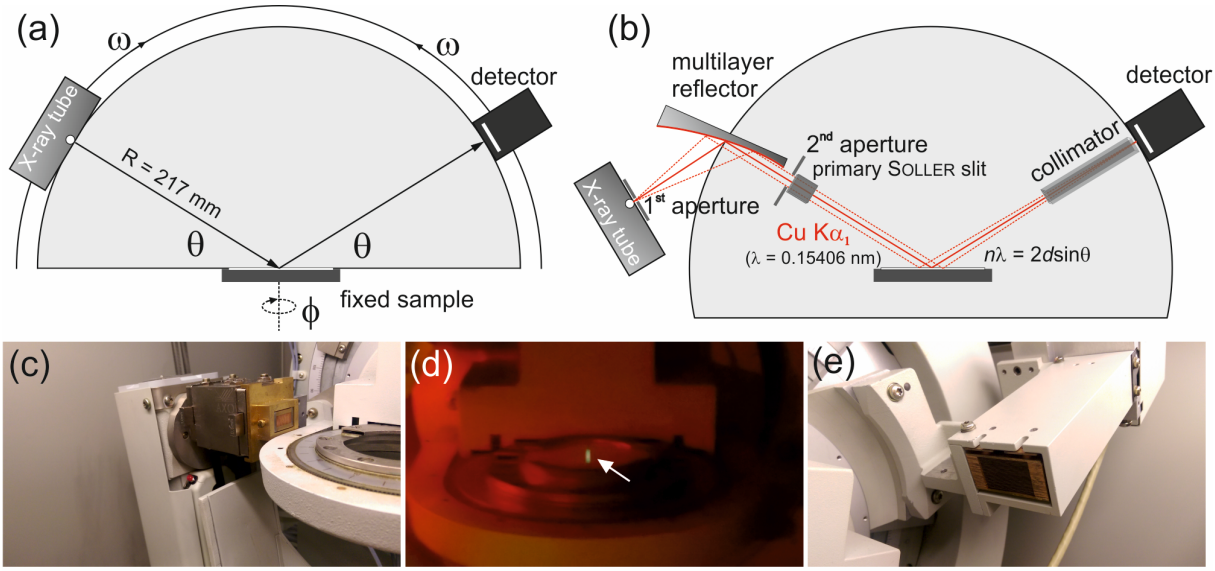


**Figure 50.** BRAGG-BRENTANO X-ray diffraction in (a) $\theta$–$\theta$ geometry at a (b) parallel beam optic as is the case with the goniometer used in this work. Photographs of the inside of the Siemens D-5000 by courtesy of Dr.-Ing. Rolf Grieseler, TU Ilmenau: (c) primary side showing the X-ray tube together with the divergence slit, a thin film attachment (the multilayer reflector, also known as GOEBEL mirror), a near sample aperture, and primary SOLLER slit, (d) fluorescent line focus at sample position, marked by an arrow, (e) secondary side showing the collimator in front of the detector.

A **parallel beam optic** is used for adequate illumination even at small angles $\theta$, forming a lathy line focus at the position of the sample to be measured (Figure 50b – e). Cu is used as the anode material in the X-ray tube. Characteristic Cu K$\alpha$ radiation is selected for illumination. Due to different absorption capacities of individual layers of the multilayer reflector, the divergent, polychromatic incident beam is transformed into a *monochromatic*, parallel beam upon reflection. Ni/C multilayers are predominantly used as layer materials for monochromatization of Cu radiation [71]. Beam optic parameters as well as custom settings are summarized in Table 2. Sample size should be at least 1 cm² in order to ensure adequate illumination during measurement. X-ray diffractograms were compared with the powder diffraction file database (PDF) of the **I**nternational **C**entre for **D**iffraction **D**ata (ICDD, Newtown Square PA, 2010) to identify phases formed during solid-state dewetting of the multicomponent bi-layer thin films. Information about texture evolution is also evident from diffraction data.

Table 2. Summary of key parameters for X-ray diffraction in this work.

| Feature | Parameter | Absolute value |
|---|---|---|
| Fixed beam optics | Divergence slit (1st aperture) | 1.000 mm |
| | Near sample aperture (2nd aperture) | 0.600 mm |
| | Thin film attachment | 0.460 ° |
| Settings | X-ray tube mode of operation | 40 kV/40 mA |
| | Delay time | 10 s |
| | 2-theta range | 15…100 ° |
| | Step size | 0.020 ° |
| | Time/step | 2 s |
| | Scan type | Locked coupled |
| | Scan mode | Continuous Scan |
| | Spinner ($\varphi$) | Off |

### *3.3.3 Nanomaterials preparation using focused ion beam (FIB)*

An essential tool for the preparation and analysis of materials at the nanoscale is the focused ion beam (FIB). An *Auriga 60 CrossBeam* workstation containing a $Ga^+$ ion source for FIB as well as a FEG-SEM GEMINI® column from *Zeiss* was used. This combination allows high-precision *in-situ* preparation of nanomaterials. Their arrangement within the vacuum chamber is shown in Figure 51. Vacuum level during preparation is usually $10^{-6}$ mbar.

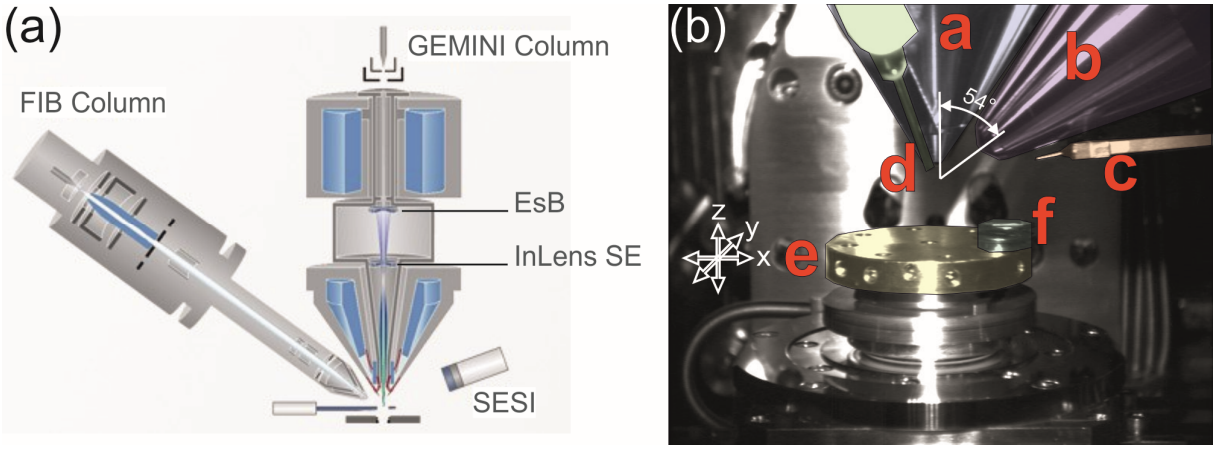


**Figure 51.** (a) CrossBeam arrangement together with detector positions. Cross-sectional illustration with kind permission of Carl Zeiss Microscopy GmbH. (b) Chamber interior of the Auriga 60 CrossBeam workstation: a. electron gun, b. FIB, c. GIS, d. micromanipulator at the front side, and e. the stage with f. mounted sample.

The stage can be moved in *x*, *y*, and *z* direction to position the sample for *in-situ* FIB milling. At each position, full rotation is possible. The so-called *m-axis* is further used to set the *eucentric height*. Due to plenty of components inside the chamber, stage motion has to be

carried out carefully. The gas injection system (GIS) can be used to deposit Pt, C, as well as W. These precursors usually act as protection layers prior to FIB processing. For example, the combination of Pt/C bi- or multilayers can help increase analytical ability of materials interfaces. Another use of the precursor materials is filling or joining structures at the nanoscale. For imaging, different detectors are available: An in-lens SE one, an out-lens secondary electrons secondary ions (SESI) detector, and an energy selective backscattered (EsB) detector suitable for compositional contrast can be used (see also Figure 51 – for details, the author refers to respective Internet presence by *Zeiss*). Another important tool is the *Kleindiek* MM3A-EM micromanipulator. Two of them are available for a variety of applications. Here, manipulators are mainly used as transfer tools. The following list briefly summarizes FIB techniques especially used in the framework of this thesis:

- *Preparation of cross-sections*

  In order to get an idea of a particle interior, FIB cross-sections are prepared. Prior to that, regions of interest (ROI) have to be covered by a Pt and/or C protection layer by means of the GIS. The colored area represents the region where particles are affected by precursor deposition (which is the former sample grid, see Figure 52a). Different milling steps are successively carried out to approach particles (or arbitrary structures of interest). During milling, also re-deposition of removed material takes place, in particular on the side walls of the trapeze-shaped depression. Finally, the area under consideration is polished via focused ion beam at 30 kV and 240 pA.

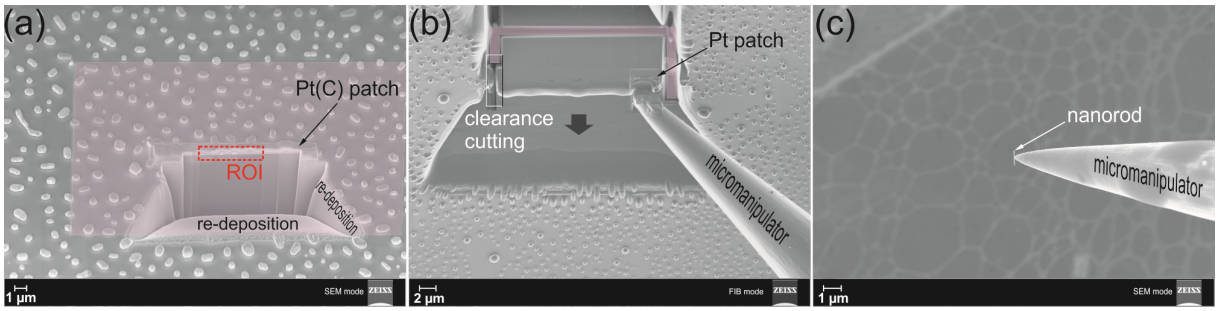


**Figure 52.** Nanomaterials preparation techniques using the focused ion beam. (a) cross-section, (b) lift-off process of a TEM lamella, (c) nanostructure transfer onto a TEM grid.

- *Preparation of TEM lamellae*

  Figure 52b shows the *lift-off* process using a micromanipulator. Prior to that, the lamella is cut into shape (so-called U profile, see colored areas). Once the lamella has been attached to a Cu grid, further thinning is carried out to make it translucent

for the electron beam in a TEM (irradiated area: a few microns, thickness: several nm).

- *FIB Nanomanipulation*

  This technique is used to cleanly transfer and precisely position nano-objects (particles, pillars, rods, wires,…) *without* any precursor. At such dimensions, nanostructures simply "stick" to manipulators through adhesion forces, see Figure 52c. This is especially needed for composite materials in order to avoid any undesired effects such as contamination. For this purpose, it is recommended to use both manipulators (detachment from substrate, transfer, and final positioning).

# 4 On the role of W in the dewetting nature of Au

*Au and W single- and bi-layer thin films provide an interesting situation: The melting point of W (3422 °C) is considerably higher than that of Au (1064 °C) and different cubic crystal systems are present for W (body-centered cubic, bcc) and Au (face-centered cubic, fcc). Consequently, from thermodynamics, this binary system is completely immiscible in solid state. Individual layers as well as bi-layers are studied and compared in this chapter. For the bi-layer configurations considered, the role of stacking sequence at medium temperature will be highlighted. For W being the ground layer, the substrate effect which depends on initial Au film thickness is shown. W being on top is shown to hinder the dewetting of Au due to passivation. Influencing parameters associated with solid-state dewetting (SSD), such as activation energies for void initiation/void growth, diffusion paths being active, or ambient conditions are discussed with respect to changes in film morphology. Furthermore, it is demonstrated that the combination of Au and W thin film evolution can be used to make regular arrays of nanoparticles (NPs).*

## 4.1 Formation of Au NPs through dewetting revisited

Initially, a brief review on the influence of Au film thickness on morphology evolution will be given. Figure 53 illustrates that, depending on Au film thickness, the as-deposited state significantly affects mean size, areal density and morphology of the Au NPs formed. For 3 nm Au, a discontinuous film of isolated Au islands is grown; lateral grain growth or -evolution in such multi-grained island structures is limited. This implicates that initial steps for the dewetting in solid state (*i.e.*, void formation and -evolution) are skipped when transforming the polycrystalline islands into single- or bi-crystal particles. This is of course quite contrary to continuous films where film voids and grain boundaries are found to interact [24, 28]. Consequently, uniform spherical Au NPs are formed rather fast via surface (and/or interface) diffusion upon annealing at elevated temperature. Surface melting may also contribute here due to reduced scale. Particle mean diameter coincides with the one of the former Au islands, indicating that common void evolution and associated reallocation of film material did not occur. However, long-term annealing may cause the mean particle size to increase due to ripening of densely populated particles. Such a phenomenon is indeed reported for ultrathin Au films annealed at 900 °C for 60 min [72].

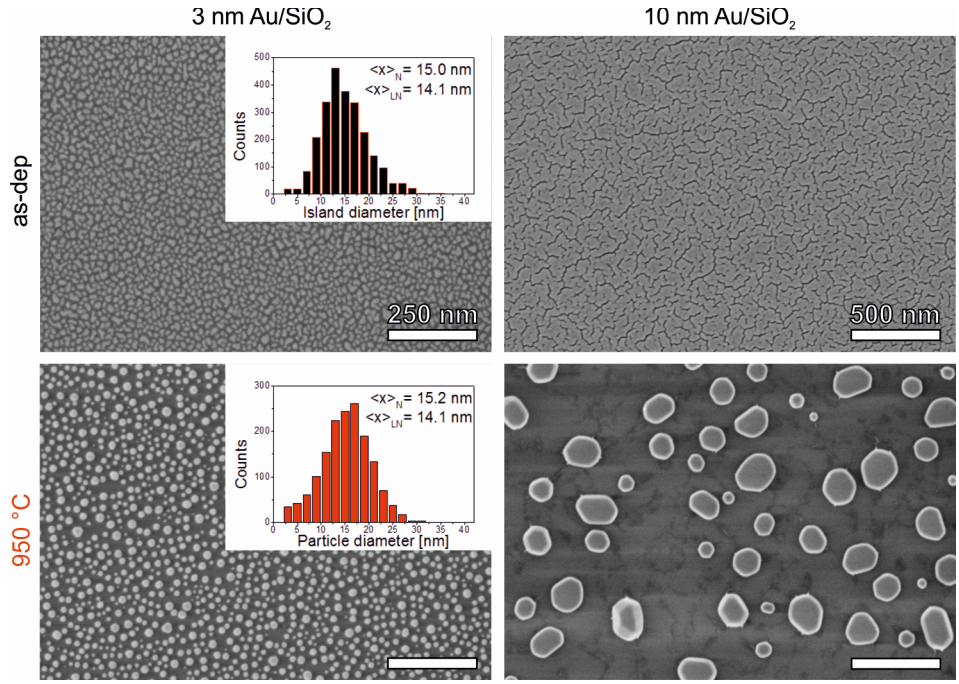


**Figure 53.** NP formation via SSD of Au thin films deposited on $SiO_2$. Both samples were annealed for 1 min at 950 °C. Statistical analyses on mean feature size using normal ($<x>_N$) or lognormal ($<x>_{LN}$) probability density function (PDF) are shown for 3 nm Au for the purpose of comparison. It is seen that NP characteristics are determined by the as-deposited state ("as-dep"). Scale bars are valid down the column. Feature sizes were calculated using the analyze particles tool of the free software ImageJ [73].

For 10 nm Au, the as-deposited state is a continuous layer with *grooves* running through it (Figure 53). These grooves are probably caused by some residual stresses inside the film after deposition. Anyway, this morphology causes the dewetting to turn into a different mode. The majority of the particles formed by dewetting are rather flat showing faceted edges. This metastable shape even holds for long-term annealing (in case of not containing grain boundaries) [31]. Moreover, the (lateral) particle size is considerably higher than in case of the 3 nm Au film. A clear view of particle size evolution as a function of Au film thickness during SSD on $SiO_2$ is given elsewhere [54]. The main message here is the fact that Au film evolution (and final particle formation) is predefined by its initial state after deposition, especially for ultrathin Au films with a layer thickness well below 10 nm. An immediate consequence is observed for the plasmonic nature of the Au nanostructures considered. Figure 54 exemplarily shows UV-Vis spectra of ultrathin Au films: A clear blue-shift of the localized surface plasmon resonance (LSPR) peak is observed for temperatures above 320 °C which occurs due to the dewetting of isolated islands into spherical NPs already at low temperatures. This *shape effect* becomes more evident at increasing initial film thickness. Here, the aspect ratio of the island network also increases until structures interconnect. This trend becomes visible in Figure 54.

The transformation of high-aspect ratio nano-islands into nano-spheres then results in a larger peak shift. A more rigorous examination concerning this can be found elsewhere [6].

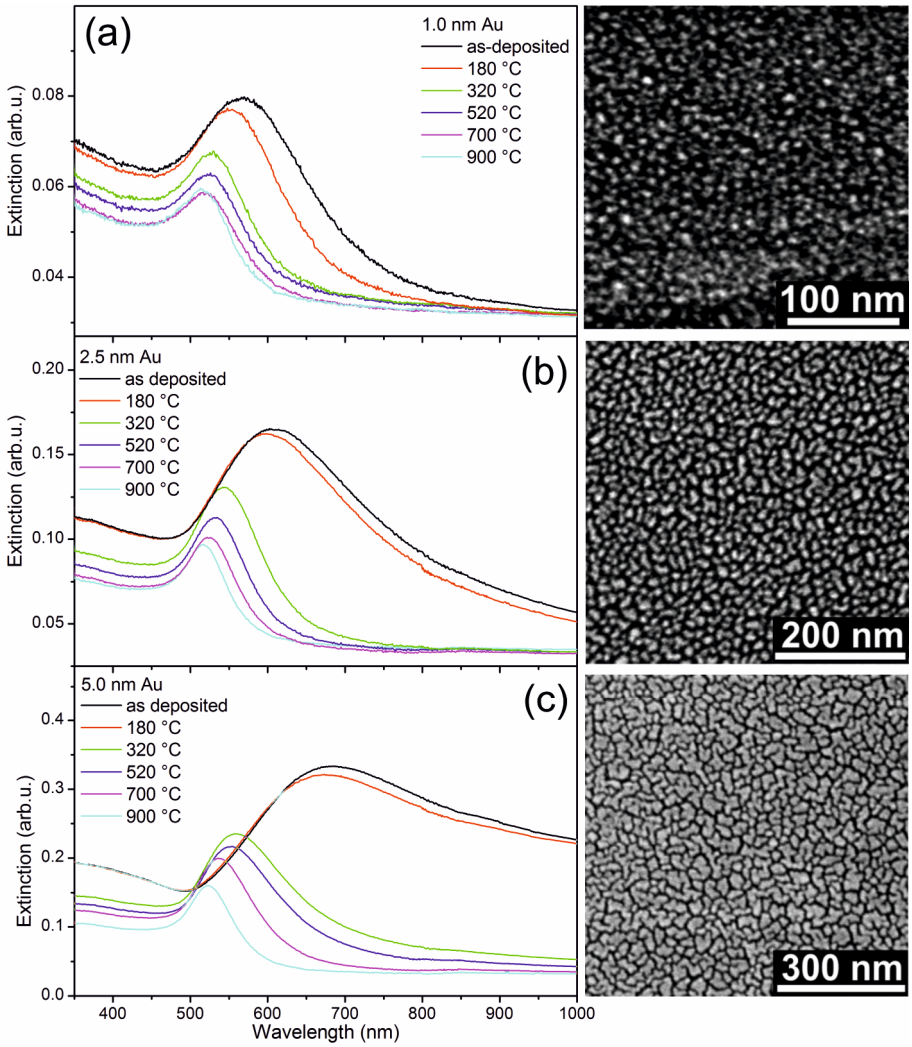


**Figure 54.** Extinction spectra of ultrathin Au films deposited on fused silica as a function of film thickness. Temperature dependence of the localized surface plasmon resonance peak can be related to the transformation of isolated Au islands in the as-deposited state into spherical NPs upon dewetting. This wavelength shift increases with increasing initial film thickness. Short-term annealing (30 sec) was conducted for all thermal treatments (a – c). Additionally, SEM micrographs of corresponding as-deposited states are also provided to the right of each spectrum. Optical measurements were performed using a UV-Vis spectrometer in transmission mode (*Agilent Cary 5000 UV-Vis-NIR*).

## 4.2 Morphology evolution of W ultrathin films

W films are barely investigated with respect to SSD. To the best of the author's knowledge, the only report on W dewetting or self-assembly available in literature was found in *Liu et al.* [74]. Here it is stated that needle-like W nanocrystals form at temperatures below 1000 °C upon annealing for 2 min in an inert ambient out of ultrathin W films deposited on $SiO_2$. At higher temperatures, this anisotropic effect, *i.e.*, different growth rates along different crystal orientations vanishes due to an increased mobility of surface mobile atoms. However, any systematic study on this effect and the combination with the dewetting of another metal is missing. In order to initially verify W nanocrystal formation solely via thin film dewetting, careful TEM investigations were carried out (Figure 55). FIB Nanomanipulation is used to cleanly transfer nanocrystals onto a TEM grid. For adequate observation, these objects were put on a 300 mesh Cu grid with a two-layer graphene film on a lacey carbon film, provided by *Plano GmbH*, Wetzlar, Germany.

The agglomeration starts from a continuous and closed W layer. Here, a grainy surface is visible from image contrast in the SEM micrograph. Even small seed-like structures can be identified, possibly acting as starting points for the self-assembly: Generally speaking, dewetting means that film material agglomerates in such a way that the film gradually exposes the underlying substrate via evolution of crystal voids. However, upon annealing, ultrathin W films show indeed a kind of nanocrystal growth instead. At 550 °C, small nanorods (NRs) start growing from the top of the film *without* building voids (Figure 55a). Their spatial arrangement seems to be random. At increasing temperature, some remaining film material is also transformed into NPs and the aspect ratio of the ultrafine needles becomes extensively higher, indicating anisotropic crystal growth along a preferred crystal axis.

Figure 55b exemplarily shows the transport of an individual NR from the original $SiO_2$ substrate onto a TEM grid. It can be confirmed that such a single crystalline NR reveals a preferred growth direction which is shown in Figure 55c. However, lattice spacing does not match any crystallographic plane of the bcc W. It rather coincides with the spacing of $(0\ 2\ 0)_m$ of the monoclinic *tungsten (VI) oxide* ($WO_3$), which is a low-symmetry system [75]. Reduced crystal symmetry of $WO_3$ may facilitate spontaneous, anisotropic growth: In the monoclinic system, one of the axes is superior in such a way that it is perpendicular to the other two axes, allowing crystal growth along a preferential direction. Oxide formation is also evident from STEM-EDS where a substantial amount of oxygen can be seen (compared to the signal coming

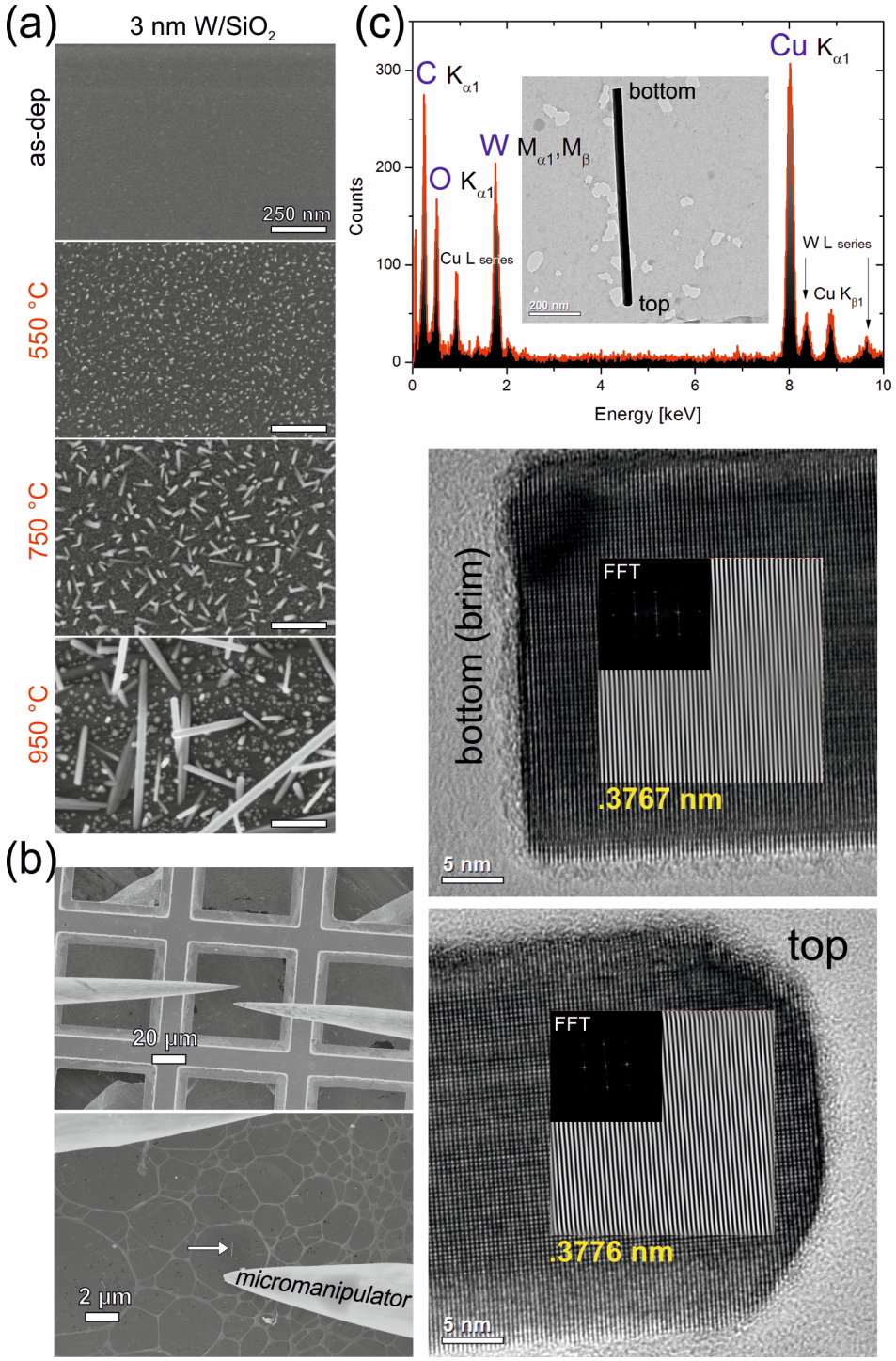


**Figure 55.** Morphology evolution of W ultrathin films. (a) NRs are formed upon isochronal (1 min) annealing at elevated temperatures. Scale bar is valid down the column. (b) A single NR from the sample annealed at 950 °C is placed onto a TEM grid. Its position is marked by an arrow. In the present case, the aspect ratio of the needle-like nanocrystal is approx. 22 (length ~860 nm, width ~40 nm). (c) STEM-EDS analysis shows that there is a considerably high amount of oxygen present at the region of interest (see inset). High-resolution micrographs of the bottom (brim) and the top reveal that the NR is surrounded by a thin amorphous layer covering the faceted surface. Growth direction of the single crystalline NR is highlighted by Fourier filtering and corresponds to a lattice spacing of about .377 nm. This value agrees well with the $(0\ 2\ 0)_m$ spacing of *tungsten (VI) oxide* ($WO_3$).

from W). This agglomeration mechanism is contrary to the assumption to be a dewetting mode (as stated in [74]). In fact, thinking of the considerably high melting point of W, it can be related to an anisotropic oxide crystal growth from small seeds out of the W film in the presence of any residual oxygen. Oxidation may result from impurities during deposition and/or annealing and, moreover, from pre-existing adsorbate states of the pure W surface as samples were exposed to air between both processes [76]. A more rigorous investigation on the origin of oxygen is presented in Figure 56.

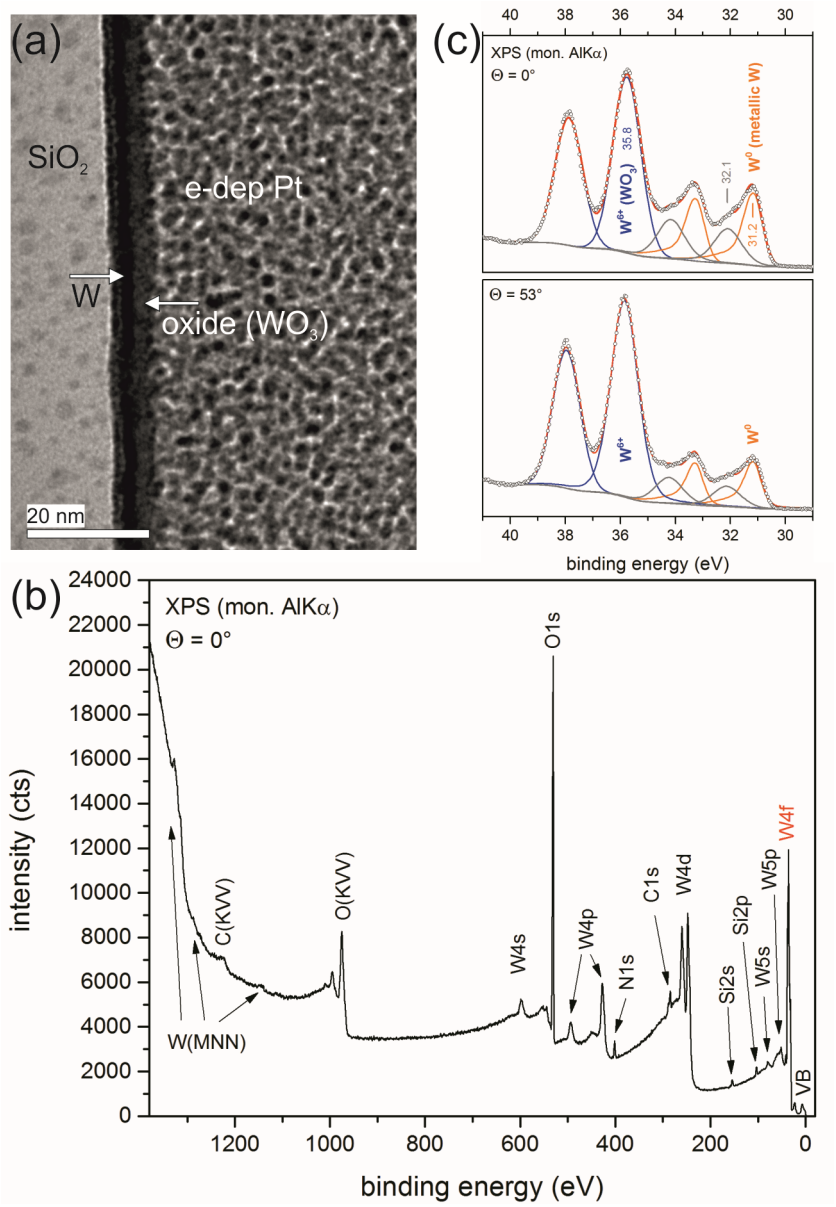


**Figure 56.** Investigation of W as-deposited onto $SiO_2$. (a) TEM cross-sectional view: From image contrast, a layer-like character of the thin film is apparent. Nominal W film thickness (~3 nm) is increased only due to pre-oxidation in ambient air prior to annealing treatment. (b – c) XPS survey spectrum with detailed analysis of the W4f state at different angular emission characteristics (*XPS-SAGE HR 150 Specs*). It is seen that *tungsten (VI) oxide* ($WO_3$) is already existent in the as-deposited thin film.

TEM cross-sectional view reveals, on the one hand, a kind of double layer being present in the as-deposited W ultrathin film. On the other hand, actual film thickness is much larger than 3 nm nominal one. From image contrast, one can conclude that the W film (W atomic number: 74, dark in contrast) is covered by some additional material which gives rise to oxide formation during air exposure of the sample. X-ray photoelectron spectroscopy (XPS) indicates that, depending on angular photoemission, the oxide component is located at the surface region, in accordance with TEM observation. Metallic ($W^0$) as well as oxidation states ($W^{6+}$, *tungsten (VI) oxide*) validate the layer-like character, see the detailed view in Figure 56c. Assuming a 3-zone model ($WO_3/W/SiO_2$) of the sample, an estimate of the oxide thickness can be given using the relative area of dedicated peaks. About 3.4 nm thick $WO_3$ is deduced from XPS profile, which is in good agreement with TEM cross-sectional view ($WO_3$ mean atomic number: 24.5, brighter in contrast).

## 4.3 Morphology evolution of Au-W bi-layer thin films

Stacking sequence as well as individual Au film thickness are combined, *i.e.*, four different scenarios are considered when putting the evolution of Au and W thin films together. Furthermore, morphology evolution at high temperature will reveal a certain interaction between Au NP formation and oxide nanocrystal growth of pre-oxidized W thin films.

### *4.3.1 Medium temperature annealing – Au dewetting modified*

In Figure 57 and Figure 58, all Au as well as Au-W thin film arrangements are illustrated for comparison. Both figures clearly show the effect of stacking sequence at different individual Au film thickness.

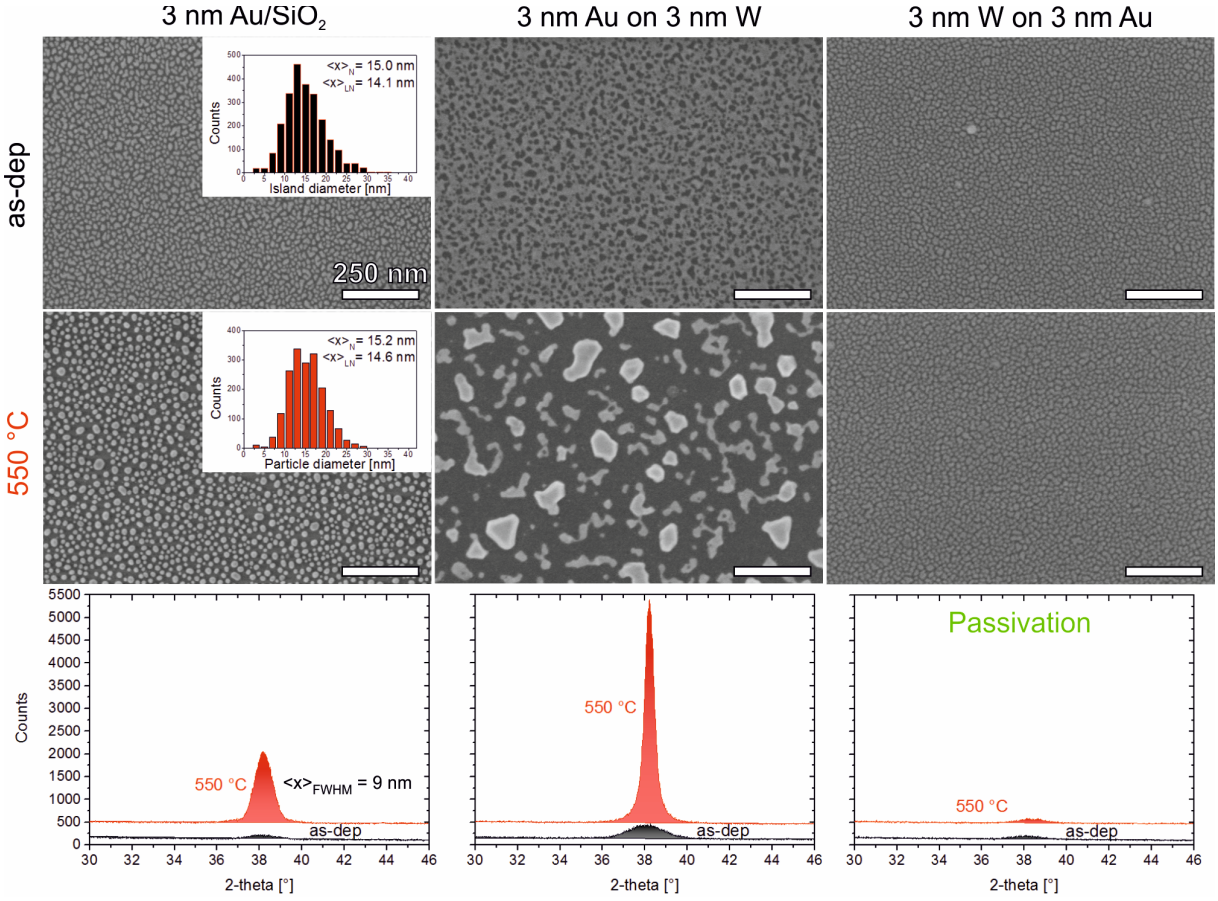


**Figure 57.** Morphology evolution of Au-W bi-layer thin films annealed at medium temperature for 1 min. Equal individual layer thickness as a function of stacking sequence. Scale bar is valid for all images. XRD peak intensity of Au (111) BRAGG reflection can be used as a measure of the degree of coverage (due to constant Au film thickness): The higher the intensity, the more substrate area has been exposed. Intensities (counts) are valid serially.

For a 3 nm Au thin film deposited on $SiO_2$ it is seen that particle characteristics are already established upon annealing at medium temperature: Spherical NPs which are similar in size and

shape like the ones formed at 950 °C are found (Figure 53). However, Au-W bi-layer thin films evolve in a different manner. On the one hand, W is found to modify the wettability of the Au top layer: The as-deposited state is characterized by a mesh-like arrangement of pre-existing critical Au film voids (and no longer isolated film islands). At 550 °C, these voids are able to grow/coalesce very easily, forming complex, particle-like structures while W acts as the substrate. On the other hand, for a reversed bi-layer arrangement, W is found to suppress the dewetting of the underlying Au film because its morphology is still in the initial state at 550 °C. From XRD, it is obvious that the dewetting is pending due to the passivation effect of the ultrathin W top layer. Peak evolution does not occur. As Au and W are immiscible in solid state, phase formation will not affect the evolution of Au (111) BRAGG reflections (and the dewetting). It is rather expected that oxidation plays a major role in the dewetting. In particular, dewetting morphologies of Au on W are notably similar to that observed for other non-wetting ceramic substrates such as $TiO_2$ [77].

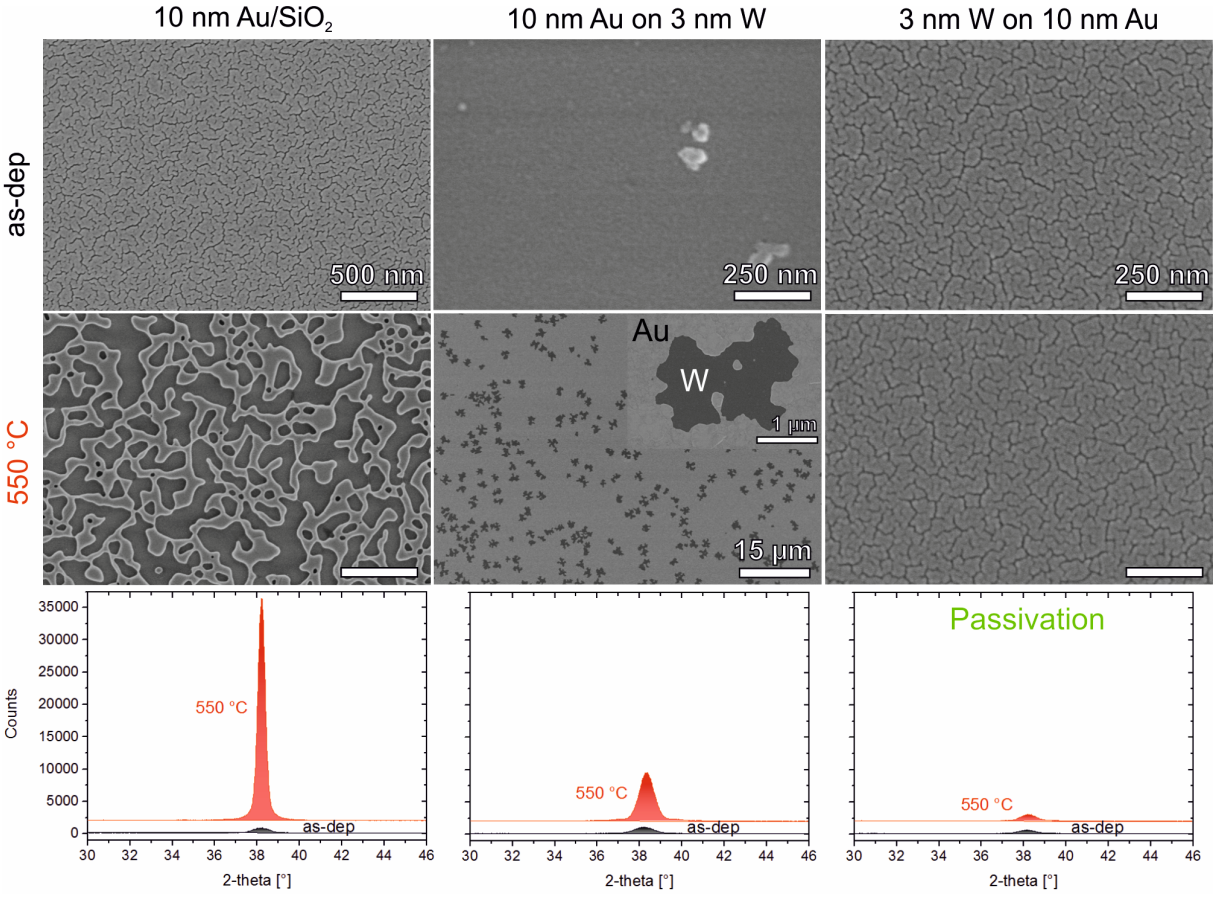


**Figure 58.** Morphology evolution of Au-W bi-layer thin films annealed at medium temperature for 1 min. Different individual layer thickness as a function of stacking sequence. Scale bars are valid down the column. Intensities (counts) are valid serially. The inset (middle column) shows a branched Au film void exposing the underlying W film which acts as a non-wetting substrate.

Similar behavior is found for different individual layer thickness. The dewetting of a 10 nm Au thin film deposited on $SiO_2$ is determined by the groove pattern being present in the as-deposited state. At 550 °C, pre-existing grooves seem to widen, turning the thin film into a labyrinth of exposed substrate regions. However, some critical voids may also form in the film itself. Using $W/SiO_2$ as the substrate makes a different situation: A grainy surface structure is seen instead of grooves or any disclosed area. Upon annealing, branched void growth is found to occur due to increased activation energies for void initiation and growth (as is usually the case with continuous, polycrystalline Au thin films). W being the top layer again suppresses the dewetting of Au due to the effect of passivation. A thin native oxide layer that again passivates the pure W surface will also enhance overall thin film stability. To sum up, SSD of Au thin films at medium temperatures can be critically modified by changing individual layer thickness and stacking sequence of Au-W bi-layer thin films (without exploiting effects due to alloying).

### *4.3.2 High temperature annealing – regular pattern formation*

From all the bi-layer configurations considered in this work, the most interesting one is presented in Figure 59. As a rule of thumb, NP formation via dewetting depends on Au film thickness: The thinner the film, the smaller the particles. Upon annealing, this process will be delayed if W is deposited onto $Au/SiO_2$ since it is acting as a passivation layer at medium temperatures. Due to the immiscibility of Au and W even at high temperatures, effects of alloying can be neglected (which is contrary to studies such as on Au-Co bi-layer films [78]). Therefore, both W and Au layers will evolve independently. The following phenomenological model describes how regular pattern formation of Au-$WO_3$ NPs is realized through self-assembly of a 3 nm W/3 nm Au bi-layer thin film.

**(i)** At medium temperature (750 °C), oxide nanocrystal growth out of the W thin film is initiated prior to the agglomeration of Au islands which are still passivated (Figure 59a).

**(ii)** Upon annealing at 950 °C, agglomeration of Au islands occurs and the growth of the $WO_3$ NRs is more obvious (the aspect-ratio of oxide nanocrystals is increased), as seen in the mixed morphology comprising nanoparticles (NPs) and nanorods (NRs). Moreover, some former $WO_3$ NRs (that undergo Rayleigh-like instabilities) are about to decompose into rows of NPs while Au islands transform into densely populated NPs (Figure 59b). It can be seen that the majority of the particles consists of two or more parts (*Janus-type* particles).

**(iii)** Upon further annealing at 950 °C, $WO_3$ NRs are decomposed into rows of NPs in large scale, and regular arrays of *Janus-type* Au-$WO_3$ NPs are formed (Figure 59c). Compositional contrast indicates that particles consist of Au and $WO_3$ phases which arrange in different particle shapes (Figure 59d). A two-level morphology (regular arrays of bigger particles together with smaller particles in between) is formed via self-assembly of a W/Au bi-layer thin film without *any* chemical agents.

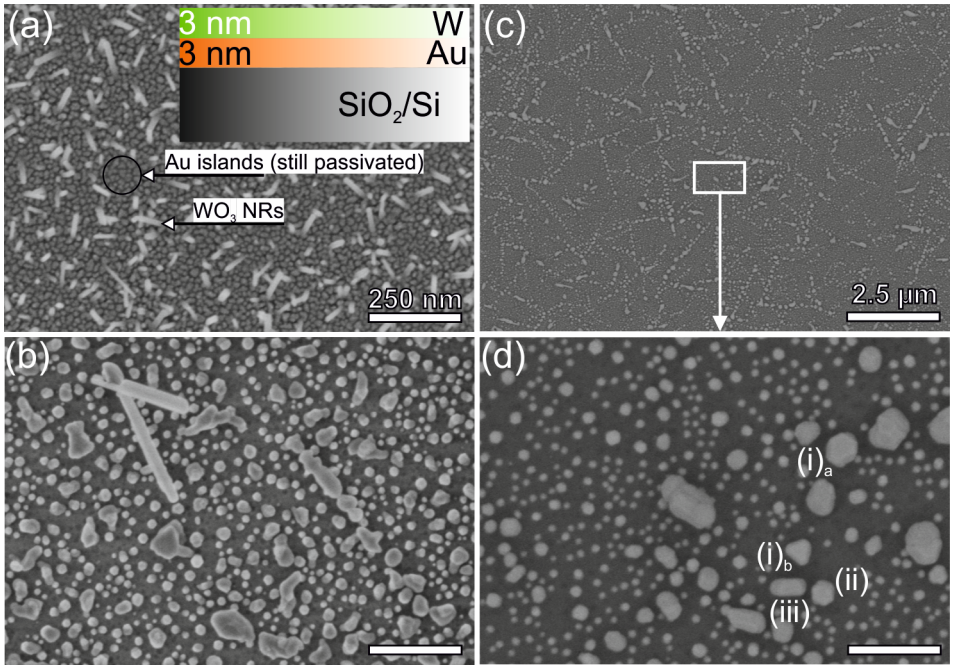


**Figure 59.** Regular pattern formation of Au-$WO_3$ NPs. (a) A 3 nm W/3 nm Au bi-layer represents the starting point as illustrated. At 750 °C, oxide nanocrystal growth is initiated. (b) Upon annealing at 950 °C for 1 min, the bi-layer transforms into nanoparticles (NPs) and nanorods (NRs), which are found to disintegrate. (c) Accumulated annealing at 950 °C for another 5 min then results in the formation of regular arrays of NPs. (d) Magnified view. Different kinds of particle shapes are observed alongside an individual row: $(i)_{a,b}$ truncated triangular profiles showing even symmetric arrangements of Au and $WO_3$ phases, (ii) faceted, and (iii) elongated. (a) and (b) are recorded using SE contrast only; (c) and (d) use mixed signals SE/BSE in order to reduce topographical image content. Scale bar in (a) is also valid for (b) and (d).

## At a glance.

I. Self-assembly of Au, W, and Au-W bi-layer thin films

• Pre-oxidized W ultrathin films are found to evolve into needle-like $WO_3$ nanorods (NRs) due to an anisotropic 1D oxide crystal growth which is not a dewetting mode in its usual manner

• Their aspect-ratio can be easily tuned by the annealing temperature

• For bi-layer thin films, both W and Au are revealed to evolve independently:

- The influence of stacking sequence was found to be substantial while individual Au layer thickness affects the degree of coverage in the as-deposited state
- W being the ground layer delays the dewetting of $Au/SiO_2$, acting as a non-wetting substrate
- W being the top layer even passivates the Au film and no dewetting occurs

• Combination of Au thin film dewetting and oxide NR formation results in the self-assembly of ordered arrays of Au-$WO_3$ NPs, potentially being used as a simple and cost-effective way to fabricate tailored Au-$WO_3$ nanostructures for photocatalytic applications

# 5 Morphology and microstructure evolution of Au-Ni bi-layer thin films

*The Au-Ni binary system provides a useful testing ground for the investigation of alloying effects on the dewetting of bi-layer thin films which defines the scope of this chapter. Individual layer thickness as well as stacking sequence is shown to potentially control void initiation in two-phase Au-Ni thin films at elevated temperature. Limited solubility of Au and Ni in solid state critically affects phase formation and void evolution. Dewetting at temperatures above the miscibility gap introduces Au-Ni solid solutions whose composition is determined by the thickness ratio of the initial bi-layer. Corresponding Au-Ni agglomerates are highly textured.*

## 5.1 The role of individual layer thickness and stacking sequence

Compared to single layer (one-component) and alloy thin films, bi-layers provide two additional parameters to be changed: individual layer thickness and stacking sequence. The following introduces how the morphology of thin Au-Ni bi-layers will evolve upon dewetting at medium temperature if these two parameters are systematically changed. Overall alloy compositions, which are determined by the thickness ratio of the bi-layers, are summarized in Table 3. Values ranging from 34 to 82 at.% Ni are situated within the miscibility gap according to the phase diagram at 500 °C. That means a two-phase equilibrium consisting of an Au- and Ni-rich phase is reached upon rapid thermal annealing.

Table 3. Au-Ni bi-layer films and their stoichiometric composition calculated from thickness ratios. Both Au and Ni were deposited in the same PVD coating unit, *i.e.*, Ni films were not exposed to air between deposition and annealing. Therefore, pre-oxidation of Ni films can be neglected in case of Au being the top layer.

| Bi-layer film | **Au** | **Ni** | Calculated alloy composition [at.% Ni] |
|---|---|---|---|
| Individual layer thickness [nm] | 5 | 15 | 82 |
| | 10 | 10 | 61 |
| | 15 | 5 | 34 |

Figure 60 highlights bi-layer film morphologies. It is seen that void initiation is not apparent in case of Au being the top layer (Figure 60b). Films are still unperturbed. Only chemical interdiffusion of Au and Ni is expected to occur. This is due to the fact that continuous films are formed for Au/Ni/$SiO_2$ upon deposition. In contrast, Au thin films are found to be discontinuous with *grooves* running through for 10 nm film thickness. Another thin Ni layer will just cover this relief (see Figure 60a, middle image). It is obvious that void initiation is

favored in this case. At 500 °C, mutual solubility of Au and Ni is limited, resulting in the formation of Au-rich and Ni-rich phases in the thin film. From a kinetic point of view, Au(-rich) material will be removed faster than Ni(-rich) matter due to different diffusivities [39]. This is why area density of voids is highest for the greatest volume content of Au-rich material, *i.e.*, 5 nm Ni deposited onto 15 nm $Au/SiO_2$ (Figure 60c). Of course, this phenomenological line of argument is only useful to make a statement about relative changes in film morphology. Individual features require special care and further investigations. However, the effect itself is clearly visible.

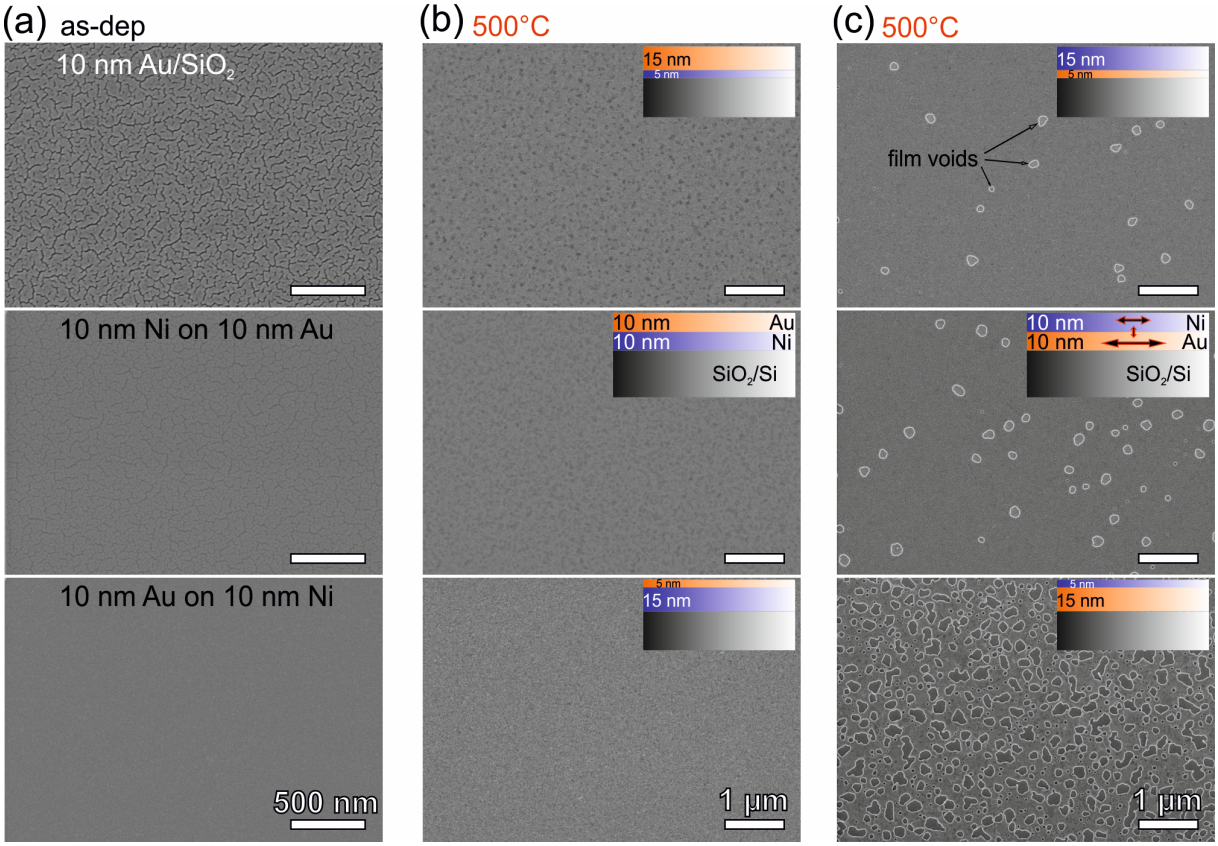


**Figure 60.** SEM micrographs of different Au-Ni bi-layer samples: (a) film morphologies in the as-deposited state as a function of stacking sequence for 10 nm individual layer thickness, (b) film morphologies upon annealing for 1 min at 500 °C as a function of individual layer thickness with Au being the top layer, (c) film morphologies upon annealing for 1 min at 500 °C as a function of individual layer thickness with Ni being the top layer. Total bi-layer film thickness is 20 nm in each case. Inserts illustrate all the bi-layer configurations considered. Double arrows in (c), middle image, indicate the magnitude of diffusion coefficients for *self- and interdiffusion* at that temperature. Scale bars are valid down the column.

At this point, one can conclude that the *film-substrate* interface determines whether critical (*i.e.*, viable) film voids are formed or not which is fixed by the stacking sequence of the Au-Ni bi-layer. The message here is that the morphology of the as-deposited state is a key factor for void formation in Au-Ni bi-layer thin films, rather than effects such as oxidation especially in

case of Ni being the top layer. A native oxide layer would actually hinder void formation of the overall bi-layer film due to passivation. Total number of initiated voids can be further controlled by individual layer thickness. In order to follow void initiation and their evolution in Au/Ni bi-layer thin films (column b in Figure 60), annealing temperature was increased.

Another highlight is presented in Figure 62. A mixed morphology is observed for a 15 nm Au/5 nm Ni bi-layer film upon annealing at 650 °C. A single film void is surrounded by plenty of bubbles. Such morphologies are rather unusual in the course of dewetting. However, formation of bubbles were also observed in a 200 nm Au thin film deposited on a ceramic substrate ($Y_2O_3$-doped $ZrO_2$, YSZ). *Shaffir et al.* state that the formation of bubbles is an alternative mechanism of thin film rupture [12]. Their rapid formation and subsequent fracture is indeed another way to break up thin films.

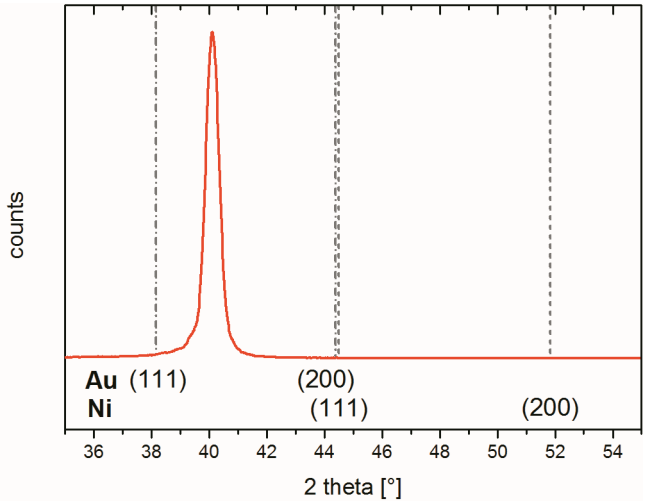


**Figure 61.** XRD pattern of the 2-theta range of interest of the as-annealed 15 nm Au/5 nm Ni bi-layer film. It is seen that only one phase is formed after annealing at 650 °C for 1 min. Peak position corresponds to approx. 39 at.% Ni as an estimate of the alloy composition after [79]. Using VEGARD's law would even lead to ~34 at.% Ni, which is in very good agreement with initial composition of the bi-layer film. However, thermal stresses due to rapid cooling may also contribute to peak shift.

A reasonable explanation for the formation of such cavities can be related to impurities chemisorbed onto the substrate prior to film deposition. During annealing, these substances (*e.g.*, water or carbon molecules coming from cleaning process) may turn into the gas phase generating some pressure which will cause the film to bulge out. Additionally, thermal expansion of the thin film may contribute here. Actually, cavity dimension is much smaller in the present case. This could be due to a size effect – total film thickness is decreased by a factor of 10 and, therefore, size of bubbles is supposed to shrink likewise. It is hard to believe that only this sample was subject to impurities. It is rather conceivable that phase formation plays a

major role. Figure 61 reveals that the film consists of one phase only, an Au-Ni solid solution. Rapid cooling facilitate conservation of this state at room temperature. Annealing took place at a critical temperature range: At 650 °C, stoichiometric composition (34 at.% Ni) is very close to the curve on the phase diagram that defines the limits of solid solubility. For ultrathin films with only a few nanometers in thickness, phase transition temperature is also decreased due to the size effect. Different coefficients of thermal expansion (pure Au: 14.2, Ni: 13.4 in $10^{-6}$ $K^{-1}$ at room temperature [80]) may then cause the one-phase Au-Ni thin film to bulge out, in a similar way to Au films. However, SEM image contrast indicates that (at least) some of the elevations contain "boundaries" which could separate (abnormal) grains, see Figure 62. Even phase boundaries would make sense. In other words, formation of bubbles might also result from regions in the thin film where phase separation yet happened (*i.e.*, due to an inhomogeneous temperature distribution over the sample during annealing). However, so far it is not quite clear why such bubbles *solely* formed in case of this particular bi-layer arrangement. It is left for future studies to clarify this observation. Also TEM investigations of a film bubble would help clarify whether there are grain/phase boundaries or not (*i.e.*, just being artificial features from SEM image contrast). Nonetheless this extraordinary sample was found to be worth mentioning at this point, indicating the complexity of multicomponent thin film dewetting.

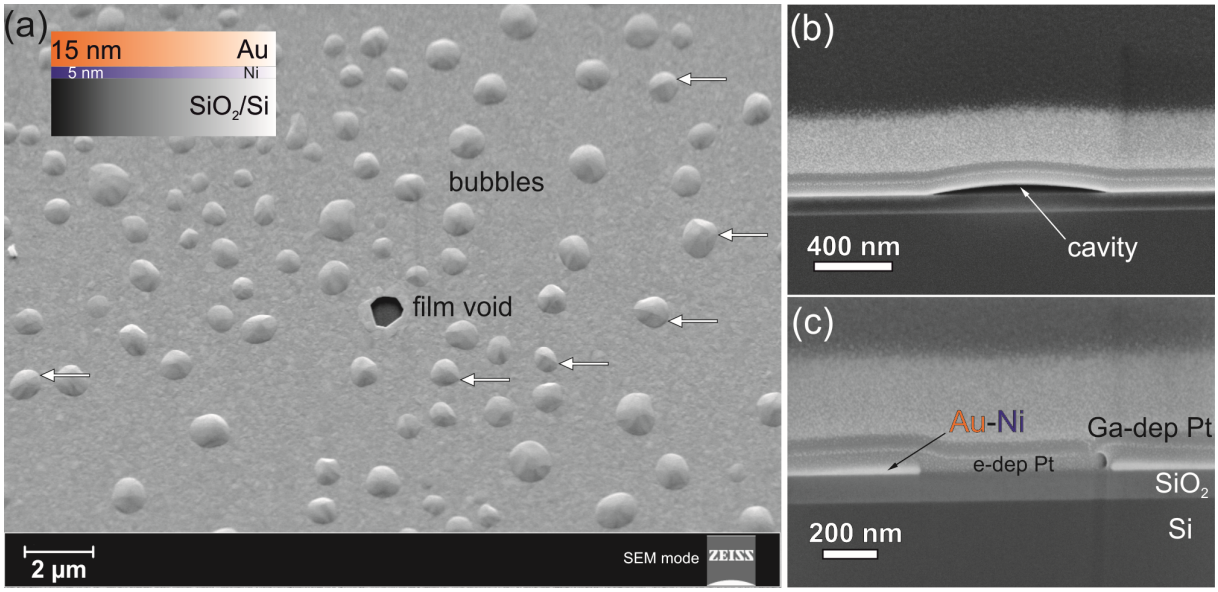


**Figure 62.** Film morphology of a 15 nm Au/5 nm Ni bi-layer upon annealing for 1 min at 650 °C: (a) SEM side view showing a mixed morphology consisting of few film voids and plenty of elevations, arrows indicate "boundaries" running through some of the elevations, (b) FIB cross-sectioning reveals that elevations are film bubbles (and not hillocks), (c) FIB cross-section of the film void showing faceted void edges. Pt precursor deposited via electron/ion beam-assisted GIS as well as Au-Ni/substrate are labeled.

## 5.2 Void evolution and phase formation

Alloying effects on the dewetting were recently investigated for Au-Fe as well as Au-Pt thin films [15, 37]. In either case, annealing took place in the solid solution regimes of the corresponding bulk phase diagrams. However, miscibility gaps were not considered.

In case of polycrystalline thin films, thermally induced film agglomeration is expected to occur rather fast due to short-circuit diffusion paths and plenty of void nucleation sites [37]. Thus, rapid thermal processing is suitable to study the dewetting of polycrystalline Au-Ni bi-layer thin films. In order to examine void evolution and Au-Ni phase formation in the course of dewetting, a successive increase in temperature passing the miscibility gap is applied (isochronal annealing, see Figure 63). During fixed annealing at different temperatures, consecutive dewetting stages will be reached due to increased diffusivities of the constituents. Effects of alloying on thin film morphology evolution will be highlighted. For analysis, in particular, a combination of electron microscopy and X-ray diffraction is used.

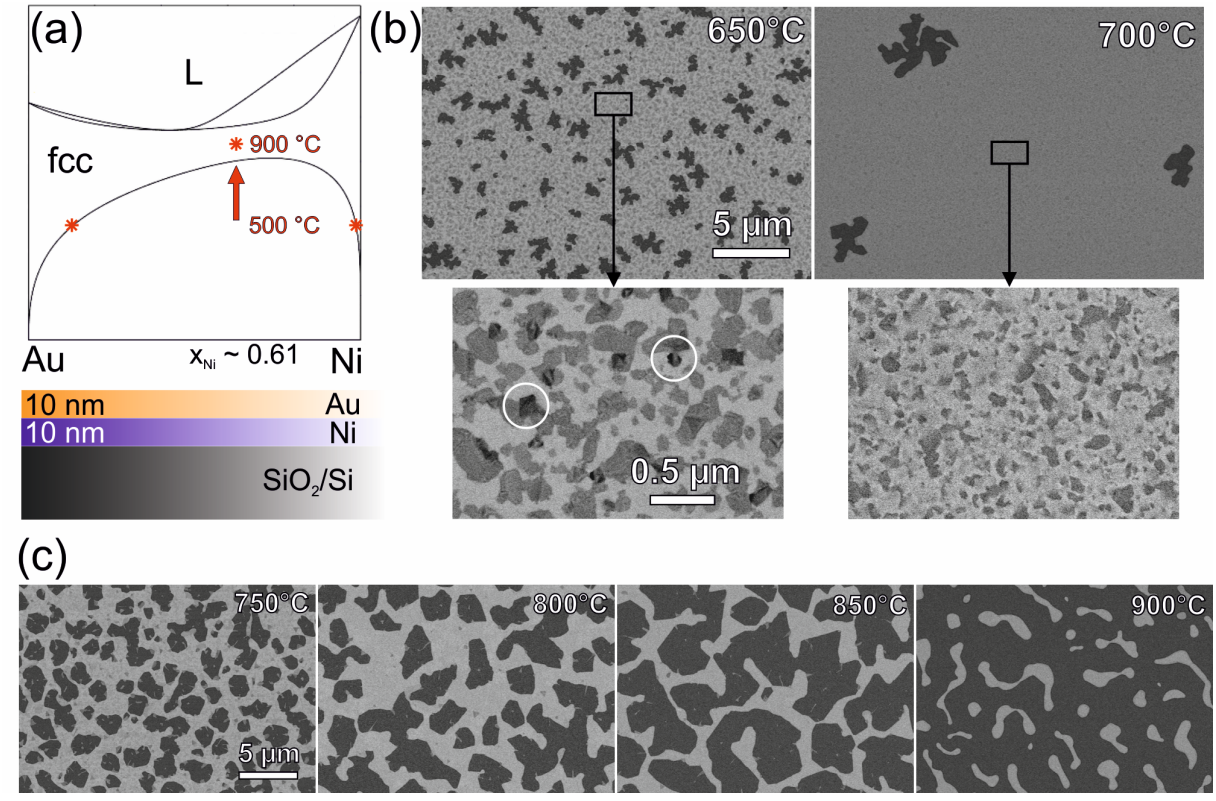


**Figure 63.** Morphology map. (a) Schematic drawing of the experimental approach used to probe the dewetting of an Au/Ni bi-layer thin film. Composition (~61 at.% Ni) is fixed by the thickness ratio of individual Au and Ni layers. Annealing temperature was successively increased from 500 °C (phase separation) to 900 °C (homogeneous solid solution). SEM micrographs at (b) medium and (c) higher temperatures using mixed signal SE/BSE. Annealing duration was 1 min at each temperature. Breakup regions appear darkest in contrast and are exemplarily encircled in (b).

### *5.2.1 Dewetting of Au/Ni bi-layers in solid-state by increase in temperature*

Morphology evolution of a 10 nm Au/10 nm Ni bi-layer thin film upon annealing is shown in Figure 63. This bi-layer arrangement ensures continuous film formation upon deposition and prevents Ni from oxidation when samples are exposed to air before annealing in furnace. SEM images reveal that different dewetting stages are reached upon short-term annealing at increasing temperatures. At 500 °C, void initiation is not apparent (see Figure 60). However, a few voids are likely formed considering the whole sample. At 650 and 700 °C, branched void growth is clearly visible. However, at 700 °C, much *fewer* voids are grown. Their greater extent can be related to a decreased incubation time $t_i$ for void initiation (assuming constant activation energy $E_i$, see Equation (3)),

$$t_i \propto e^{E_i/k_B T}. \tag{15}$$

Therefore, initiated voids are able to grow further during annealing for 1 minute. A closer look at the remaining film at 650 °C reveals that the Au-Ni thin film predominantly ruptures at the phase boundaries (see magnified images of Figure 63b). The mixed morphology consisting of initiated (*i.e.*, $t_i < t_{anneal}$) as well as growing voids indicates that void initiation does not necessarily occur simultaneously. This was also observed in polycrystalline Au thin films and is attributed to the different mechanisms involved during void initiation (*cf.* chapter 2) [15]. In contrast, no accompanying film rupturing is observed at 700 °C. Thus, from 650 to 700 °C, there must be a characteristic change in void growth mode. At 750 °C, expanding voids start to impinge, which is characterized by narrow links in the remaining film between two or more voids. Then, at higher temperatures, void coalescence is taking place leading to isolated post-film agglomerates after annealing at 900 °C. Figure 64 shows XRD pattern of the bi-layer sample treated at different temperatures. For each annealing experiment, a fresh sample was used. From 500 to 650 °C, two separate peaks arise according to the limited solubility of Au and Ni at these temperatures. At 700 °C, however, an additional intermediate broad peak appears. At 750 °C, even four peaks are distinguishable. The large peak width can originate from many factors such as grain size, dislocation density, microstrain or local variations in composition $Au_xNi_{1-x}$ in the remaining film. The former one can be excluded since rising temperatures implicate grain growth which would in turn implicate sharper peaks. Due to the fact that all samples were processed equally, changes in peak width caused by significant variations in dislocation density or modifications of internal strain (or stress) are assumed to be marginal. In this context, only variations in composition seem to be reasonable for peaks to broaden and even to overlap with each other.

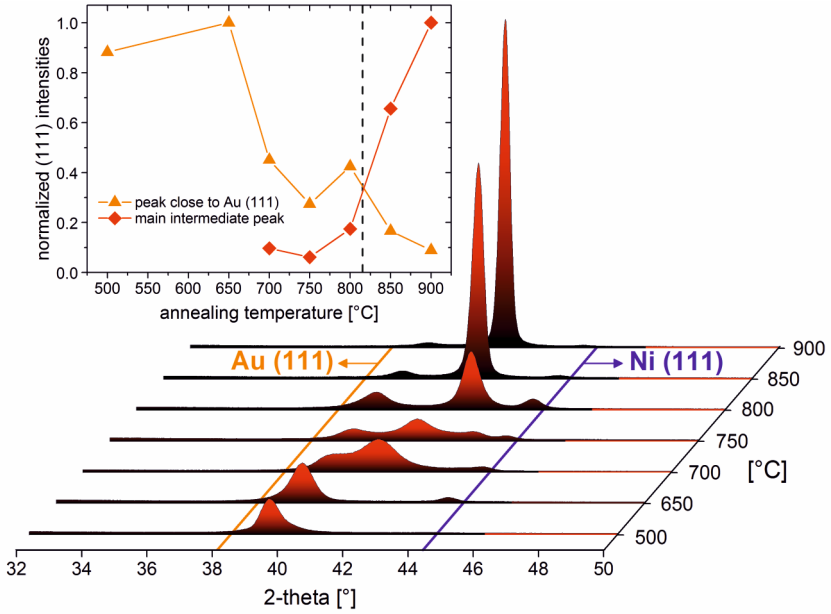


**Figure 64.** XRD pattern of Au-Ni thin films upon annealing showing the 2-theta range of interest: Corresponding (111) 2-theta positions of pure Au and Ni are indicated as full lines. At 500 °C, the very weak Ni peak is hard to see only due to the intensity scale. The inset shows the evolution of the relative intensities of the (111) BRAGG reflections upon annealing after subtracting the background (connecting lines are only meant to guide the eye). The dashed line within the inset represents the critical temperature of the miscibility gap at equilibrium condition, $T_C$ = 816 °C (1089 K) [81]. Solubility enhancement of Au and Ni well below this temperature causes the intensities of corresponding BRAGG peaks to change characteristically.

The XRD pattern of the sample annealed at 800 °C also shows that three phases are at metastable equilibrium. However, the intermediate peak reveals an increased shift toward Ni (111); its position corresponds to about 73 at.% Ni. For the sake of convenience in terms of alloying, composition of Au and Ni was deduced from the center positions of dedicated BRAGG peaks [79]. Since annealing was conducted close to the critical temperature of the miscibility gap ($T_C$ = 816 °C), a distinct phase formed in the range of the critical composition (71 at.% Ni). Annealing above the miscibility gap at 850 and 900 °C forms supersaturated Au-Ni solid solutions. From Figure 64 it is apparent that precipitation was mostly inhibited during rapid cooling. The composition derived from strong peaks in the XRD pattern is 64 at.% Ni, which approaches the initial one of the bi-layer (61 at.% Ni).

XRD pattern can be used to track the dewetting process since intensity evolution upon annealing is related to a height increase of sample features like grain growth [24]. Texture sharpening may also contribute here. In Figure 64, from 500 to 650 °C, the peak which represents the Au-rich phase (*i.e.*, which is close to the Au (111) 2-theta position) becomes stronger at early stages of dewetting probably due to grain growth and/or textural effects. However, its intensity rapidly decreases when metastable intermediate phases have formed at

700 °C. Upon further annealing, the gain in intensity of the main intermediate peak obviously occurs at the expense of the peak belonging to the Au-rich phase. This accounts for the fact that the diffusivity of Au is much larger than that of Ni in solid-state [39]. Thus, the intensity (and relative position) of the weak peak indicating a Ni-rich phase only shows a minor change upon annealing. Above the miscibility gap, annealing results in sharp peaks of high intensity. From this follows that Au/Ni bi-layer thin films reveal another sample feature, which can be used to track the dewetting by XRD, and this is the changing solubility of Au and Ni in solid-state.

### *5.2.2 Void formation and limits of solubility of Au and Ni*

In the Au-Ni binary system, the critical temperature of the miscibility gap at equilibrium is $T_C$ = 816 °C (1089 K). Annealing well below this temperature results in phase separation of Au-rich and Ni-rich material in the Au-Ni thin film according to the phase diagram. From theory of thermal grooving follows that surface flux $J$ is driven by the local surface curvature gradient $\partial_s\kappa$ at a given temperature $T$ (see Equation 2),

$$J_s = -(\boldsymbol{D_s}\gamma\Omega\nu/k_B T)\,\partial_s\kappa. \tag{16}$$

From all the parameters, the large discrepancy in diffusivity of Au and Ni should affect the overall mass flux *J(tot) = J(Au) + J(Ni)* most. Thus, void initiation as well as void growth is supposed to be determined by the mass flux of Au (or Au-rich) and Ni (or Ni-rich) material in the phase separating regime. At 650 °C, the Au-Ni film was found to break up at its phase boundaries. In Figure 65a, SEM cross-sectional view reveals that film rupturing occurs either via thermal grooving or void nucleation both located at the boundaries between Au-rich and Ni-rich phases. The former way will be determined by different mass fluxes: Since $D_S$*(Au)* > $D_S$*(Ni)* and *J(Au) > J(Ni)*, more Au-rich material will be reallocated in the remaining film resulting in a level difference between the two phases. Void nucleation as the bottom-up approach for initiating film rupturing may also be affected since interfacial energies of Au/$SiO_2$ and Ni/$SiO_2$ are quite different (Au/$SiO_2$: 0.39 J/m$^2$; Ni/$SiO_2$: 1.37 J/m$^2$) [82, 83]. The boundaries (or triple junctions at phase boundaries) between Ni-rich and Au-rich phases could therefore be the preferred position for void nucleation. In a recent study, cross-sectional characterizations of a thin Au/Ni bi-layer (individual layer thickness: 30 nm) were performed upon annealing at 675 °C for 1 h. Void nucleation at the film-substrate interface at Au/Ni/$SiO_2$ triple points could be verified. Moreover, void formation at phase boundaries inside the Au-Ni film was found to occur by the KIRKENDALL effect [84]. Inhomogeneity in film morphology due to rapid cooling (*e.g.*, quenched vacancies) is supposed to contribute here, too.

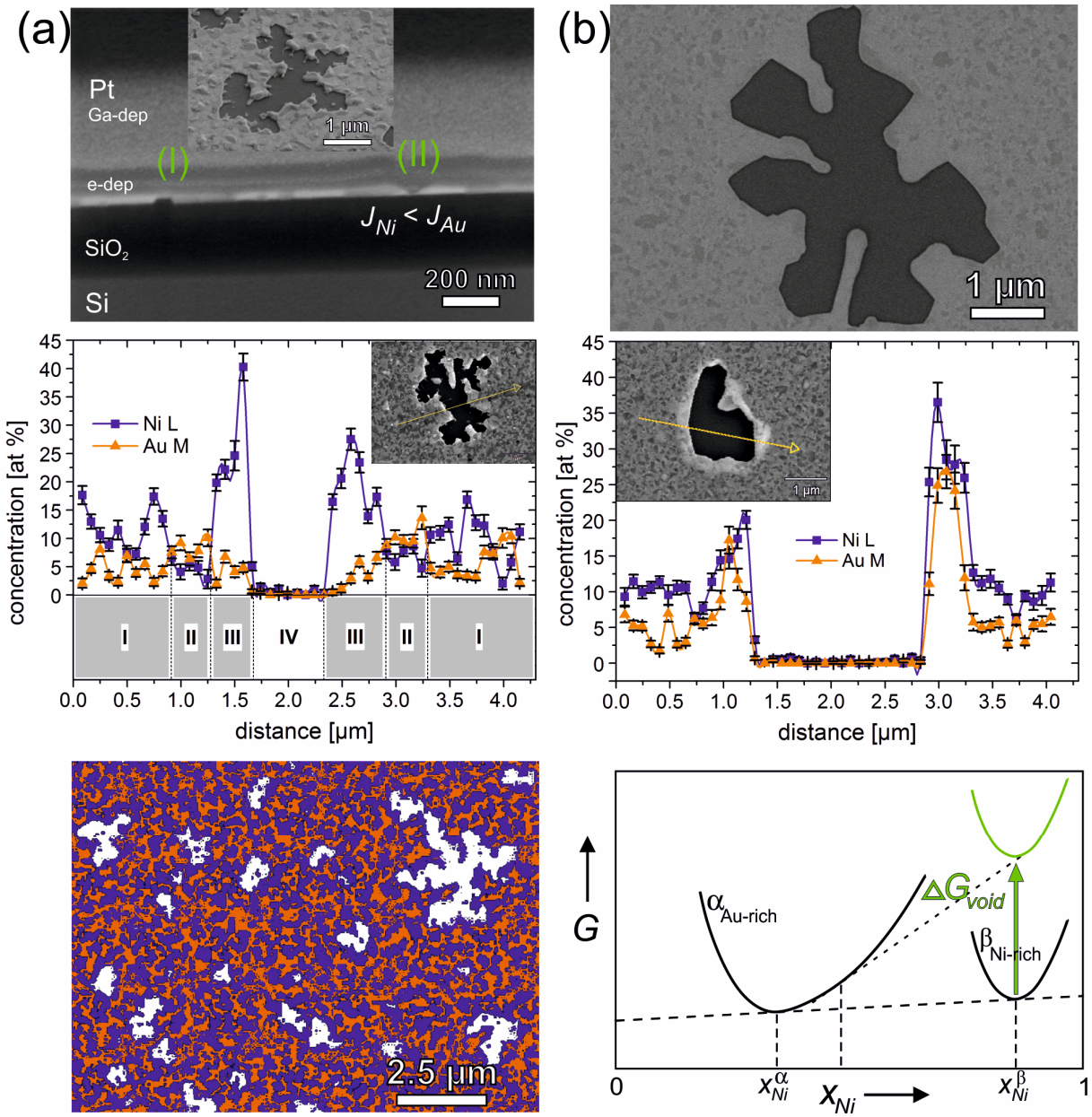


**Figure 65.** Void characteristics in phase separated Au-Ni thin films. (a) At **650** °C, voids nucleate at Au/Ni/$SiO_2$ triple points (position **I**) or thermal grooves are formed (position **II**). A certain level difference between the pile-up of Au-rich and Ni-rich material due to different mass fluxes *J(Au)* and *J(Ni)* is observed. A uniform void rim is missing. An EDS line scan of a branched void shows a characteristic sequence of zones: the phase separated film (region **I**), Au-rich material (**II**), Ni-rich rim (**III**), and the void (**IV**). Please note that absolute concentration values are not conclusive due to topographic effects and substrate contributions to the total signal. The arrow within the inset represents the EDS line scan performed. Phase mapping using Z-contrast reveals that void growth occurs via the Ni-rich phase (indigo refers to a Ni-rich phase; orange indicates the Au-rich phase). (b) At **700** °C, void growth appears to be more regular and faceted. The SEM micrograph consists of mixed signal SE/BSE. Z-contrast predominantly remains in the Au-Ni film still indicating phase separation. EDS indicates a relative solubility enhancement of Au and Ni at the rim zone. The arrow in the inset illustrates the line scan performed along the void. Thermodynamic specification of the situation is further illustrated.

During annealing at 650 °C, initiated voids were found to evolve in a branch-like manner. In Figure 65a, SEM side view imaging indicates that a uniform, elevated void rim is missing during void growth, which is in contrast to polycrystalline Au thin films (*cf.* chapter 2). An EDS line scan of an individual branched void indicates that growing voids are preferably surrounded by Ni-rich material: Due to the larger diffusivity of Au, more Au-rich material moved away from voids via surface diffusion and/or other active diffusion paths. A kind of zone model can be established at this point. The phase-separated thin film merges into Au-rich material followed by a Ni-rich rim, which surrounds the branched void. From this follows that void growth solely occurs via the Ni-rich phase, which can be seen from a corresponding phase map also provided in Figure 65a. In this context, long-term annealing at 650 °C results in Ni-Au bi-metallic nanoparticles via dewetting [1].

### *5.2.3 Solubility enhancement in the void growth stage*

In the phase separating regime at 650 °C, the Au-Ni film preferably ruptures at the phase boundaries and growing voids were found to evolve via the Ni-rich phase. According to the thermodynamics of alloys, equilibrium conditions for two stable phases (*e.g.*, $\alpha$ and $\beta$) correspond to the equality of dedicated chemical potentials $\mu$ [23],

$$\mu_i^{\alpha} = \mu_i^{\beta}, \tag{17}$$

where *i* stands for Au and Ni, respectively. In the course of dewetting, the *effective* area of the Ni-rich or $\beta$-phase increases during branched void growth ($\mathrm{d}a > 0$) and, therefore, GIBBS free energy of that phase increases for a positive surface energy ($\gamma > 0$) according to Equation (10),

$$\mathrm{d}G = \gamma \mathrm{d}a > 0. \tag{18}$$

This gain in GIBBS free energy causes Au and Ni mutual solubility to rise at the rim zone of evolving voids and, in turn, results in three (or even four) phase equilibria in the Au-Ni thin film. This was indeed observed at 700 °C and higher temperatures (see XRD pattern in Figure 64). Figure 65b catches the situation described. As a consequence of this, void growth appears to occur in a more regular, faceted manner. Z-contrast is visible predominantly in the remaining Au-Ni film still indicating phase separation. Another feature did also change: A uniform, elevated rim can now be deduced from SEM imaging. More Au in the rim zone obviously causes voids to turn into a growth mode, which is similar to that in polycrystalline pure Au thin films (*cf.* chapter 2). EDS investigations emphasize the effect of alloying on morphology evolution.

At 700 °C, moreover, almost no film rupturing was discovered and only sparsely populated growing voids were observed (see Figure 63b). From a kinetic point of view, changing solubility of Au and Ni (*i.e.*, interdiffusion) may hinder material removal from straight initiated voids–meaning that there are *competing* mechanisms in the course of solid-state dewetting of Au/Ni bi-layer thin films. This obviously makes the Au-Ni film remarkably stable to rupturing and, in turn, the number density of viable voids is decreased. At this point one can conclude that a kind of *self-healing* occurs due to alloying. The effect of grain growth, *i.e.*, available grain boundary area as thermal grooves or nucleation sites during void initiation and as a possible diffusion pathway during void growth can be assumed to be marginal here since annealing was of short duration at these elevated temperatures (650 °C and 700 °C).

## 5.3 Dewetting at temperatures above the miscibility gap

Figure 66a highlights the morphology of the Au-Ni film after complete dewetting: Elongated and flat agglomerates are formed during annealing at 900 °C for 1 minute (*i.e.*, beyond the miscibility gap in the solid solution regime). The uniform height represents the dewetted state. The homogeneous EDS profile along such a structure indicates the formation of supersaturated Au-Ni solid solutions. Only marginal fluctuations are visible. The weighted mean of the Au M and Ni L signal excluding the experimental scatter (*i.e.*, regions where the total signal is less than 100 at.%) yields 38(1) at.% Au and 62(1) at.% Ni, which is in good agreement with XRD results. Figure 66b shows an elongated agglomerate from a cross-sectional view in TEM. Selected area electron diffraction gives evidence that the agglomerates reveal a single crystal character and (111) crystallographic orientation. In compliance with XRD, grain growth as well as texture sharpening dominates the dewetting in the solid solution regime of the Au-Ni binary system. Moreover, there is a considerable increase in thickness, *i.e.*, the height of the elongated, flat structure (approx. 100 nm) is 5 times larger than the initial bi-layer. Therefore, the morphological transformation from the Au/Ni bi-layer into flat agglomerates can be considered as an oriented growth of Au-Ni solid solutions in the course of solid-state dewetting.

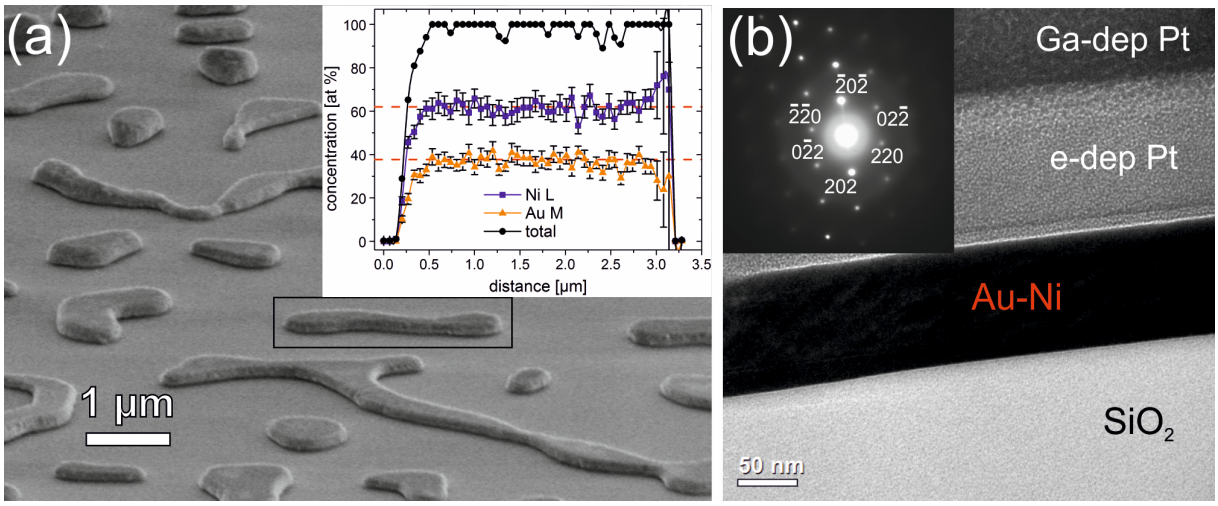


**Figure 66.** SEM side view of the dewetted Au/Ni bi-layer is shown in (a): Elongated and flat Au-Ni agglomerates are formed after annealing at 900 °C for 1 minute. Subsequent processes such as particle equilibration are not considered in this work. An EDS profile of an Au-Ni agglomerate is included in (a): The weighted means of the Au M and Ni L signals are marked by dashed lines. A cross-sectional view by bright field TEM is depicted in (b). The dewetted Au-Ni film appears uniformly dark in image contrast due to the strong scattering power of Au in the fcc solid solution. Selected area electron diffraction indicates [$\bar{1}$11] beam direction and, in turn, (111) crystallographic orientation. Pt layers on top of the Au-Ni structure, which were deposited as protection layers via electron and Ga beams prior to FIB processing, are also labeled.

## At a glance.

II. Solid-state dewetting of Au-Ni bi-layer thin films

• Stacking sequence and individual layer thickness critically affect void formation at elevated temperatures

• Further void evolution of selected bi-layer systems can be well studied by screening the Au-Ni phase diagram by means of rapid thermal annealing technique

• For a **10** nm Au/**10** nm Ni, voids are found to

- initiate at phase boundaries either via nucleation or grooving
- evolve via the Ni-rich phase
- change Au-Ni mutual solubility

• A certain degree of thin film self-healing is observed due to the effect of alloying

# 6 Preparation of tailored functional Au-Ni micro- and nanoparticles

*A bi-layer made up of the ferromagnetic 3d-transition metal Ni and the catalytically active Au could provide a convenient basis for the fabrication of novel Au-Ni alloy micro- and nanoparticles. In a preliminary work, the dewetting behavior of Ni/Au bi-layer films was investigated for the first time [1]. There, bi-metallic nanoparticles formed via dewetting reveal an enhanced solid solubility at the nanoscale. In this chapter, it will be shown how this approach can be refined in order to create tailored Au-Ni alloy particles using physical principles at reduced scale.*

## 6.1 Solid solution and supersaturation

Rapid thermal annealing was conducted above the miscibility gap at 950 °C for 1 min. Fast cooling in furnace was used to retain Au-Ni solid solutions at room temperature. Bi-layer thin film dewetting then results in the formation of supersaturated Au-Ni alloy particles in the submicron range (Figure 67).

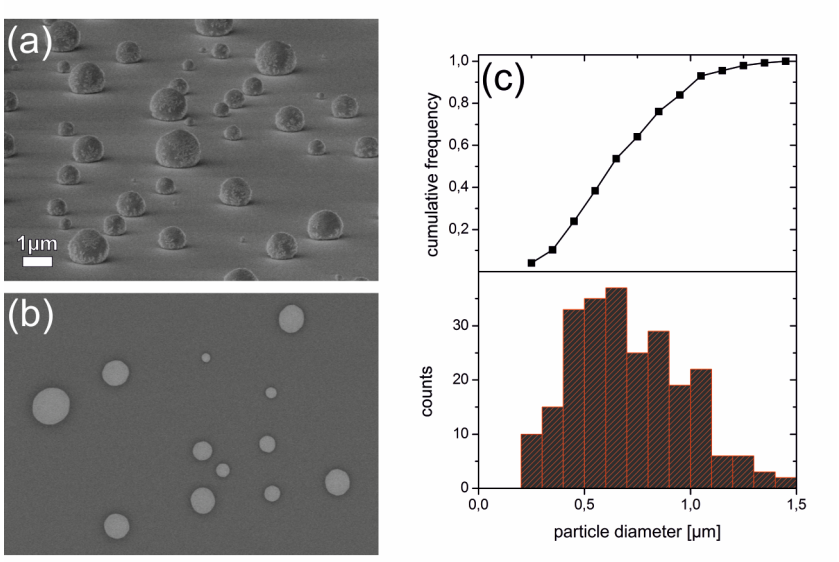


**Figure 67.** SEM micrographs. Side-view image at 80° tilt using SE signal is shown in (a), a top-view image using mixed signal SE/BSE is shown in (b). The scale bar is valid for both SEM images. The corresponding particle size distribution is illustrated in (c). Feature sizes were calculated using the analyze particles tool of the free software ImageJ [73].

As can be seen, spherical particles are formed via dewetting after rapid thermal treatment. These particles do not show any Z-contrast indicating that no phase separation occurred during cooling. Particle sizes tend to follow a log-normal distribution. Most of the particles (about

84%) possess a diameter in the submicron range. Figure 68 shows an EDS line scan profile of an arbitrarily chosen particle. Neglecting edge effects due to its spherical shape, concentrations of Ni and Au look quite homogeneous along the particle. This indicates an Au-Ni solid solution. However, concentration fluctuations visible in Figure 68 might be caused by small precipitates. There is an area in the EDS line scan where no influence of the substrate is visible (*i.e.*, the total signal of detected Ni and Au has reached 100 at.%). Calculating the weighted mean of that concentration range for at least three particles being similar in size yields 34(1) at.% Au, which is close to the corresponding value of the as-deposited bi-layer film (39 at.%). It should be noted that the spherical shape of the particles causes the beam interaction volume to deform. The EDS signal derived from that volume is therefore influenced by the topography. In contrast, a clear abruption of concentration profiles was found in case of bi-metallic Au-Ni nanoparticles formed after annealing and subsequent slow cooling, and this means that Au-rich and Ni-rich phases are present in individual particles [1].

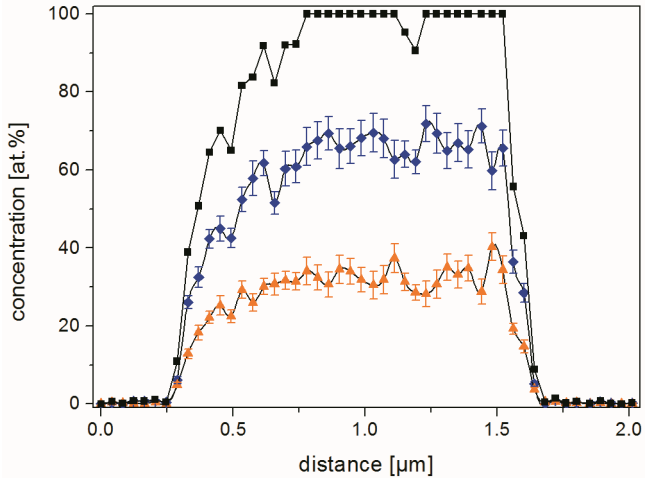


**Figure 68.** EDS line scan profile of an arbitrary particle. Ni L (♦) and Au M (▲) signals are shown including error bars. Total signal of detected Ni and Au (■) is also illustrated.

XRD pattern of the as-deposited 10 nm Au/10 nm Ni bi-layer film as well as Au-Ni particles are shown in Figure 69. It can be seen that there are sharp peaks being close to the broadened Si (400) peak. These contributions can be attributed to the substrate as they do not change upon annealing. In the as-deposited state, a peak belonging to Au (111) appears. The weak peak at higher angles cannot be distinguished whether to belong to Ni (111) or Au (200). The intensity ratio of the (111) to (200) peak can be used as a qualitative measure of the out-of-plane texture. From powder diffraction files, one obtains a ratio of 1.92 for Au (PDF 00-004-0784) and 2.38 for Ni (PDF 00-004-0850). Ascribing the weak peak to Au (200) indicates that the intensity ratio of the as-deposited state is much higher than that of an ideal powder. Therefore, the bi-

layer film exhibits a pronounced (111) out-of-plane texture. Due to the high surface-to-volume ratio of thin films, the bi-layer film is expected to expose the surface of lowest energy, and this is the (111) surface [85]. Initial grain size is 9 nm, which is estimated from Au (111) peak. This means that grain size is of the order of individual Au film thickness of the bi-layer film. Such a relation is well known for most metallic thin film deposition methods.

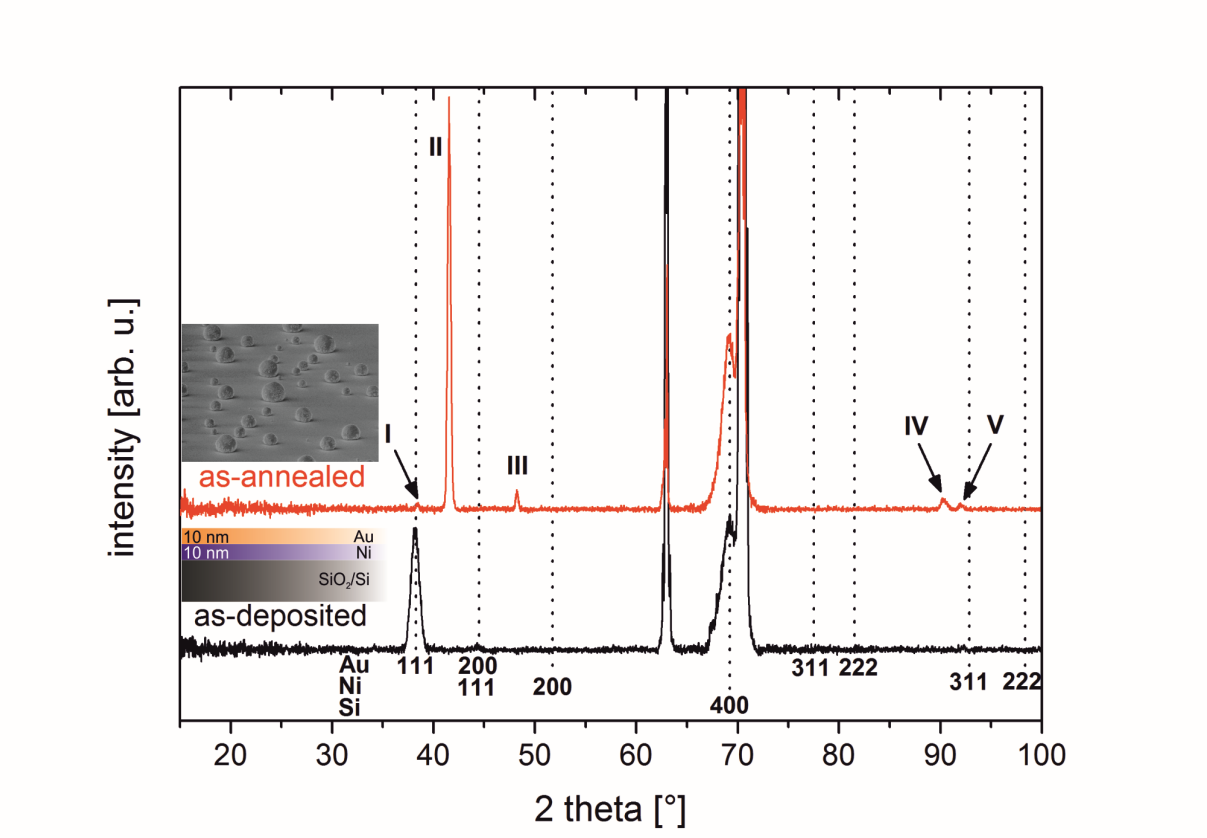


**Figure 69.** Diffraction pattern of the as-deposited bi-layer film (black) and the particles (red) after subtracting the background. Peak positions of Au, Ni, and Si are also indicated (see dotted lines, taken from corresponding PDF). Grain sizes in the as-deposited state were estimated from Au (111) BRAGG peak by the SCHERRER formula using the full width at half maximum (FWHM) of a GAUSSIAN fit. Measurements of a single crystalline silicon sample were taken in order to subtract instrumental line broadening.

After annealing and rapid cooling in furnace, the Au (111) peak nearly disappears and is slightly shifted rightwards (marked peak I in Figure 69). A sharp peak arises at 41.55° instead which leads to a lattice spacing of about 0.376 nm and corresponds to a solid solution with 37 at.% Au [79]. The initial Au/Ni bi-layer thickness ratio is equivalent to 39 at.% Au and 61 at.% Ni, respectively. Deviations could result either from (marginal) thermal stresses due to quenching (which would relate to a peak shift as well) or evaporation effects during annealing. There is a model of evaporation of metal nanoparticle arrays which was experimentally proved for Au and Ni nanoparticles on sapphire [33]. Due to its lower melting point (1064 °C), a larger

quantity of Au is expected to evaporate from the substrate upon annealing at 950 °C. This loss of mass may lead to the observed small change in stoichiometry. Marked peaks III and IV in Figure 69 can be identified as (200) and (222) peaks belonging to the solid solution. These relatively weak peaks exhibit a poor goodness of fit and, therefore, were not taken into account for calculating quantities. (111)/(200) peak intensity ratio is approx. 20. Hence, (111) texture of the bi-layer was preserved after annealing-induced grain growth and dewetting. The fifth peak seems to belong to Ni (311). Its clear shift is most likely due to alloying.

To sum up, alloy composition can be defined by the thickness ratio of the Au-Ni bi-layer film. Subsequent annealing at high temperature in the homogeneous solid solution regime induces particle formation through bi-layer thin film dewetting. From a local point of view, EDS reveals that the composition of some particles may differ from that obtained by XRD. Anyway, the combination of both methods clearly proves that *supersaturated, (111) oriented Au-Ni alloy particles* are formed whose composition approaches the one of the former Au/Ni bi-layer film.

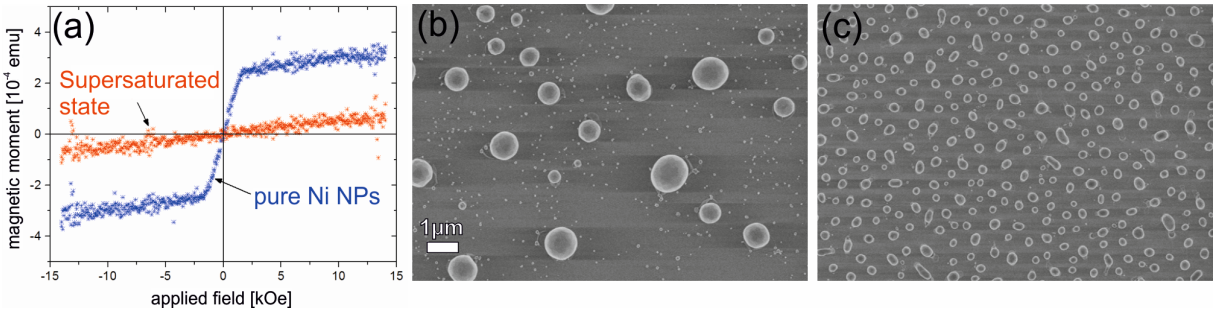


**Figure 70.** Magnetic properties of metal nanoparticles. (a) VSM measurements of (b) supersaturated Au-Ni particles and (c) pure Ni particles. The scale bar is valid for both SEM images. It is seen that the supersaturated state unveils paramagnetic behavior at room temperature.

Magnetic properties of the Au-Ni alloy particles were finally investigated by utilizing a vibrating sample magnetometer (VSM, *Micromag™3900, Princeton Measurements Corp., USA*). Samples were mounted parallel to the external field which means an in-plane setup. In order to obtain an adequate signal, individual layer thickness was increased to 20 nm (sample size: 25 $mm^2$). In this case, stoichiometric composition of the bi-layer is not changed. The same layer thickness (20 nm) was used for the dewetting of a Ni single layer film at equal conditions. Since total film thickness of the bi-layer (40 nm) is bigger than the one of the Ni layer, mean size of the supersaturated Au-Ni particles formed is increased as well. The diamagnetic background of the $SiO_2$/Si substrate was subtracted by measuring blank samples. VSM measurements at room temperature indicate a change from ferromagnetic (pure Ni particles) to

paramagnetic behavior (see Figure 70). Their paramagnetic volume susceptibility is estimated to be $10^{-2}$ (cgs-units). *Cheung et al.* [86] state that an isolated Ni impurity atom does not form a stable magnetic moment in a nonmagnetic metal host. The onset of ferromagnetism can be derived from cluster interactions as the critical Ni concentration is exceeded. *Kuentzler and Kappler* [87] found a linear relationship between CURIE temperature and Ni concentration being greater than 50 at.%. Based on this, the CURIE temperature of an Au-70 at.% Ni alloy corresponds to 275 K (~2 °C), which is below room temperature. One can thus maintain that Au-Ni solid solution formation suppresses ferromagnetic coupling at room temperature. Consequently, supersaturated Au-Ni particles show paramagnetic behavior. This study provides a useful route to obtain Au-Ni alloy particles of defined composition and, therefore, fixed (magnetic) properties.

## 6.2 Substrate effects

The same experiment was conducted on inverted pyramidal pit arrays. In order to obtain regular arrays of supersaturated Au-Ni alloy nanoparticles of similar size and spacing, individual layer thickness was adjusted. Now, an 18 nm Au/18 nm Ni bi-layer thin film was deposited on the pre-patterned $SiO_2$/Si substrate. At this point it should be noted that Au/Ni bi-layer thin films are found to be more sensitive to film thickness than Au thin films in forming ordered arrays of nanoparticles.

The following compares microstructural features of Au/Ni bi-layer films upon annealing with respect to the substrate type. Figure 71a shows the morphology obtained after annealing of a 20 nm thin Au/Ni bi-layer film deposited on the flat $SiO_2$/Si substrate. Spherical Au-Ni particles in the submicron range are formed after dewetting at 950 °C for 1 min. Only marginal faceting is visible after short-term annealing. Figure 71b shows Au-Ni nanoparticles each located in one pit after templated dewetting of a 36 nm Au/Ni bi-layer thin film at equal conditions. Here, faceting appears in a more pronounced but irregular way. Figure 71c depicts corresponding XRD pattern of the two samples indicating that, in either case, supersaturated Au-Ni solid solutions are formed after thermal treatment. From (111) and (200) peak intensities it is obvious that there is a change in texture after bi-layer dewetting on different substrate types. In case of the flat substrate, a distinct (111) out-of-plane texture is observed. Both as-deposited Au/Ni bi-layer films and Au single layer films reveal a strong (111) crystallographic texture, which is going to be inherited by the particles after dewetting [55]. In case of the pre-patterned substrate, however, supersaturated Au-Ni nanoparticles do not show any preferred orientation.

This is quite contrary to Au thin films which revealed a distinct (100) crystallographic texture after templated dewetting [55]. However, it should be noted that the said Au films were annealed at 850 °C for 2 h. Thus, the dewetted state does not have to be the same. From this it follows that–after short-term annealing–(111) side walls of the pyramidal pits do not influence the faceting of the supersaturated Au-Ni nanoparticles at least in early stages.

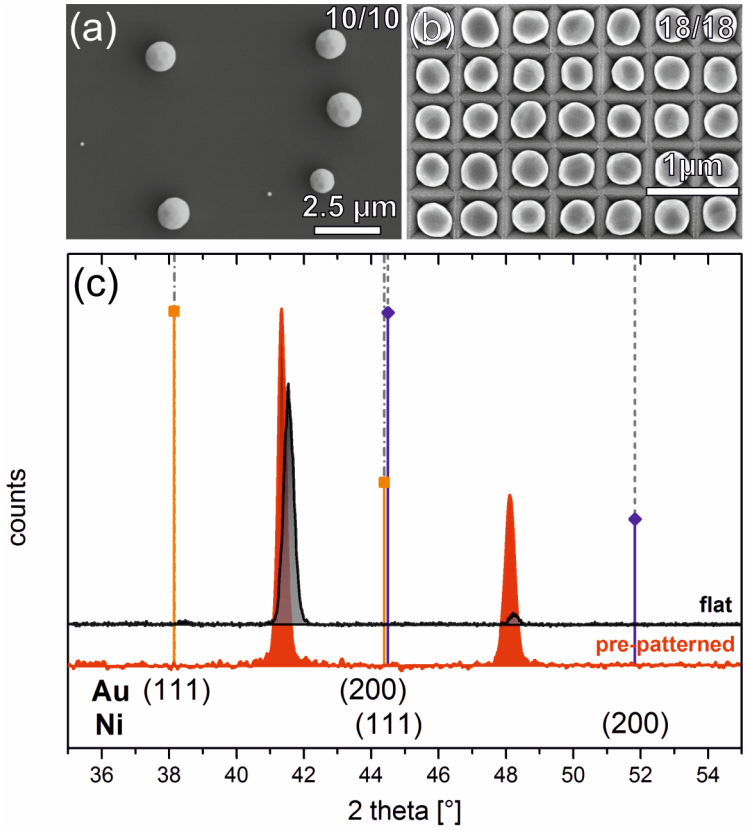


**Figure 71.** Templated Au/Ni bi-layer thin film dewetting. SEM micrographs of supersaturated Au-Ni particles formed via dewetting of an Au/Ni bi-layer film upon annealing at 950 °C for 1 min on (a) flat and (b) pre-patterned $SiO_2$/Si substrate (numbers in pictures give Au/Ni film thickness in nanometers). Corresponding XRD pattern of the 2-theta range of interest is shown in (c). Au (■) and Ni (♦) peak positions as well as relative intensities are indicated using dedicated PDFs.

Upon annealing, a second feature of *templated* bi-layer dewetting is a certain peak shift toward Au BRAGG peaks relative to the particles formed via dewetting on the flat substrate. Since the composition of the Au/Ni bi-layers deposited on both substrate types is the same and an equal thermal treatment was applied, this peak shift turns out to be caused by the substrate itself. Figure 72 shows EDS line scan profiles of both a supersaturated Au-Ni nanoparticle located in a pyramidal pit and two still joint Au-Ni nanoparticles (which indicates incomplete dewetting). EDS of the single particle indicates a homogeneous Au-Ni solid solution, taking the error margins into account. Measured concentration values of Au and Ni further correspond to the initial composition of the bi-layer film (39 at.% Au and 61 at.% Ni, respectively). Looking

at the joint particles reveals a different behavior: On the mesa, the joint obviously comprises some Au-rich material whereas the main bodies of the particles formed within the pits show similar EDS signals for Au and Ni like the single particle. There are inhomogeneous regions where the total signal is less than 100 at.%, which is probably caused by topographical effects and/or contributions from the substrate. However, this is not the case for the joint region on the mesa. Since there are several joint Au-Ni nanoparticles on the pre-patterned substrate, the solid solution peak is caused to shift toward Au BRAGG peaks in the XRD pattern.

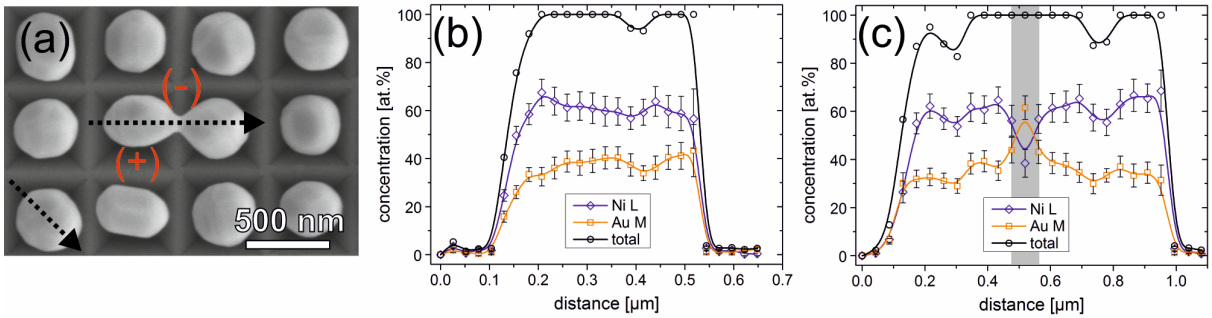


**Figure 72.** EDS analysis of individual Au-Ni particles on the pre-patterned $SiO_2$/Si substrate. (a) SEM micrograph showing single as well as joint particles. Dotted arrows indicate line scans performed. Surface curvature is changed from positive (+) to negative (–) along the profile of joint particles. (b) EDS line scan profile of the single and (c) joint particles. The mesa region is highlighted by the gray area in the line scan. For better visibility, data points of the line scans were interpolated using B-splines.

An explanation for this behavior can be given using Equation (2) in chapter 2.2. Upon annealing, *a priori*, total surface flux obeys $J_{tot} = J_1 + J_2$ in case of a bi-layer or alloy thin film. $J_1$ and $J_2$ are the contributions of the corresponding constituents to the total mass flux (here, Au and Ni). On the one hand, there is a vertical mass flux induced from the mesa edges (positive curvature) to the apex of the pits (negative curvature), which facilitates the formation of Au-Ni nanoparticles within the pyramidal pit. Since annealing takes place above the miscibility gap of Au and Ni, solid solutions are formed and retained to room temperature. In case of incomplete dewetting (joint particles), Au-rich material situated on the mesa only can form if $J_1$ and $J_2$ are different. This would implicate that the vertical mass flux of Ni or Ni-rich material must be greater than that of Au or Au-rich material. But this might not hold since the diffusivity of Ni or Ni-rich material is much lower than that of Au or Au-rich material [39]. As can be seen from Figure 72a, however, joint particles themselves form a new horizontal surface negative curvature (concave at the joint). Therefore, an *additional* mass flux is generated from the main bodies of the incompletely dewetted particles (positive curvature) to the joint region on the mesa (negative curvature). Because the diffusivity of Au is larger than that of Ni, Au-rich

material is found on the mesa. Again, this observation means that there are competing mechanisms being active during dewetting of multicomponent thin films.

## 6.3 Facet-controlled phase separation upon shape equilibration

A useful side effect of the dewetting of thin metal films is, in solid state, the fact that single crystal, nearly defect-free faceted particles are formed [48]. For face-centered cubic (fcc) crystals like Au, the equilibrium crystal shape (ECS) corresponds to a truncated octahedron with the {111} and {100} facets as the only two stable orientations [10, 13]. At this point, it is not obvious how metal particles will equilibrate in case of an alloy since (anisotropic) surface, interface and elastic energies of more than one constituent as well as kinetic effects are involved. *Amram et al.* [48] state precisely that the lack of structural defects, internal thermal stresses and faceting may have crucial influence on phase formation in alloy particles with a lateral dimension in the submicron range. Here, faceting is supposed even to assign a certain symmetry to the spatial arrangement of precipitates because contact regions (*e.g.*, edges or triple points) of the atomically flat surfaces can be considered as the favorable nucleation sites.

### *6.3.1 A two-level experimental approach*

In this study, the Au-Ni binary alloy serves as a model system for studying alloy particle equilibration based on the same crystal structure of the constituents. In spite of the same WULFF shape, an extra complexity upon phase separation is related to the question how Au and Ni (*in terms of phases*) should arrange in the particle once reaching its ECS. There are three sites for initially accumulating Au or Ni: (i) the interface between particle and $SiO_2$, (ii) the particle interior, and (iii) the faceted surface. The interface region is expected to be enriched by Au as the corresponding interfacial energy (0.39 J/m$^2$) is much lower than that of Ni/$SiO_2$ (~1.37 J/m$^2$) [82, 83]. The interior of the particle should not be favored for precipitation due to the lack of defects inside inhibiting heterogeneous nucleation. Eventually, an overall core-shell formation would implicate high internal stresses thinking of the large lattice mismatch of about 15% between Au and Ni [46]. It is thus obvious that faceting will play a decisive role for phase formation in Au-Ni alloy particles. However, precipitation of a second phase on a facet as a whole might be challenging due to a strongly decreased area density of mobile atoms [48].

Figure 73 shows the experimental procedure applied in this study. Starting from an Au/Ni bi-layer thin film, which is deposited using electron beam evaporation, supersaturated, (111) oriented Au-Ni alloy particles are formed via thermal dewetting at high (950 °C) temperature and subsequent fast cooling. Their composition amounts to ~61 at.% Ni which is determined

by the initial thickness ratio (10 nm Au/10 nm Ni) of the bi-layer. For further details please see corresponding chapters/sections above. In this mixed state, Au-Ni particles show spherical shape which is also observed for Ag-Au particles [47, 88].

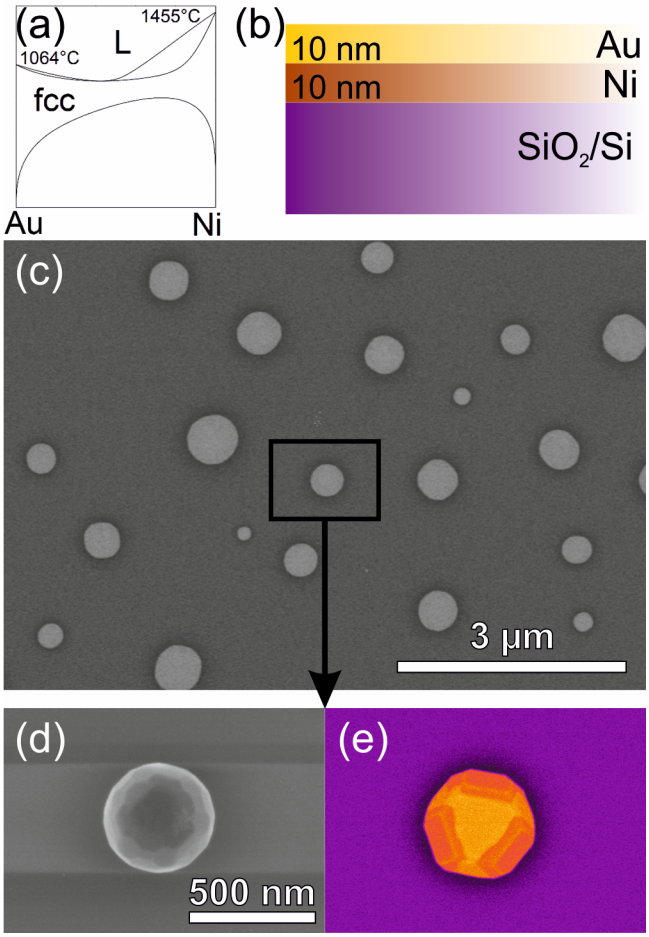


**Figure 73.** Experimental "roadmap" for studying features of physical metallurgy at the mesoscale. (a) Sketch of the equilibrium Au-Ni phase diagram including melting points of Au (1064 °C) and Ni (1455 °C), (b) the Au/Ni bi-layer thin film, (c) SEM micrograph of the supersaturated Au-Ni alloy particles using mixed signal SE/BSE, (d) high-resolution view of an individual alloy particle showing nano-faceting upon annealing at 950 °C, (e) Pseudo-color image (derived from backscatter mode) of an equilibrated Au-Ni nanoparticle upon annealing at 650 °C showing side facets which are accumulated by Ni. Scale bar is the same for both (d) and (e).

A closer look at the supersaturated Au-Ni alloy particles reveals that the surface actually consists of poorly developed *nano-facets*, meaning that plenty of nucleation sites are available on the free surface (Figure 73d). Moreover, such freestanding edges may undergo instabilities upon annealing: The situation, generally speaking, is coincident with rectangular voids initially formed in the course of solid-state dewetting in single crystal Ni thin films. Such holes are found to evolve by corner-induced instabilities [20]. Both dewetting and particle shape equilibration are driven by surface (and interface) energy minimization. In other words,

underlying mechanisms of particle shape evolution may include such corner instabilities to possibly form the ECS by eliminating unfavorable facets. Figure 74 shows a former supersaturated Au-Ni alloy particle after rapid thermal annealing at 650 °C for 6 min as well as corresponding X-ray diffraction pattern in BRAGG-BRENTANO geometry. This intermediate state shows that Au-rich and Ni-rich phases (according to the phase diagram at this elevated temperature) indeed precipitate on the faceted surface whereas the interior of the particle remains supersaturated at early stages of shape equilibration. This indicates that phase formation strongly correlates with the evolution of facets. Figure 73e finally shows the equilibrated Au-Ni particle. It can be seen that the WULFF shape has formed in such a way as to enable Ni accumulating at the {100} side facets of the truncated octahedron. This is rather puzzling as a surface energy argument would favor both Au and Ni on the {111} facets and, moreover, a volume argument would favor Au on the {100} faces. In a previous work, the formation of Ni-Au bi-metallic, but irregularly shaped nanoparticles was achieved using the dewetting method only [1]. The advance associated with the two-level procedure applied here is to control the arrangement of phases with respect to the facets of the particle.

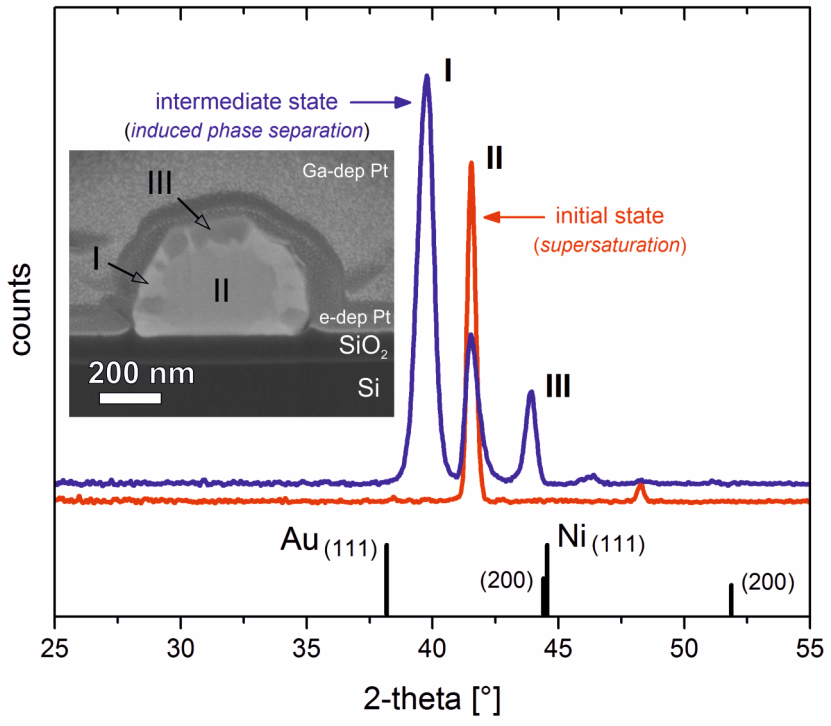


**Figure 74.** Induced phase separation which is characterized by an intermediate state. XRD pattern of the 2-theta region of interest shows the evolution of peaks upon annealing (6 min at 650 °C). Au and Ni peak positions as well as relative intensities are indicated using dedicated PDFs. From SEM image contrast, respective phases can be assigned to regions in the Au-Ni particles. Au-rich (**I**) and Ni-rich (**III**) phases initially form on the faceted surface whereas the particle interior remains supersaturated (**II**). Please note that SEM image is only meant to represent the situation of an individual particle according to a much bigger area on the sample exposed to the X-ray beam during XRD.

A cross-sectional view of an equilibrated particle formed after accumulated annealing for 16 min at 650 °C is shown in Figure 75. This equilibrated state was reached by annealing particles of the intermediate state another 10 min at 650 °C. The Ni-rich {100} side facets of the particle can clearly be seen from image contrast. Even Ni accumulation in the interior of the particle is observed, whereas the lower part to the interface is fixed by Au/$SiO_2$. Moreover, no difference in height along the facets of the particle is found, indicating that Ni-rich phases are fully embedded in the host particle. *Amram and Rabkin* deduce that the location of a precipitate depends on its size–the preferred position of a smaller one is inside the particle whereas greater precipitates tend to migrate to the side surface of the particle once reaching a critical size [51]. This tendency can also be seen from Figure 75c, resulting in *sandwich-like* structured Au-Ni particles.

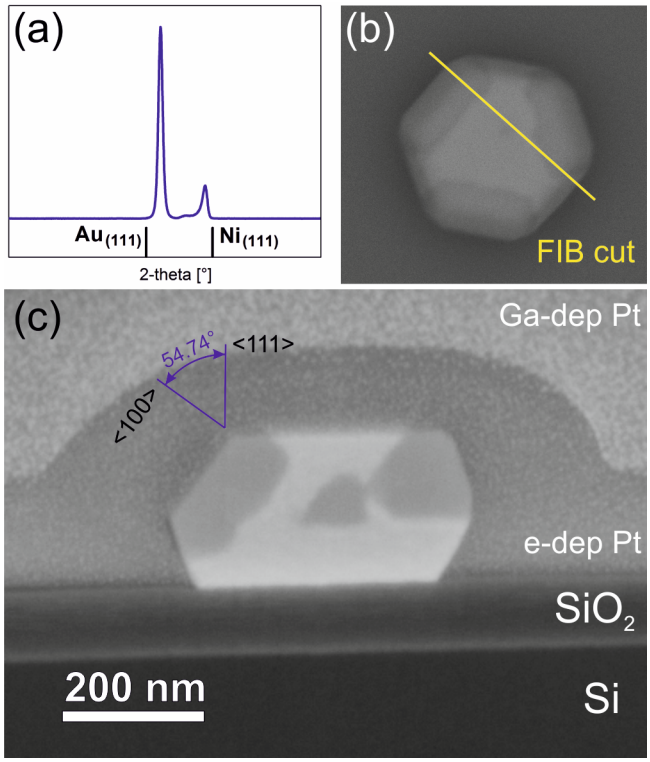


**Figure 75.** A detailed representation of an equilibrated Au-Ni particle after accumulated annealing for 16 min at 650 °C. (a) XRD pattern, (b) particle top view indicating the position of the FIB cut perpendicular to a side facet, (c) SEM cross-sectional view: The $SiO_2$/Si substrate as well as the Pt layers deposited via electron (e-dep) and Ga (Ga-dep) beam prior to FIB processing are labeled. It is evident that {100} side facets of the particle contain the Ni-rich phase (dark gray in Z-contrast). Additionally, some Ni amount is found to precipitate in the interior of the particle.

### 6.3.2 *Elastic response of two-phase faceted particles*

The Ni-rich phase situated on {100} side facets has a considerable width reaching several nanometers. Segregation effects are therefore unlikely to explain why {100} side facets contain this phase and not the Au-rich one. Both phases are instead expected to be elastically strained during their formation on the respective facets. Energetics of both phases is then related to single crystalline bulk anisotropic elastic properties that are conveniently characterized by an area modulus of elasticity (for details see Refs. [89, 90]).

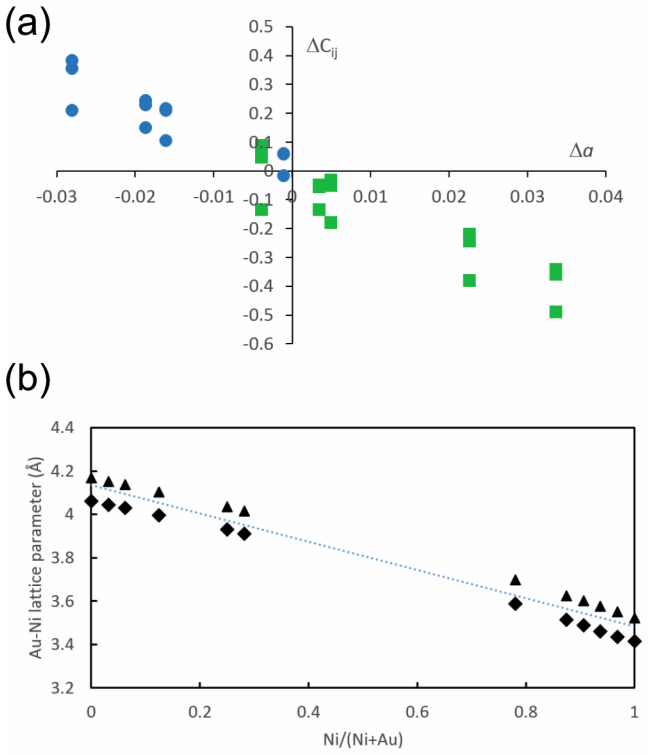


**Figure 76.** Computational procedure. (a) Relative deviations of computed elastic constants $\Delta C_{ij} = (C^{th}_{ij} - C^{exp}_{ij})/C^{exp}_{ij}$ (values for $C_{11}$, $C_{12}$, and $C_{44}$ included) as a function of relative deviations of the calculated equilibrium lattice parameter $\Delta a = (a^{th} - a^{exp})/a^{exp}$ obtained for both pure Ni (●) and Au (■) using different GGA and LDA approximations to the exchange-correlation functional in the quantum-mechanical calculations. (b) Computed compositional trends in lattice parameters of Au-Ni solid solutions using the local density approximation (LDA,▲) or generalized gradient approximation (GGA,♦) to the exchange-correlation functional.

The area modulus of elasticity is a two-dimensional counterpart of the Young's modulus: Similarly, as the single crystalline Young's modulus $Y(\boldsymbol{r})$ connects uniaxial stresses along a vector $\boldsymbol{r}$ with strains along this direction, the area modulus $A(\boldsymbol{r})$ connects equibiaxial planar stresses within a plane having a plane normal vector $\boldsymbol{r}$ with the relative area change of this plane. For cubic systems, the single crystal anisotropic area modulus $A(\boldsymbol{r})$ is expressed as

$$A(\boldsymbol{r})^{-1} = Y(\boldsymbol{r})^{-1} + (3B)^{-1}, \quad (19)$$

where $B$ is the bulk modulus (see, *e.g.*, Refs. [91, 92]). The area modulus of elasticity is derived from single crystalline elastic constants. These are challenging to measure for the Au-rich and Ni-rich phases as both exist only in the form of nanometer thick phases at the facets and their compositions are off their room temperature equilibrium. Therefore, theoretical tools, *i.e.*, quantum-mechanical calculations as implemented in the VASP software package are used [93-95]. Testing elemental Au and Ni, it is found that commonly used approximations to the exchange-correlation (xc) functional perform well, however, either for Au or Ni but not for both of them at the same time (such as in any Au-Ni alloy). Fortunately, it has been found that relative deviations of computed elastic constants $C^{th}_{ij}$ and the lattice parameter $a^{th}$ from experimental data ($C^{exp}_{ij}$ and $a^{exp}$ [96, 97]),

$$\Delta C_{ij} = (C^{th}_{ij} - C^{exp}_{ij})/C^{exp}_{ij} \quad (20)$$

and

$$\Delta a = (a^{th} - a^{exp})/a^{exp}, \quad (21)$$

are anti-correlated $\Delta C_{ij} \approx -12.5\ \Delta a$. This anti-correlation trend is composition-independent as it includes results obtained for both elemental Ni and Au using different parametrizations of generalized gradient approximation (GGA, [98-102]) and local density approximation (LDA, [103]) to the xc-functional. A linear fit through the data points goes very close to zero of both types of deviations (see Figure 76a). It means that from the computed $a^{th}$ and the corresponding $C^{th}_{ij}$ (that are supposed to be off the correct experimental values) it is possible to estimate values of experimental elastic constants $C^{exp}_{ij}$ if the experimental $a^{exp}$ is known. Importantly, this approach can be used also in case of other (*3d-5d*) binary systems when neither GGA nor LDA approximations to the xc-functional describe reasonably well both constituents.

XRD pattern (see Figure 75a) was used to determine the experimental lattice parameters $a^{exp}$ (0.3923 nm and 0.3569 nm). Assuming a linear compositional trend for the lattice parameter (see quantum-mechanically computed lattice parameters in Figure 76b), chemical compositions of both phases were obtained (91.88 at.% Ni and 27.98 at.% Ni). The Ni-rich and Au-rich phases were modeled by 32-atom supercells with stoichiometry $Au_3Ni_{29}$ (90.625 at.% Ni) and $Au_{23}Ni_9$ (28.125 at.% Ni) and a special quasi-random distribution of atoms inside [104, 105]. Well-converged computational parameters were used to compute $C^{th}_{ij}$ employing a stress-strain approach [106, 107]. The symmetry of cubic systems is such that three single crystal elastic constants fully describe elastic properties. The symmetry of cubic crystals leads to

identities such as $C_{11} = C_{22} = C_{33}$, $C_{12} = C_{13} = C_{23}$, or $C_{44} = C_{55} = C_{66}$. The expected low-temperature experimental values of elastic constants $C_{11}$, $C_{12}$, and $C_{44}$ (in GPa) of both the Au-rich (239.3, 186.6, 59.1) and Ni-rich (264.1, 167.0, 106.7) phases were determined and directional dependences of the area moduli of elasticity based on them are visualized in Figure 77. Alternatively, single crystal elastic constants ($C_{11}$, $C_{12}$, $C_{44}$) can also be obtained by a linear interpolation of room temperature experimental values detected for Au-24.2at.% Ni, Au-42.42at.% Ni, and elemental Ni [96, 108, 109].

It appears that the planar stresses (and consequently associated elastic energies) will be lowest in case of biaxial straining either Ni-rich or Au-rich phases within their {100} planes. As the Ni-rich phase exhibits generally higher values of the area modulus of elasticity than the Au-rich one, it is the former that forms on the {100} faces in order to minimize epitaxial elastic strains. Complementarily, the Au-rich phase then forms on the remaining type of facets, the {111} ones.

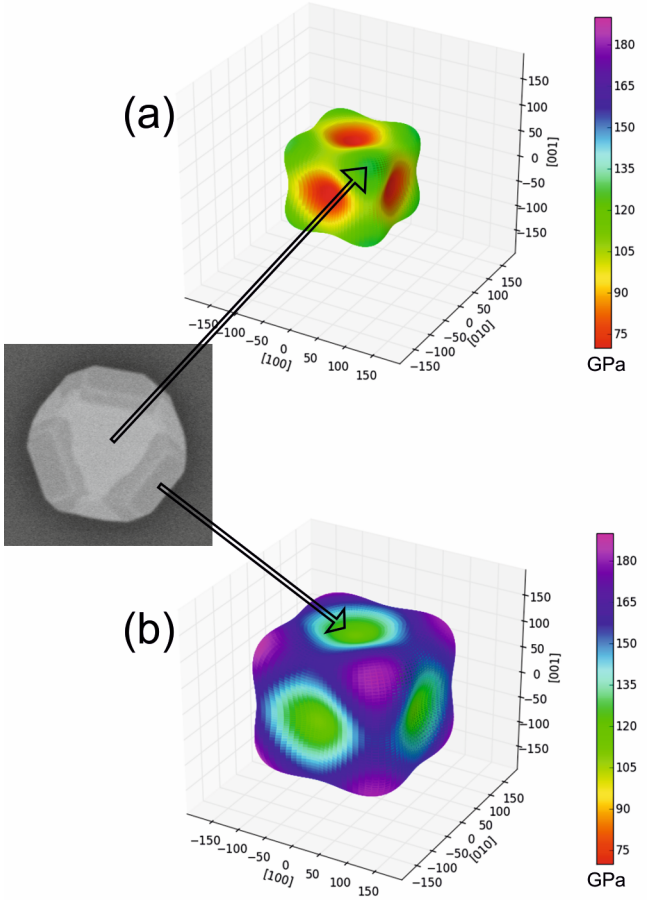


**Figure 77.** Directional dependences of the area modulus of elasticity calculated for (a) Au-rich and (b) Ni-rich phases. Arrows indicate values corresponding to the location of both phases in the faceted nanoparticles. Results are visualized by the SC-EMA package [110, 111]. In addition to dimensional scaling, area moduli are color-encoded in order to guide the eye.

The area modulus of elasticity $A(\mathbf{r})$ in both phases at low temperature ($T = 0$ K for quantum-mechanical calculations) ranges from 67.4 GPa for the {100} planes in the Au-rich phase to 177.3 GPa for the {111} planes in the Ni-rich one. Seeing this rather wide range of values, it is interesting that the value of $A(\mathbf{r})$ in the Au-rich phase for the {111} planes, 134.0 GPa, is quite close to 110.0 GPa predicted for the Ni-rich phase in case of the {100} planes (see the green color code values in Figure 77). Had the decomposition further continued to elemental Ni and Au, these two values of $A(\mathbf{r})$ computed from experimental elastic constants [96, 97] would have been even closer (116 GPa for the {111} planes in pure Au and 119 GPa for the {100} planes in Ni). The whole faceted surface of the equilibrated Au-Ni particle then possesses nearly uniform area modulus of elasticity $A(\mathbf{r})$. In other words, the difference in area modulus of the two phases would be maximum, were the order of phase arrangement reversed (an arrangement minimizing the surface energies). In that case, *a priori*, the particle would not be able to stabilize its ECS anymore. As the studied particles are too big to be solely governed by surface energies, a complex interplay between equilibrium strain-free thermodynamics and strain energy contributions can result in the formation of rather unprecedented phases decorating different types of facets. It is left for future studies, if this similarity of the area moduli of elasticity appears also in other submicron particle systems and if it can be used as a new designing principle.

## At a glance.

III. Employing bi-layer thin dewetting to define Au-Ni micro- and nanoparticles

• An experimental roadmap for Au-Ni nanoparticles is established which includes main findings depicted in Figure 78:

- Tailored Au-Ni alloy nanoparticles are fabricated via supersaturation
- Phase formation in such particles is explained by an area modulus of elasticity
- Further influencing parameters such as oxidation are intended to be studied

• Solid-state dewetting (as a simple and cost-effective method) is shown to be promising for micro- and nanoparticle research and development

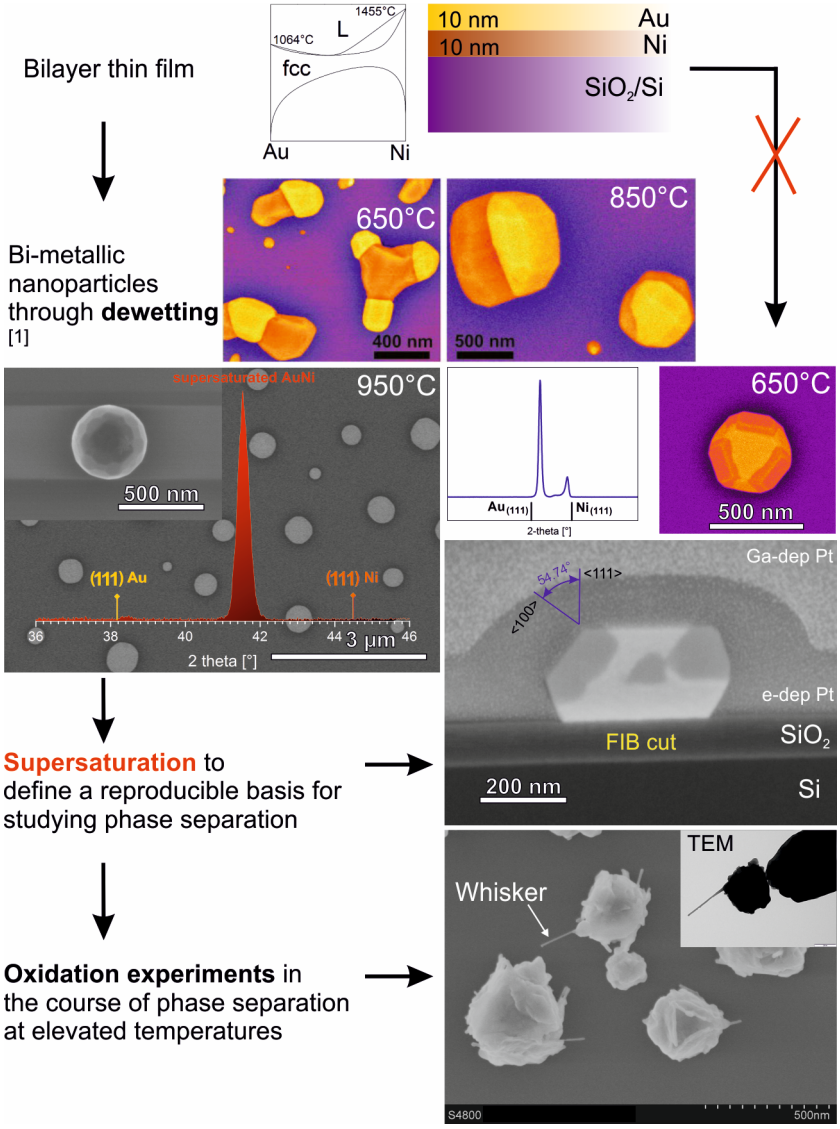


**Figure 78.** Summary of findings and observations for the fabrication of Au-Ni submicron particles. Facet-controlled arrangement of respective phases can only be achieved via the supersaturated state, and not just by dewetting (see the red cross above). Au-NiO particles having whisker ("satellites") attached to their surface are also shown. So far, these experiments have not completed yet.

# 7 Summary

## 7.1 Morphology evolution of Au and W single- and bi-layer thin films

The role of Au film thickness with respect to the formation of Au nanoparticles (NPs) and their plasmonic nature was revisited: The transformation of high-aspect ratio Au nano-islands into nanospheres upon dewetting on $SiO_2$ is accompanied by a clear blue-shift of the localized surface plasmon resonance (LSPR) peak for temperatures above 320 °C. This *shape effect* becomes more evident at increasing initial film thickness well below 10 nm. W ultrathin films were found to evolve into needle-like $WO_3$ nanorods (NRs) due to an anisotropic 1D oxide crystal growth which is *not* a dewetting mode in its usual manner. Adsorption of oxygen on the pure W surface is seen to play a major role for the self-assembly of W films. The aspect-ratio of oxide NRs can be easily tuned by the annealing temperature.

For bi-layer thin films, both W and Au were revealed to evolve independently due to their immiscibility in solid state. It was pointed out that, at medium temperature, an additional thin W layer changes the dewetting nature of $Au/SiO_2$: W being the ground layer delays the dewetting of Au, acting as a non-wetting substrate. Oxidation of the pure W surface may also influence the dewetting nature of Au. W being the top layer even passivates the Au film and no dewetting occurs. The influence of stacking sequence was found to be substantial while individual Au layer thickness affects the degree of coverage in the as-deposited state. However, combination of Au thin film dewetting and oxide NR formation eventually results in the self-assembly of *ordered arrays* of Au-$WO_3$ NPs, potentially being used as a simple and cost-effective way to fabricate tailored Au-$WO_3$ nanostructures for photocatalytic applications.

## 7.2 Solid-state dewetting of Au-Ni bi-layer thin films

This part of the present thesis points out that solid-state dewetting of metallic bi-layer thin films discloses even new characteristics due to alloying. The solid-state dewetting of Au/Ni bi-layer thin films at elevated temperature showed that individual layer thickness and stacking sequence are crucial parameters for the formation of crystal voids in the thin film having a total thickness of 20 nm. Further void evolution was investigated for a fixed bi-layer film arrangement (10 nm Au on 10 nm Ni) and, therefore, for a *fixed* composition of the overall alloy. In order to connect the dewetting with the mixing of Au and Ni, annealing temperature was increased from 500 up to 900 °C passing the miscibility gap of the Au-Ni binary alloy. A

rapid thermal annealing technique turned out to be suitable for this purpose. The combination of XRD and electron microscopy was applied to specify morphology and microstructure upon Au-Ni bi-layer thin film dewetting.

A complex interplay between void evolution and mixing of Au and Ni in the thin films is highlighted. At 650 °C, film rupturing predominantly occurred at the phase boundaries and voids were found to evolve via the Ni-rich phase in the phase separated Au-Ni thin film. Owing to the GIBBS-THOMSON effect, solubility enhancement could be observed at increased temperatures resulting in three or even four phase equilibria. Due to this, void growth at 650 °C was found to be different from that at 700 °C and a remarkable thermal stability against film rupturing was observed even at that higher temperature. Beyond the miscibility gap, the dewetted state could be reached upon annealing for 1 min at 900 °C: Elongated and flat agglomerates are formed characterized by supersaturated, well-oriented Au-Ni solid solutions exhibiting similar composition like the initial state.

## 7.3 Preparation of tailored Au-Ni micro- and nanoparticles via dewetting

Supersaturated, well-oriented Au-Ni submicron particles were successfully prepared via dewetting of a thin Au/Ni bi-layer thin film for 1 min at 950 °C. Their composition and, consequently, magnetic properties is determined by the initial thickness ratio of individual Au and Ni layers (10 nm Au on 10 nm Ni in the present case). Precise arrangements of such particles could be realized through *templated dewetting* of corresponding bi-layer films on a pre-patterned $SiO_2$/Si (inverted pyramidal pits) substrate. Effects of the pre-defined surface topography of the substrate on supersaturated Au-Ni nanoparticles were also disclosed: Quite a few *twin* particles were observed which form a new horizontal surface negative curvature (concave at the joint). As a consequence, some Au-rich material was found to be located on the mesa region through surface curvature induced surface diffusion.

In a next step, a two-level procedure employing bi-layer thin film dewetting and metallurgy at reduced scale (which clearly differs from conventional chemical ways) was used in this work to produce *facet-controlled* Au-Ni alloy particles. The supersaturated state showed nano-faces on the surface of respective spherical particles. Upon annealing at 650 °C, phase separation could be studied with respect to particle shape equilibration. Here, similar crystal lattices of the constituents and thus similar equilibrium crystal shapes (ECS) are pointed out to be a limiting factor for the arrangement of phases in such particles. It was found that {100} facets of

equilibrated Au-Ni particles are enriched with Ni, {111} faces with Au. In order to explain these observations, both Au- and Ni-rich phases were studied by quantum-mechanical calculations in combination with an error-reduction scheme that was developed to compensate for a missing exchange-correlation potential reliably describing both Au and Ni. The Ni-rich phase is stabilized by minimizing its elastic strain energy on the respective facet conveniently expressed by the anisotropic *area modulus of elasticity*. The whole faceted surface is predicted to possess nearly *uniform elastic response* to epitaxial strains and stresses. Recent findings provide an insight into features of the metallurgy at reduced scale and may contribute to designing novel tailored alloy particles.

## 7.4 Perspectives

Based on results and findings of the present work, future studies on solid-state dewetting of multicomponent thin films may include thin multilayers which could reveal new effects on void formation and their evolution at early stages of the dewetting and, consequently, on the overall thin film stability.

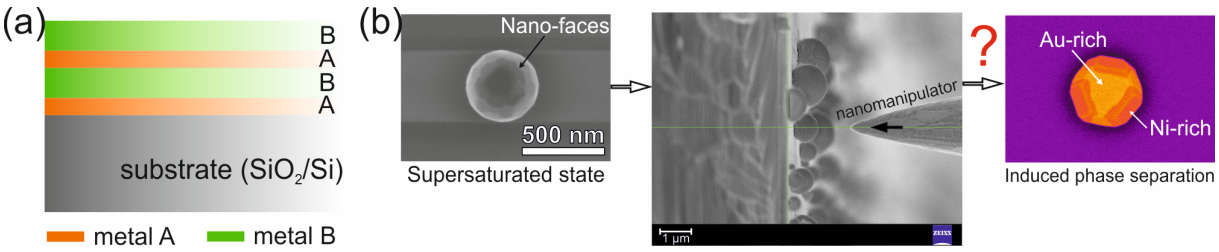


**Figure 79.** Future prospects. (a) Metallic multilayer thin films (consisting of two components) are expected to be another interesting starting point for the investigation of the dewetting of multicomponent thin films. (b) Understanding parameters that define alloy particles at the mesoscale: Introducing defects in supersaturated Au-Ni particles via FIB Nanomanipulation, for example, is supposed to critically affect the arrangement of respective phases upon post-thermal treatment.

As shown in the current thesis, stacking sequence as well as individual layer thickness are crucial for voids to form in bi-layer thin films. Thin multilayer films consisting of two components such as Au and Ni provide an increased number of possible layer arrangements (see Figure 79a). Variations in individual layer thickness additionally affects dewetting behavior. Moreover, other Au-based binary alloys or even ternary alloys could be subject to future studies on solid-state dewetting. Concerning the dewetting route, simplicity and cost efficiency of this preparation method is beyond discussion. In recent years, the dewetting method as well as solution-processed, chemical ways have been established as complementary backbones in the field of nanoparticle research and development. Even more research work

should be spent on the issue *how* phases will arrange in submicron- and nanoparticles (see Figure 79b). A comprehensive understanding of parameters that define alloy particles is needed to exploit their great potential. Also probing functionalities is intended to be another main objective in order to check for possible applications.

# List of references


[1] Wang D, Schaaf P. Ni–Au bi-metallic nanoparticles formed via dewetting. Materials Letters 2012;70:30.

[2] Destouesse E, Chambon S, Courtel S, Hirsch L, Wantz G. Solution-Processed Small-Molecule Bulk Heterojunctions: Leakage Currents and the Dewetting Issue for Inverted Solar Cells. ACS Applied Materials & Interfaces 2015;7:24663.

[3] Geiger C, Carvalho-Knighton K. *Environmental Applications of Nanoscale and Microscale Reactive Metal Particles* (Oxford University Press, New York, 2010).

[4] Lee K, Kim M, Kim H. Catalytic nanoparticles being facet-controlled. Journal of Materials Chemistry 2010;20:3791.

[5] Chang T-C, Jian F-Y, Chen S-C, Tsai Y-T. Developments in nanocrystal memory. Materials Today 2011;14:608.

[6] Sun H, Yu M, Wang G, Sun X, Lian J. Temperature-Dependent Morphology Evolution and Surface Plasmon Absorption of Ultrathin Gold Island Films. The Journal of Physical Chemistry C 2012;116:9000.

[7] Wu Y, Li G, Cherqui C, Bigelow NW, Thakkar N, Masiello DJ, Camden JP, Rack PD. Electron Energy Loss Spectroscopy Study of the Full Plasmonic Spectrum of Self-Assembled Au–Ag Alloy Nanoparticles: Unraveling Size, Composition, and Substrate Effects. ACS Photonics 2016;3:130.

[8] Danielson DT, Sparacin DK, Michel J, Kimerling LC. Surface-energy-driven dewetting theory of silicon-on-insulator agglomeration. Journal of Applied Physics 2006;100:083507.

[9] Michalak WD, Miller JB, Yolcu C, Gellman AJ. Fabrication of metallic nanoparticles by spinodal dewetting of thin films: A high-throughput approach. Thin Solid Films 2012;522:473.

[10] Müller CM, Mornaghini FCF, Spolenak R. Ordered arrays of faceted gold nanoparticles obtained by dewetting and nanosphere lithography. Nanotechnology 2008;19:485306.

[11] Ye J. Investigation of the mechanism of solid-state dewetting of silver thin films using spatial correlation analysis of hole patterns. Applied Physics Express 2014;7:085601.

[12] Shaffir E, Riess I, Kaplan WD. The mechanism of initial de-wetting and detachment of thin Au films on YSZ. Acta Materialia 2009;57:248.

[13] Kaplan W, Chatain D, Wynblatt P, Carter WC. A review of wetting versus adsorption, complexions, and related phenomena: the rosetta stone of wetting. Journal of Materials Science 2013;48:5681.

[14] Mullins WW. Theory of Thermal Grooving. Journal of Applied Physics 1957;28:333.

[15] Müller CM, Spolenak R. Dewetting of Au and AuPt alloy films: A dewetting zone model. Journal of Applied Physics 2013;113:094301.

[16] Wong H, Voorhees PW, Miksis MJ, Davis SH. Periodic mass shedding of a retracting solid film step. Acta Materialia 2000;48:1719.

[17] Kondic L, Diez JA, Rack PD, Guan Y, Fowlkes JD. Nanoparticle assembly via the dewetting of patterned thin metal lines: Understanding the instability mechanisms. Physical Review E 2009;79:026302.

[18] Fowlkes JD, Kondic L, Diez J, Wu Y, Rack PD. Self-Assembly versus Directed Assembly of Nanoparticles via Pulsed Laser Induced Dewetting of Patterned Metal Films. Nano Letters 2011;11:2478.

[19] Karim S, Toimil-Molares ME, Ensinger W, Balogh AG, Cornelius TW, Khan EU, Neumann R. Influence of crystallinity on the Rayleigh instability of gold nanowires. Journal of Physics D: Applied Physics 2007;40:3767.

[20] Ye J, Thompson CV. Mechanisms of complex morphological evolution during solid-state dewetting of single-crystal nickel thin films. Applied Physics Letters 2010;97:071904.

[21] Ye J, Thompson CV. Anisotropic edge retraction and hole growth during solid-state dewetting of single crystal nickel thin films. Acta Materialia 2011;59:582.

[22] Kirchheim R. Grain coarsening inhibited by solute segregation. Acta Materialia 2002;50:413.

[23] Haasen P. *Physikalische Metallkunde*, 3rd ed. (Springer, Berlin Heidelberg New York, 1994), pp. 76–99.

[24] Müller CM, Spolenak R. Microstructure evolution during dewetting in thin Au films. Acta Materialia 2010;58:6035.

[25] Atiya G, Chatain D, Mikhelashvili V, Eisenstein G, Kaplan WD. The role of abnormal grain growth on solid-state dewetting kinetics. Acta Materialia 2014;81:304.

[26] Kim HC, Theodore ND, Alford TL. Comparison of texture evolution in Ag and Ag(Al) alloy thin films on amorphous $SiO_2$. Journal of Applied Physics 2004;95:5180.

[27] Niekiel F, Kraschewski SM, Schweizer P, Butz B, Spiecker E. Texture evolution and microstructural changes during solid-state dewetting: A correlative study by complementary in situ TEM techniques. Acta Materialia 2016;115:230.

[28] Kovalenko O, Greer JR, Rabkin E. Solid-state dewetting of thin iron films on sapphire substrates controlled by grain boundary diffusion. Acta Materialia 2013;61:3148.

[29] Amram D, Klinger L, Gazit N, Gluska H, Rabkin E. Grain boundary grooving in thin films revisited: The role of interface diffusion. Acta Materialia 2014;69:386.

[30] Kosinova A, Kovalenko O, Klinger L, Rabkin E. Mechanisms of solid-state dewetting of thin Au films in different annealing atmospheres. Acta Materialia 2015;83:91.

[31] Malyi O, Klinger L, Srolovitz DJ, Rabkin E. Size and shape evolution of faceted bicrystal nanoparticles of gold on sapphire. Acta Materialia 2011;59:2872.

[32] Kovalenko O, Rabkin E. Mechano-stimulated equilibration of gold nanoparticles on sapphire. Scripta Materialia 2015;107:149.

[33] Malyi O, Rabkin E. The effect of evaporation on size and shape evolution of faceted gold nanoparticles on sapphire. Acta Materialia 2012;60:261.

[34] Esterina R, Liu XM, Adeyeye AO, Ross CA, Choi WK. Solid-state dewetting of magnetic binary multilayer thin films. Journal of Applied Physics 2015;118:144902.

[35] Petersen J, Mayr SG. Dewetting of Ni and NiAg solid thin films and formation of nanowires on ripple patterned substrates. Journal of Applied Physics 2008;103:023520.

[36] Perzanowski M, Zabila Y, Morgiel J, Polit A, Krupinski M, Dobrowolska A, Marszałek M. AFM, XRD and HRTEM Studies of Annealed FePd Thin Films. Acta Physica Polonica A 2010;117:423.

[37] Amram D, Klinger L, Rabkin E. Anisotropic hole growth during solid-state dewetting of single-crystal Au–Fe thin films. Acta Materialia 2012;60:3047.

[38] Amram D, Rabkin E. On the role of Fe in the growth of single crystalline heteroepitaxial Au thin films on sapphire. Acta Materialia 2013;61:4113.

[39] Jedele A. Die Diffusion im festen Zustand bei den Metallpaaren Gold-Nickel, Gold-Palladium und Gold-Platin. Zeitschrift Elektrochemie 1933;39:691.

[40] Clearfield R, Railsback JG, Pearce RC, Hensley DK, Fowlkes JD, Fuentes-Cabrera M, Simpson ML, Rack PD, Melechko AV. Reactive solid-state dewetting of Cu--Ni films on silicon. Applied Physics Letters 2010;97:253101.

[41] Sachan R, Yadavali S, Shirato N, Krishna H, Ramos V, Duscher G, Pennycook SJ, Gangopadhyay AK, Garcia H, Kalyanaraman R. Self-organized bimetallic Ag–Co nanoparticles with tunable localized surface plasmons showing high environmental stability and sensitivity. Nanotechnology 2012;23:275604.

[42] Li J, Yin D, Li Q, Chen C, Huang S, Wang Z. A dewetting route to grow heterostructured nanoparticles based on thin film heterojunctions. Nanoscale 2015.

[43] Seo O, Oh SA, Lee JY, Ha SS, Kim JM, Choi JW, Kim J-W, Kang HC, Noh DY. Controlling the alloy composition of PtNi nanocrystals using solid-state dewetting of bilayer films. Journal of Alloys and Compounds 2016;667:141.

[44] Wu Y, Fowlkes JD, Rack PD. The optical properties of Cu-Ni nanoparticles produced via pulsed laser dewetting of ultrathin films: The effect of nanoparticle size and composition on the plasmon response. Journal of Materials Research 2011;26:277.

[45] Okamoto H, Massalski TB. *Phase Diagrams of Binary Gold Alloys* (ASM International, Materials Park Novelty OH, 1987).

[46] Wolverton C, Zunger A. Ni-Au: A testing ground for theories of phase stability. Computational Materials Science 1997;8:107.

[47] Wang D, Schaaf P. Nanoporous gold nanoparticles. Journal of Materials Chemistry 2012;22:5344.

[48] Amram D, Klinger L, Rabkin E. Phase transformations in Au(Fe) nano- and microparticles obtained by solid state dewetting of thin Au–Fe bilayer films. Acta Materialia 2013;61:5130.

[49] Amram D, Amouyal Y, Rabkin E. Encapsulation by segregation – A multifaceted approach to gold segregation in iron particles on sapphire. Acta Materialia 2016;102:342.

[50] Amram D, Barlam D, Rabkin E, Shneck RZ. Coherency strain reduction in particles on a substrate as a driving force for solute segregation. Scripta Materialia 2016;122:89.

[51] Amram D, Rabkin E. Core(Fe)–Shell(Au) Nanoparticles Obtained from Thin Fe/Au Bilayers Employing Surface Segregation. ACS Nano 2014;8:10687.

[52] Amram D, Kovalenko O, Rabkin E. The α ↔ γ transformation in Fe and Fe–Au thin films, micro- and nanoparticles – an in situ study. Acta Materialia 2015;98:343.

[53] Wang D, Schaaf P. Thermal dewetting of thin Au films deposited onto line-patterned substrates. Journal of Materials Science 2012;47:1605.

[54] Wang D, Ji R, Schaaf P. Formation of precise 2D Au particle arrays via thermally induced dewetting on pre-patterned substrates. Beilstein Journal of Nanotechnology 2011;2:318.

[55] Giermann AL, Thompson CV. Solid-state dewetting for ordered arrays of crystallographically oriented metal particles. Applied Physics Letters 2005;86:121903.

[56] Giermann AL, Thompson CV. Requirements for graphoepitaxial alignment through solid-state dewetting of Au films. Journal of Applied Physics 2011;109:083520.

[57] Makarov SV, Milichko VA, Mukhin IS, Shishkin II, Zuev DA, Mozharov AM, Krasnok AE, Belov PA. Controllable femtosecond laser-induced dewetting for plasmonic applications. Laser & Photonics Reviews 2016;10:91.

[58] https://www.youtube.com/watch?v=dh3Kw680uXc (date of retrieving data: June 16, 2016).

[59] Oh Y-J, Ross CA, Jung YS, Wang Y, Thompson CV. Cobalt Nanoparticle Arrays made by Templated Solid-State Dewetting. Small 2009;5:860.

[60] Le Bris A, Maloum F, Teisseire J, Sorin F. Self-organized ordered silver nanoparticle arrays obtained by solid state dewetting. Applied Physics Letters 2014;105:203102.

[61] Wang D, Ji R, Albrecht A, Schaaf P. Ordered arrays of nanoporous gold nanoparticles. Beilstein Journal of Nanotechnology 2012;3:651.

[62] Oh Y-J, Kim J-H, Thompson CV, Ross CA. Templated assembly of Co-Pt nanoparticles via thermal and laser-induced dewetting of bilayer metal films. Nanoscale 2013;5:401.

[63] Henley SJ, Carey JD, Silva SRP. Pulsed-laser-induced nanoscale island formation in thin metal-on-oxide films. Physical Review B 2005;72:195408.

[64] Ye J, Thompson CV. Regular pattern formation through the retraction and pinch-off of edges during solid-state dewetting of patterned single crystal films. Physical Review B 2010;82:193408.

[65] Ye J. Fabrication of ordered arrays of micro- and nanoscale features with control over their shape and size via templated solid-state dewetting. Scientific Reports 2015;5:9823.

[66] Ruffino F, Grimaldi MG. Self-organized patterned arrays of Au and Ag nanoparticles by thickness-dependent dewetting of template-confined films. Journal of Materials Science 2014;49:5714.

[67] Wong S, Shalav A, Ruffell S, Bradby JE, Field MR, McCulloch DG, Elliman RG. Formation of ordered arrays of gold particles by nanoindentation templating. physica status solidi (RRL) – Rapid Research Letters 2014;8:48.

[68] Rinke TJ, Koch C. *Photolithography – Theory and Application of Photoresists, Etchants and Solvents* (MicroChemicals® - Basics of Microstructuring, Ulm, 2012).

[69] Kienel G. *Vakuumbeschichtung 4* (VDI-Verlag GmbH, Düsseldorf, 1993), p. 17.

[70] INSTRUCTION MANUAL FOR MODEL S-4800 FIELD EMISSION SCANNING ELECTRON MICROSCOPE (Hitachi High-Technologies Corporation, 2003).

[71] Spieß L, Teichert G, Schwarzer R, Behnken H, Genzel C. *Moderne Roentgenbeugung*, 2nd ed. (Vieweg+Teubner, Wiesbaden, 2009), p. 116.

[72] Lee S-H, Kwak E-H, Jeong G-H. Dewetting behavior of electron-beam-deposited Au thin films on various substrates: graphenes, quartz, and $SiO_2$ wafers. Applied Physics A: Materials Science & Processing 2015;118:389.

[73] Rasband WS. *ImageJ* (U. S. National Institutes of Health, Bethesda MD, 2016), at http://imagej.nih.gov/ij/.

[74] Liu Z, Lee C, Narayanan V, Pei G, Kan EC. Metal nanocrystal memories. I. Device design and fabrication. IEEE Transactions on Electron Devices 2002;49:1606.

[75] Pokhrel S, Birkenstock J, Dianat A, Zimmermann J, Schowalter M, Rosenauer A, Ciacchi LC, Madler L. In situ high temperature X-ray diffraction, transmission electron microscopy and theoretical modeling for the formation of $WO_3$ crystallites. CrystEngComm 2015;17:6985.

[76] Jehn H, Katscher H. *W Wolfram* in *Gmelin Handbook of Inorganic and Organometallic Chemistry*, 8th ed. (Springer, Berlin Heidelberg, 1978), pp. 89–172.

[77] Nsimama PD, Herz A, Wang D, Schaaf P. Influence of the substrate on the morphological evolution of gold thin films during solid-state dewetting. Applied Surface Science 2016;388, Part A:475.

[78] Li J, Yin D, Li Q, Chen C, Huang S, Wang Z. A dewetting route to grow heterostructured nanoparticles based on thin film heterojunctions. Nanoscale 2015;7:19977.

[79] Crawley AF, Fabian DJ. A Redetermination of the Lattice Spacings and Densities of Gold-Nickel Solutions. Journal of the Institute of Metals 1966;94:39.

[80] Haynes WM. *CRC Handbook of Chemistry and Physics. A ready-reference Book of Chemical and Physical Data*, 92nd ed. (CRC Press, Boca Raton FL, 2011).

[81] Landolt-Börnstein. *Group IV Physical Chemistry* (Springer-Verlag, 2007), Vol. 19B5, pp. 1–4.

[82] Kennedy MS, Moody NR, Adams DP, Clift M, Bahr DF. Environmental influence on interface interactions and adhesion of Au/$SiO_2$. Materials Science and Engineering: A 2008;493:299.

[83] Lee CH, Kim J-H, Zou C, Cho IS, Weisse JM, Nemeth W, Wang Q, van Duin ACT, Kim T-S, Zheng X. Peel-and-Stick: Mechanism Study for Efficient Fabrication of Flexible/Transparent Thin-film Electronics. Scientific Reports 2013;3.

[84] Cen X, Thron A, Zhang X, van Benthem K. Cross-sectional characterization of the dewetting of a Au/Ni Bilayer Film. Ultramicroscopy (2016), doi:10.1016/j.ultramic.2016.06.004.

[85] Vitos L, Ruban AV, Skriver HL, Kollár J. The surface energy of metals. Surface Science 1998;411:186.

[86] Cheung TD, Kouvel JS, Garland JW. Giant-moment clusters in paramagnetic and weakly ferromagnetic Pd-Ni alloys. Physical Review B 1981;23:1245.

[87] Kuentzler R, Kappler JP. Heat capacity and magnetisation of gold-nickel alloys. Journal of Physics F: Metal Physics 1979;9:195.

[88] Wang D, Schaaf P. Solid-state dewetting for fabrication of metallic nanoparticles and influences of nanostructured substrates and dealloying. physica status solidi (a) 2013;210:1544.

[89] Scott NH. An Area Modulus of Elasticity: Definition and Properties. Journal of Elasticity 2000;58:269.

[90] Norris AN. Poisson's ratio in cubic materials. Proceedings of the Royal Society A: Mathematical, Physical and Engineering Science 2006;462:3385.

[91] Zhu LF, Friák M, Dick A, Grabowski B, Hickel T, Liot F, Holec D, Schlieter A, Kühn U, Eckert J, Ebrahimi Z, Emmerich H, Neugebauer J. First-principles study of the thermodynamic and elastic properties of eutectic Fe–Ti alloys. Acta Materialia 2012;60:1594.

[92] Hemzalová P, Friák M, Šob M, Ma D, Udyansky A, Raabe D, Neugebauer J. Ab initio study of thermodynamic, electronic, magnetic, structural, and elastic properties of $Ni_4N$ allotropes. Physical Review B 2013;88:174103.

[93] Kresse G, Furthmüller J. Efficient iterative schemes for ab initio total-energy calculations using a plane-wave basis set. Physical Review B 1996;54:11169.

[94] Kresse G, Joubert D. From ultrasoft pseudopotentials to the projector augmented-wave method. Physical Review B 1999;59:1758.

[95] Blöchl PE. Projector augmented-wave method. Physical Review B 1994;50:17953.

[96] Çagin T, Pettitt BM. Elastic constants of nickel: Variations with respect to temperature and pressure. Physical Review B 1989;39:12484.

[97] Güler E, Güler M. Geometry Optimization Calculations for the Elasticity of Gold at High Pressure. Advances in Materials Science and Engineering 2013;2013:5.

[98] Perdew JP, Burke K, Ernzerhof M. Generalized Gradient Approximation Made Simple. Physical Review Letters 1996;77:3865.

[99] Perdew JP, Burke K, Ernzerhof M. Perdew, Burke, and Ernzerhof Reply. Physical Review Letters 1998;80:891.

[100] Armiento R, Mattsson AE. Functional designed to include surface effects in self-consistent density functional theory. Physical Review B 2005;72:085108.

[101] Mattsson AE, Armiento R. Implementing and testing the AM05 spin density functional. Physical Review B 2009;79:155101.

[102] Perdew JP, Ruzsinszky A, Csonka GI, Vydrov OA, Scuseria GE, Constantin LA, Zhou X, Burke K. Restoring the Density-Gradient Expansion for Exchange in Solids and Surfaces. Physical Review Letters 2008;100:136406.

[103] Perdew JP, Zunger A. Self-interaction correction to density-functional approximations for many-electron systems. Physical Review B 1981;23:5048.

[104] Wei SH, Ferreira LG, Bernard JE, Zunger A. Electronic properties of random alloys: Special quasirandom structures. Physical Review B 1990;42:9622.

[105] von Pezold J, Dick A, Friák M, Neugebauer J. Generation and performance of special quasirandom structures for studying the elastic properties of random alloys: Application to Al-Ti. Physical Review B 2010;81:094203.

[106] 32-atom supercells consisting of 2×2×2 fcc elementary cells, 400 eV cut-off energy, 7×7×7 Morkhorst-Pack k-point meshes, 0.1 eV smearing parameter.

[107] Zhou L, Holec D, Mayrhofer PH. First-principles study of elastic properties of cubic $Cr_{1-x}Al_xN$ alloys. Journal of Applied Physics 2013;113:043511.

[108] Golding B, Moss SC, Averbach BL. Composition and Pressure Dependence of the Elastic Constants of Gold-Nickel Alloys. Physical Review 1967;158:637.

[109] Golding B, Moss SC. A recalculation of the gold nickel spinodal. Acta Metallurgica 1967;15:1239.

[110] Titrian H, Aydin U, Friák M, Ma D, Raabe D, Neugebauer J. Self-Consistent Scale-Bridging Approach to Compute the Elasticity of Multi-Phase Polycrystalline Materials. Materials Research Society Symposium Proceedings 2013;1524.

[111] Friák M, Zhu LF, Lymperakis L, Titrian H, Aydin U, Janus AM, Fabritius HO, Ziegler A, Nikolov S, Hemzalová P, Raabe D, Neugebauer J. Quantum-Mechanical Study of Single-Crystalline and Polycrystalline Elastic Properties of Mg-Substituted Calcite Crystals. Key Engineering Materials 2014;592 - 593:335.

# List of figures and tables

# Wissenschaftliche Vita

2016 Fachvortrag zum *Materials Science and Engineering Kongress* an der TU **Darmstadt**

Teilnahme am *3rd International Conference & 5th International MacroNano-Colloquium on the Challenges and Perspectives of Functional Nanostructures* an der TU **Ilmenau**

Posterbeitrag zum *Thüringer Werkstofftag* an der TU **Ilmenau**

2015 Posterbeitrag zur *Werkstoffwoche* „Werkstoffe für die Zukunft“ der Deutschen Gemeinschaft für Materialkunde e.V. (DGM) in **Dresden**

2014 Posterbeitrag zum *Materials Science and Engineering Kongress* an der TU **Darmstadt**

Teilnahme am DGM/DVM-*Arbeitskreistreffen* “Mikrostrukturcharakterisierung im Rasterelektronenmikroskop” am Max-Planck-Institut für Eisenforschung (MPIE) in **Düsseldorf**

2013 Teilnahme am DGM/DVM-*Arbeitskreistreffen* “Mikrostrukturcharakterisierung im Rasterelektronenmikroskop” am Institut für Werkstoffwissenschaft der TU Bergakademie in **Freiberg**

Teilnahme am *3rd Kleindiek Nanotechnik User Meeting* in **Kusterdingen**

Posterbeitrag zum *Thüringer Werkstofftag* an der TU **Ilmenau**

Fachvortrag zur *Frühjahrstagung* der Deutschen Physikalischen Gesellschaft e.V. (DPG), Sektion kondensierte Materie (SKM) in **Regensburg**, gefördert durch das *Wilhelm und Else Heraeus*-Programm der DPG zur wissenschaftlichen Kommunikation von Nachwuchsphysikerinnen und –physikern

2012 Einwöchiger *Forschungsaufenthalt* an der Slowakisch Technischen Universität in **Bratislava**, Faculty of Electrical Engineering and Information Technology

Teilnahme am *57th Ilmenau Scientific Colloquium* an der TU **Ilmenau**

Teilnahme am DGM/DVM-*Arbeitskreistreffen* “Mikrostrukturcharakterisierung im Rasterelektronenmikroskop” am Institut für Werkstoffkunde der Leibniz Universität Hannover in **Garbsen**

2011 Wissenschaftlicher Mitarbeiter und Doktorand im Fachgebiet „Werkstoffe der Elektrotechnik“ am Institut für Werkstofftechnik und Institut für Mikro- und Nanotechnologien IMN MacroNano® der Technischen Universität Ilmenau – *Promotionsvorhaben* über „Entnetzen metallischer Dünnschichtsysteme“; wiss. Betreuer: Prof. Peter Schaaf

*Diplomarbeit* über „Korngrenzensegregation von Kohlenstoff und Bildung von nanokristallinen Eisen-Kohlenstoff-Legierungen mittels Kugelmahlen“ am Institut für Materialphysik der Universität Göttingen, Arbeitsgruppe „Defactants“; wiss. Betreuer: Prof. Reiner Kirchheim

Fachvortrag zur *Frühjahrstagung* der Deutschen Physikalischen Gesellschaft e.V. (DPG), Sektion kondensierte Materie (SKM) in **Dresden**

2005 *Studium* der Physik an der Georg-August Universität Göttingen nach Erwerb der allgemeinen Hochschulreife (*Abitur*) am Tilesius-Gymnasium in Mühlhausen/Thüringen

# Lehrtätigkeit

- Betreuung von Abschluss- und Projektarbeiten

2015 *Masterarbeit*, Theska, Felix. Solid-state dewetting of Au-Ni bi-layers - The effect of layer thickness and stacking sequence.

*Projektarbeit* (MA), Krause, Razvan & Leimbach, Martin. Entnetzen von dünnen Fe-Pt- und W-Schichten.

2014 *Projektarbeit* (MA), Stürzel, Thomas K. & Theska, Felix. In-situ mikromechanische Untersuchungen an kleinen Strukturen.

2013 *Bachelorarbeit*, Theska, Felix. Einfluss der Probenpräparation auf die EBSD-Analyse von Duplex-Stahl.

- Betreuung von Praktika

| | |
|---|---|
| Werkstoffpraktikum (5. FS): | „Topographie- und Stöchiometrieanalyse“ (*Topo/Stö*) |
| Interdisziplinäres Grundpraktikum: | „Elektrische Leitfähigkeit“ (*ElLeit*)<br>„Thermische Analyse“ (*ThermAn*) |

# Liste der wissenschaftlichen Veröffentlichungen


[1] Herz A, Wang D, Schaaf P. *Selbstorganisation—Chapeau!* forschung **2016**;41:14.

[2] Herz A, Franz A, Theska F, Hentschel M, Kups T, Wang D, Schaaf P. *Solid-state dewetting of single-and bi-layer Au-W thin films: Unraveling the role of individual layer thickness, stacking sequence and oxidation on morphology evolution*. AIP Advances **2016**;6:035109.

[3] Nsimama PD, Herz A, Wang D, Schaaf P. *Influence of the substrate on the morphological evolution of gold thin films during solid-state dewetting*. Applied Surface Science **2016**;388, Part A:475.

[4] Herz A, Friák M, Rossberg D, Hentschel M, Theska F, Wang D, Holec D, Šob M, Schneeweiss O, Schaaf P. *Facet-controlled phase separation in supersaturated Au-Ni nanoparticles upon shape equilibration*. Applied Physics Letters **2015**;107:073109.

[5] Borchers C, Garve C, Tiegel M, Deutges M, Herz A, Edalati K, Pippan R, Horita Z, Kirchheim R. *Nanocrystalline steel obtained by mechanical alloying of iron and graphite subsequently compacted by high-pressure torsion*. Acta Materialia **2015**;97:207.

[6] Herz A, Wang D, Schaaf P. *Dewetting of Au/Ni bi-layer films on prepatterned substrates and the formation of arrays of supersaturated Au-Ni nanoparticles*. Journal of Vacuum Science & Technology B **2014**;32:021802.

[7] Herz A, Wang D, Kups T, Schaaf P. *Solid-state dewetting of Au/Ni bilayers: The effect of alloying on morphology evolution*. Journal of Applied Physics **2014**;116:044307.

[8] Chen YZ, Herz A, Borchers C, Shi X, Ma X, Liu F, Kirchheim R. *Inhibition of Grain Coarsening in Nanocrystalline Fe-C Alloys by Interaction between Carbon and Grain Boundaries*. Advanced Materials Research, vol. 904: Trans Tech Publ, **2014**. p.184.

[9] Wang D, Ji R, Herz A, Ronning C, Schaaf P. *Ordered arrays of patterned nanoporous silicon*. Journal of Micromechanics and Microengineering **2013**;23:074004.

[10] Herz A, Wang D, Müller R, Schaaf P. *Formation of supersaturated Au–Ni nanoparticles via dewetting of an Au/Ni bi-layer*. Materials Letters **2013**;102:22.

[11] Chen YZ, Herz A, Li YJ, Borchers C, Choi P, Raabe D, Kirchheim R. *Nanocrystalline Fe–C alloys produced by ball milling of iron and graphite*. Acta Materialia **2013**;61:3172.

[12] Kirchheim R, Chen YZ, Herz A. *Grain Boundary Segregation of Carbon and Formation of Nanocrystalline Iron-Carbon Alloys by Ball Milling*. Minerals, Metals and Materials Society/AIME, 420 Commonwealth Dr., P. O. Box 430 Warrendale PA 15086 United States.[np]. Feb **2011**.

[13] Chen YZ, Herz A, Kirchheim R. *Grain boundary segregation of carbon and formation of nanocrystalline iron-carbon alloys by ball milling*. Materials Science Forum, vol. 667: Trans Tech Publ, **2010**. p. 265.